

May 2016

# Experimental and Numerical Characterization of Scalable Cellulose Nano-fiber Composite

Bamdad Barari Barari

*University of Wisconsin-Milwaukee*

Follow this and additional works at: <https://dc.uwm.edu/etd>



Part of the [Mechanical Engineering Commons](#)

---

## Recommended Citation

Barari, Bamdad Barari, "Experimental and Numerical Characterization of Scalable Cellulose Nano-fiber Composite" (2016). *Theses and Dissertations*. 1111.

<https://dc.uwm.edu/etd/1111>

This Dissertation is brought to you for free and open access by UWM Digital Commons. It has been accepted for inclusion in Theses and Dissertations by an authorized administrator of UWM Digital Commons. For more information, please contact [open-access@uwm.edu](mailto:open-access@uwm.edu).

**EXPERIMENTAL AND NUMERICAL CHARACTERIZATION OF  
SCALABLE CELLULOSE NANO-FIBER COMPOSITE**

by

**Bamdad Barari**

A Dissertation Submitted in

Partial Fulfillment of the

Requirements for the Degree of

Doctor of Philosophy

in Engineering

at

The University of Wisconsin-Milwaukee

May 2016

## ABSTRACT

# **NUMERICAL AND EXPERIMENTAL CHARACTERIZATION OF SCALABLE CELLULOSE NANO-FIBER COMPOSITE**

by

Bamdad Barari

The University of Wisconsin-Milwaukee, 2016  
Under the Supervision of Professor Krishna M. Pillai

Fiber-reinforced polymer composites have been used in recent years as an alternative to the conventional materials because of their low weight, high mechanical properties and low processing temperatures. Most polymer composites are traditionally made using reinforcing fibers such as carbon or glass fibers. However, there has been recent interest in making these reinforcing fibers from natural resources. The plant-derived cellulose nano-fibers (CNF) are a material with remarkable mechanical properties at the nano-scale that are much superior to the mechanical properties of the traditional natural fibers (such as jute, hemp, kenaf, etc) used in the natural-fiber based polymer composites. Because CNF is bio-based and biodegradable, it is an attractive ‘green’ alternative for use in automotive, aerospace, and other engineering applications. However, efforts to produce CNF based nano-composites, with successful scaling-up of the remarkable nanoscale properties of CNF, have not met with much success and form an active area of research.

The main goals of this research are to characterize the scalable CNF based nano composites using experimental methods and to develop effective models for flow of polymeric resin in the CNF-based porous media used during the proposed manufacture of CNF nano-composites. In the

CNF composite characterization section, scalable *isotropic* and *anisotropic* CNF composites were made from a porous CNF preforms created using a freeze drying process. Formation of the fibers during freeze-drying process can change the micro skeleton of the final preform structure as non-aligned or isotropic and aligned or anisotropic CNF. Liquid Composite Molding (LCM) processes form a set of liquid molding technologies that are used quite commonly for making the conventional polymer composites. An improvised vacuum-driven LCM process was used to make the CNF-based nanocomposites from CNF preforms using a ‘green’ epoxy resin with high bio-content. Under the topic of isotropic CNF, formation of the freeze-dried CNF preforms’ porous network strongly affects the mechanical, microstructural and tribological properties of the composite, therefore experimental testing was performed to characterize the effects of pore structure on global properties of isotropic CNF composites. Level of curing was investigated by experimental methods such as DSC in order to analyze its effects on the mechanical properties. The causes of failure in the composites were discussed by analyzing the SEM micrographs of fractured surfaces. The investigations revealed that the silane treated samples show superior mechanical behavior and higher storage modulus compared to the untreated (no silane) samples. The DMA and DSC results indicated a reduction in the glass transition temperature for the CNF composites compared to the pure resin samples. The tensile results showed higher elastic moduli in composites made from silane treated CNF preforms compared to those made from non silane-treated preforms. The tribological behavior of the silylated CNFs composites showed lower coefficient of friction and wear volumes than the neat bio-epoxy due to the formation of a transfer film on the mating surfaces, which led to a decrease in the ‘direct contact’ of the composite with the asperities of the hard metallic counterface.

Under the topic of anisotropic CNF nanocomposites, a recently-discovered new type of CNF preform with more-aligned pore structure was used in our improvised LCM process to make the CNF-based anisotropic nanocomposite. The effect of such aligned pore structure on the mechanical and microstructural properties of CNF-based nanocomposites was investigated. As before, we used the tensile test, DMA and SEM to characterize this new material. Our investigation revealed that anisotropic CNF preform improved the overall mechanical properties of CNF composites due to better interfacing between the CNF and resin inside aligned pore structure of anisotropic CNF. Also, DMA results showed an improvement in the glass transition temperature of the anisotropic samples compared to the isotropic ones.

For flow modeling in the CNF-based porous medium, the closure formulation, developed as a part of the derivation of Darcy's law developed by Whitaker [1], was used to develop novel numerical and experimental methods for estimating the permeability and absorption characteristics of a porous medium with a given pore-level microstructure. The permeability of such a porous medium was estimated numerically while the absorption characteristics were analyzed through experiments. In order to use real micrograph in permeability simulations, 2D SEM pictures of the CNF-based porous media were considered. The falling head permeameter was used for measuring the experimental permeability in order to test the accuracy of the permeability tensor obtained by the proposed numerical simulation. The permeability values were also compared with the theoretical models of Kozeny-Carman. A good agreement between the numerical, experimental and analytical methods demonstrated the accuracy of the closure formulation and the resulting simulation. These results also present the closure formulation based method as a viable method to estimate the permeability of porous media using 2D SEM micrographs; such a method harnesses the micro-macro coupling and is marked with absence of any constitutive-relation based

assumption for such upscaling. Such a method is also faster, less expensive and less problematic than the corresponding 3D micro-CT scan based method because of much smaller degrees-of-freedom, memory and storage requirements.

Under the absorption characteristics study, absorption characteristics of paper-like CNF porous medium was modeled using theoretical derivation of governing equation for single-phase flow and swelling behavior and absorption coefficient were investigated through experiments. In derivation part, unique form of mass conservation was developed using volume averaging theorem in the swelling, liquid-absorbing CNF-based preform. The case of the absorption coefficient,  $b$  being unity, which corresponds to the liquid absorption rate into fibers being equal to the fiber expansion rate, results in the classical form of the continuity equation that is originally derived for a rigid, non-deforming porous medium. The value of  $b$  was determined using a novel dipping experiment conducted with the help of a microbalance and was found to be unity for flow models in swelling porous media made of the CNF.

© Copyright by Bamdad Barari, 2016  
All Rights Reserved

To  
My Parents



# TABLE OF CONTENTS

CHAPTER 1: Study of the Isotropic Cellulose Nano-Fiber based Composite.....	1
1.1. Introduction.....	1
1.2. Manufacturing process.....	4
1.2.1. Cellulose nano-fiber preforms .....	4
1.2.2. Making cellulose nano-composites using an improvised LCM process .....	5
1.3. Microstructural characterization .....	8
1.4. Mechanical Characterization.....	9
1.5. Results and discussion .....	10
1.5.1. DMA Results .....	10
1.5.2. Tensile test results.....	12
1.5.3. Water contact angle measurements.....	14
1.5.4. DSC results .....	15
1.5.5. SEM results .....	17
1.6. Summary & Conclusions .....	19
CHAPTER 2: Study of the Anisotropic Cellulose Nano-Fiber based Composite .....	21
2.1. Introduction.....	21
2.2. Sample preparation process .....	24
2.2.1. Cellulose nano-fiber preforms .....	24
2.2.2. Making cellulose nano-composites using an improvised LCM process .....	25
2.3. Microstructural and mechanical characterization .....	27

2.4. Results and discussion .....	28
2.5. Summery and Conclusions.....	34
CHAPTER 3: 2D-Micrograph based Numerical Method of Permeability Estimation in Cellulose nano-Fiber .....	36
3.1. Introduction.....	36
3.2. Theory .....	42
3.2.1. Permeability Estimation using Closure Formulation of Volume Averaging Method.....	42
3.2.2. Experimental method for estimating permeability .....	46
3.3. Results and discussion .....	47
3.3.1 Initial validation of Closure Formulation Method .....	47
3.3.2. Permeability of porous preform made from CNF .....	48
3.3.3. Experimental CNF permeability .....	55
3.4. Discussion .....	57
3.5. Summary and Conclusions.....	58
CHAPTER 4: An Analytical Study of the Absorption Characteristics of Cellulose Nano-Fiber .....	60
4.1. Introduction.....	60
4.2. Further details on modeling LCM-type flows in swelling, liquid absorbing porous media .....	62
4.3. Theory behind experimental estimation of the absorption coefficient $b$ .....	66
4.4. Experimental procedure and data analysis.....	69
4.5. Summery and conclusion .....	73
4.6. Appendix.....	74

CHAPTER 5: Mechanical, Physical and Tribological Characterization of Nano-Cellulose Fibers Composites.....	78
5.1. Introduction.....	78
5.2. Manufacturing process.....	81
5.2.1. Cellulose nano-fiber (CNF) aerogels .....	81
5.2.2. Manufacturing of CNF composites using an improvised Liquid Composite Molding (LCM) process.....	82
5.3. Characterization and testing.....	83
5.3.1. Differential scanning calorimetry tests .....	83
5.3.2. Mechanical characterization.....	84
5.3.3. Tribological characterization .....	85
5.4. Results and discussion .....	86
5.4.1. DSC characterization .....	86
5.4.2. Mechanical properties .....	89
5.4.3. Tribological Properties.....	91
5.5. Summery and Conclusions.....	105
Reference .....	107
Curriculum Vitae .....	124

## LIST OF FIGURES

Figure 1. CNF preforms used in the present study. ....	5
Figure 2. Processing of CNF Composite using the improvised LCM setup .....	6
Figure 3. A schematic of the tensile-test specimen.....	7
Figure 4. The CNF and pure resin specimens created for the tensile test. ....	8
Figure 5. DMA storage modulus plots for pure epoxy and CNF/epoxy specimens .....	11
Figure 6. DMA loss modulus plots for pure epoxy and CNF/epoxy specimens.....	12
Figure 7. DMA tan delta plots for pure epoxy and CNF/epoxy specimens.....	12
Figure 8. The experimentally measured stress-strain curves for the CNF reinforced and pure epoxy samples .....	13
Figure 9. Water contact angle (WCA) measurements for silylated CNF at 0, 5, 10, and 15 seconds after the droplet is placed on the sample. ....	14
Figure 10. First heating DSC profile.....	16
Figure 11. Second heating DSC profile .....	16
Figure 12. SEM figures of pure resin.....	18
Figure 13. SEM figures of silylated Sample .....	19
Figure 14. SEM figures of non-silylated Sample.....	19
Figure 15. The improvised vacuum-driven LCM setup and removable two-piece spacer-plate insert .....	26
Figure 16. DMA storage modulus plots for anisotropic CNF composite and pure epoxy samples .....	29
Figure 17. DMA loss modulus plots for anisotropic CNF composite and pure epoxy samples .....	29
Figure 18. DMA tan delta plots for anisotropic CNF composite and pure epoxy samples.....	30
Figure 19. The stress-strain diagrams for the anisotropic and isotropic CNF reinforced composite samples and pure epoxy samples. ....	31

Figure 20. SEM images of fractured surfaces of samples with different CNF volume fractions and different magnifications: a) Pure epoxy 100x, b) Pure epoxy 1000x, c) 1% CNF 100x, d) 1% CNF 1000x, e) 1.3% CNF 100x, f) 1.3% CNF 1000x .....	34
Figure 21. A Schematic of Falling-Head Permeameter .....	47
Figure 22. SEM micrograph of a representative sectioned plane from the CNF sample .....	50
Figure 23. The solid (white) and pore (black) regions of a reconstructed 2-D ‘binary’ region extracted from the SEM micrograph Figure 22 for various porosities: a) threshold 1 with $\epsilon=0.53$ , b) threshold 2 with $\epsilon=0.7$ and c) threshold 3 with $\epsilon=0.84$ .....	51
Figure 24. Distribution of triangular elements in a) normal, b) fine and c) extra-fine meshes used in the 2D pore space obtained with threshold 3 .....	54
Figure 25. The nine different $K_{11}$ values resulting from the mesh independence study involving the CNF permeability tensor (Eqn. (3.22)). The values correspond to three different meshes and three different pore-space geometries resulting from the application of the three different thresholds .....	54
Figure 26. Relationship between the ratio of CNF liquid-column heights and time for (a) Decane (b) Hexane. ....	56
Figure 27. Effect of changing the value of the absorption coefficient, $b$ , from 0 to 1 on the predicted length of the liquid front, $L_{lf}$ [110] as a function of time .....	64
Figure 28. Comparison of the evolution of the flow-front location during a 1D flow experiment involving the flow of a swelling-inducing liquid through a bed of natural fibers for the constant inlet pressure of 12 kPa [107] .....	65
Figure 29. Comparison of the evolution of the inlet pressure during a 1-D flow experiment involving the flow of a swelling-inducing liquid through a bed of natural fibers for the constant flow-rate of 3 ml/s [107]. ....	66
Figure 30. a) Microbalance of DCA tensiometer used for measuring the absorption coefficient, b) Schematic of the setup showing the details .....	67

Figure 31. The plot of $b'$ against $V(t) - V_0$ .....	71
Figure 32. A scatter in the value of the experimentally measured absorption coefficient, $b$ , estimated for CNF.....	72
Figure 33. a) Variation of heat flow with time for the silylated “S” and non-silylated “NS” CNF samples at 80, 100 and 130 °C and b) Normalized Heat flow with time diagram for silylated and non-silylated CNF samples at 80, 100 and 130 °C.....	89
Figure 34. Experimentally measured stress-strain curves for the CNF/bio-epoxy composites .....	90
Figure 35. SEM micrographs of: (a) non-silylated CNF composite, (b) silylated CNF composite. ....	91
Figure 36. Effect of nano-cellulose content in bio-epoxy on coefficient of friction at different normal loads for a) 0.15 m/s, b) 0.25 m/s, and c) 0.35 m/s sliding speeds and effect of nano-cellulose in bio-epoxy on wear volume at different normal loads for d) 0.15 m/s, e) 0.25 m/s, and f) 0.35 m/s sliding speeds. ....	94
Figure 37. Schematic illustration of the failure mechanism for the sliding wear of CNFs/bio-epoxy nanocomposites.....	97
Figure 38. 3D surface topography of a) neat epoxy, b) bio-epoxy reinforced by 0.9 vol.% nano-cellulose, and c) bio-epoxy reinforced by 1.4 vol.% nano-cellulose at 7N normal load and 0.15 m/s .....	100
Figure 39. Effect of normal load on COF of a) neat bio-epoxy, b) 0.9 vol.% nano-cellulose/bio-epoxy, and c) 1.4 vol.% nano-cellulose/bio-epoxy at different sliding speeds and effect of normal load on wear volume of d) neat bio-epoxy, e) 0.9 vol.% nano-cellulose/bio-epoxy, and f) 1.4 vol.% nano-cellulose/bio-epoxy at different sliding speeds .....	102
Figure 40. Worn surface of bio-epoxy nanocomposites reinforced by 1.4 vol.% nano-cellulose at a) 4N and b) 10N applied load at 0.15 m/s and worn surface of bio-epoxy nanocomposites reinforced by 1.4 vol.% nano-cellulose at 10N applied load and 0.15 m/s sliding speed at (c) 500X and (d) 1800X magnifications. ....	103
Figure 41. Effect of sliding speed on COF of nano-cellulose/ bio-epoxy nanocomposites for a) neat bio-epoxy, b) 0.9 vol.% nano-cellulose/bio-epoxy, and c) 1.4 vol.% nano-cellulose/bio-epoxy at different	

normal loads effect of sliding speed on wear volume of nano-cellulose/ bio-epoxy nanocomposites for d) neat bio-epoxy, e) 0.9 vol.% nano-cellulose/bio-epoxy, and f) 1.4 vol.% nano-cellulose/bio-epoxy at different normal load..... 105

## LIST OF TABLES

Table 1. $T_g$ of each sample during first heating and second heating.....	16
Table 2. A comparison of the mechanical properties of the anisotropic and isotropic CNF reinforced epoxy samples and the pure epoxy samples .....	33
Table 3. A comparison between the results of this study and those of Lasseux et al. in terms of dimensionless permeability $K^*$ [93].....	48
Table 4. Permeability of CNF as obtained from the closure-formulation based numerical simulations for three different thresholds. ....	52
Table 5. Physical properties of the CNF and the working fluid.....	55
Table 6. Comparison of the permeability values obtained from the closure-formulation based numerical simulation and the falling-head permeameter experiments. Units are in $m^2$ . The scatter is estimated as the 95% confidence interval obtained from three different experiments. ....	56
Table 7. Physical properties and average initial values for each CNF sample used in the dipping experiment .....	70
Table 8. Final values for the tension in the string, the weight and the absorbed liquid volume for CNF samples.....	71
Table 9. Characteristic temperatures of pure bio-epoxy and composites, obtained using the temperature ramp analysis .....	86
Table 10. Parameters of Eqn. (5.2), conversion equation as a function of time parameters. ....	88
Table 11. Summery of improvement in COF and wear rate of composites.....	96



## ACKNOWLEDGMENTS

I would like to thank my advisor, Prof. Krishna M. Pillai for guiding and supporting me over the years. You have set an example of excellence as a researcher, mentor and instructor. I would like to thank and acknowledge the efforts of Professor Lih-Sheng Turng and Mr. Thomas K. Ellingham of University of Wisconsin-Madison and Dr. Ronald C Sabo of the USDA Forest Products Laboratory at Madison for preparing CNF preforms. I would thank and acknowledge the efforts of Professor Rani El-Hajjar and his group of the Experimental Mechanics and Composites Laboratories at the University of Wisconsin-Milwaukee (UWM) for performing mechanical testing. The funding in the form of RGI grant from the graduate school of UWM and the intercampus grant from the UW System is gratefully acknowledged. I would also thank and acknowledge the efforts of Prof. Pradeep K. Rohatgi and his research group at Center for Composites for collaborating the tribological testing. Finally, I would like to thank my amazing family for the love, support, and constant encouragement I have gotten over the years. In particular, I would like to thank my parents, my lovely sister Ghazal, my brother Kian and my baby sister Nicky.

# **CHAPTER 1: Study of the Isotropic Cellulose Nano-Fiber based Composite**

## **1.1. Introduction**

Polymer matrix bio-composites are increasingly used in numerous engineering applications such as aerospace, automotive and construction. Environmental awareness on using environmentally friendly materials and a renewable resource origin of natural fibers, are the reasons which attract industrial interests in bio-composites [2]. Natural fiber polymer composites have been developed in recent years and could be used as an alternative since the 1990s [3]. Bio-composites made from hemp, flax, kenaf, etc. have become attractive in the industry, especially the auto industry, because of their low material and production costs, acceptable mechanical properties, and lower weights. The other advantages of the natural fiber composites compared to the carbon/glass polymer composites are economic viability, low cost machining, biodegradability, and enhanced energy recovery. Because of all these properties, the natural fiber composites have begun to be used in secondary structural applications in automotive industry, including those for door panels and package trays.

Responding to increasing needs for natural composites, significant research continues in the area of naturally derived composite materials. Abdul Khalil et al. [4, 5] used lignin derived from oil-palm biomass waste with epoxy matrix to improve the thermal and mechanical properties of bio-composites. Ho and Lau [6] used silk fibers to enhance the elastic modulus, impact strength and elongation of glass-fiber based composites.

Cellulose, extracted from plants, is an attractive material to make biocomposites from due to its high availability and biodegradability. However, the cellulose is a poor reinforcement due to its mechanical weakness. However, its properties at the nanoscale are completely different.

Cellulose nano-fibers (CNF) are natural fibers extracted from cellulose that have shown astonishing mechanical properties [7-10]. The first efforts in making polymer-matrix biocomposites from high volume fractions of CNF and thermoset polymer matrices resulted in brittle materials [11-13]. CNF also has been used as a reinforcement in different types of nano-composites [14, 15]. Khalid et al. [16] investigated using cellulose fillers compared to cellulose fibers with propylene matrix and reported attaining higher mechanical properties. The bonding of regenerated cellulose fibers with epoxy and polyester resins has also been investigated using a Raman spectroscopy technique [17].

CNF is now more likely than previously to be used as reinforcement because of recent improvements in the reductions of energy required for breaking down cellulose fibers into nano-fibers [18]. However, inadequate understanding on the processing of nano-fibers into reinforcements is an important limitation in making viable composite materials. Other attempts to produce bio-based composites using natural fibers and bio-based-resins have also been reported; however, these kinds of natural composite suffer from several limitations, such as low mechanical properties due to poor interface between the reinforcement and the matrix [19, 20]. For the hemp-fiber/epoxy biocomposites, the tensile strength was limited to 60 MPa at a fiber content of 40 % by weight [21], when the single-fiber strength could be as high as 900 MPa [22].

For fiber-reinforced composites, it's preferred to use epoxy as a matrix for achieving high performance properties because of the higher mechanical properties of epoxy in glassy state. Lu et al. [23] used nano-cellulose treated by silane and titanate agents to show that the storage modulus for 5 wt.% CNF increased up to 3.45 GPa. Kuo et al. [24] investigated the effects of curing of epoxy in the presence of CNF. Shibata and Nikai [25] used water-soluble components with CNF during the freeze drying process and thus created CNF preform impregnated with epoxy was cured

at increasing temperature to attain an elastic modulus around 2.6 GPa at 15 wt.% nano-cellulose loading. The corresponding tensile strength was obtained to be about 80 MPa at 10 wt.% loading.

In this chapter, silylated and non-silylated, isotropic CNF were made through a freeze-drying method and used as reinforcement with a high bio-based content epoxy. The CNF used here is called isotropic because the solid phase of the aerogel is distributed randomly with arbitrary orientation. The composite was made using an improvised, vacuum-suction driven liquid composite molding (LCM) process. Using the freeze-drying method, the suspension of CNF was converted into a form of aerogel with extremely light-weight and highly porous structure. It was presumed that CNF aerogels owing to their high porosities (above 95%) should be easily infiltrated with resin under relatively-small pressure differential ( $\sim 1$  atm) in the considered LCM process. Once the CNF aerogel's micro-scale solid skeleton is completely surrounded with epoxy, the former's high compatibility with the latter is likely to make composites with high mechanical properties. The basic idea was that cellulose nano fibers present in the CNF skeleton bond with the matrix in order to create three-dimensionally dispersed system of nanoparticles thus creating effective nanocomposites.

The mechanical behavior of the resulting CNF nanocomposite was evaluated by experimental methods. The tensile strength was estimated using the traditional quasi-static mechanical testing while the storage modulus, loss modulus and tan delta results of the samples were characterized through Dynamic Mechanical Analysis (DMA). The causes of the failures and effects of curing were investigated by the Differential Scanning Calorimetry (DSC) and Scanning Electron Microscopy (SEM) methods. The effect of silane treatment on the mechanical properties of nano composites was also studied by comparing the strength results of the treated/non-treated samples.

## 1.2. Manufacturing process

### 1.2.1. Cellulose nano-fiber preforms

TEMPO-oxidized cellulose nano-fibrils used in this chapter were prepared according to the work reported by Saito et al. [26]. Commercially-supplied bleached eucalyptus Kraft pulp (Aracruz Cellulose, Brazil) was received in dry form and used for the raw materials. The pulp was first pre-treated with an acid wash by pulping the fibers and soaking overnight at 2% solids, pH 2, and 2 wt% NaClO<sub>2</sub> (based on pulp weight). After filtering and washing the pre-treated fibers, they were then carboxylated using 2, 2, 6, 6-tetramethylpiperidine-1-oxyl (TEMPO), sodium chlorite, and sodium hypochlorite as the reactants at 60 °C for 3 days according to the procedure by Saito et al. [26]. TEMPO-oxidized pulp fibers were then washed thoroughly using reverse osmosis-purified (RO) water and homogenized in a disk refiner to break apart fibril bundles. The fiber slurry was diluted to facilitate separation of coarse and fine fractions by centrifugation, and the coarse fraction was rejected. The nano-fiber suspension was concentrated to a solid content of approximately 0.6% using ultrafiltration. A final clarification step was performed, in which the nano-fiber suspension was passed once through an M-110EH-30 Microfluidizer (Microfluidics, Newton, MA) with 200- and 87- $\mu$ m chambers in series. The carboxylate content of reacted pulp fibers was measured via titration based on TAPPI Test Method T237 cm-98 and found to be 0.65 mmol COONa per gram of pulp.

Large 18cm thick CNF preforms were then prepared by freezing the nano-fiber suspension in a tray. Smaller tensile-bar shapes were cut out of the larger CNF preforms using a Universal Laser Systems® PLS6.75 laser cutter with a 40W laser and nitrogen purge to minimize charring on the samples. For subsequent lyophilization, the laser-cut samples were placed in a glass vacuum desiccator above 1mL of trimethoxy-octadecyl silane per 5 tensile bars and kept in a vacuum oven

at 1 in of Hg and 120°C for 18 hrs. Some of the laser-cut samples were left virgin with no lyophilization to study the effect of the treatment. The resulting silylated and the non-silylated CNF preforms are shown in Figure 1.

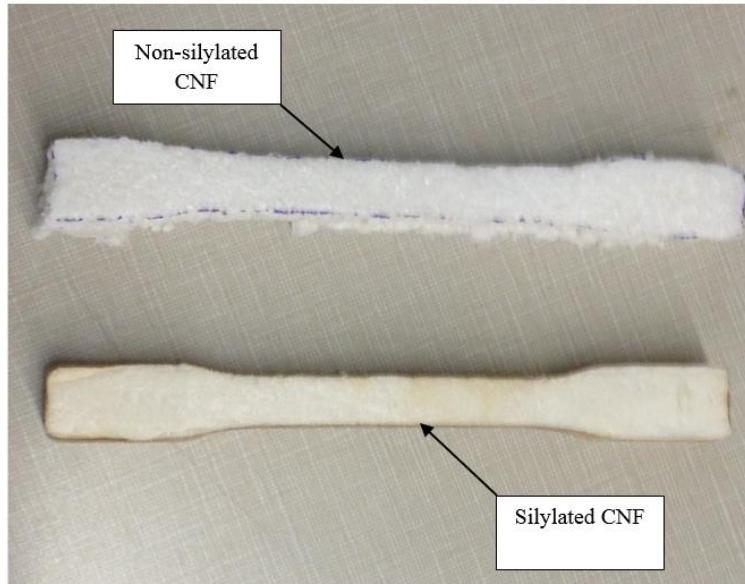


*Figure 1. CNF preforms used in the present study.*

### **1.2.2. Making cellulose nano-composites using an improvised LCM process**

The cellulose nanocomposites were made by an improvised LCM process that is a hybrid of the Resin Transfer Molding (RTM) and Vacuum-Assisted Resin Transfer Molding (VARTM) processes, and where CNF was used as the reinforcement and epoxy was infused as the matrix. In our fabrication method, instead of using a positive pressure for resin injection as used in RTM, a negative (vacuum) pressure was used, as in VARTM, to pull the resin through the CNF preform. However, the mold made from polycarbonate and aluminum was a rigid mold, as in RTM, for preventing progressive compression of the CNF preform during the resin infusion process.

Another reason we decided to use vacuum in the mold was to reduce formation of voids in the final composite part due to trapping of air as bubbles or as dry spots. As shown in Figure 2,

the entire injection setup consisted of an RTM mold, a resin trap, and a vacuum pump. The resin trap was used to prevent any resin getting sucked inside the pump. Also, a pressure gauge was installed on it to check the instant pressure during experiments. As mentioned before, the LCM mold used in experiments was made from aluminum and polycarbonate. The mold consisted of aluminum base block with a removable two-piece spacer-plate insert that creates a dog-bone shaped cavity for creating composites samples for the tensile test. The polycarbonate top-plate was used as an air seal, but it also acted as a window to detect resin movement inside the CNF preform. The mold was originally designed for resin inlet at the center of the dog-bone specimen cavity and two outlets at the specimen ends that were connected to a resin trap. In that configuration, the infusion of resin into the CNF preform was not adequate because of the race tracking phenomenon—the resin tended to pass along the edges, since the CNF skin prevented resin penetration and led to dry spots formation at the specimen center. In order to remove the dry spots, we changed the LCM mold design such that the resin was allowed in from one side, traveled horizontally along the CNF preform, and then came out from the other side. In this configuration, the resin contacted the more permeable inner core of CNF, and which increased the resin infusion into the preform.

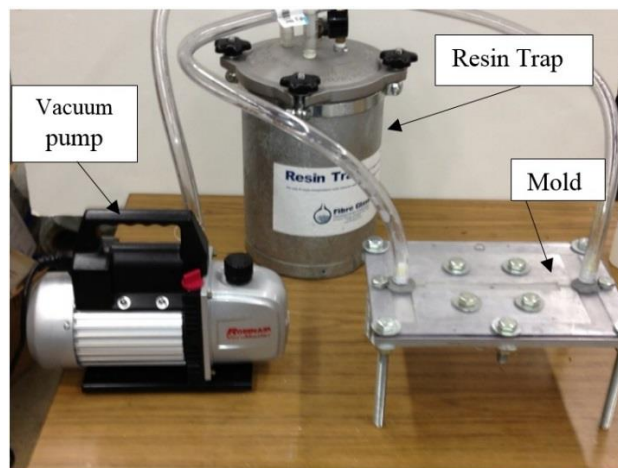


*Figure 2. Processing of CNF Composite using the improvised LCM setup*

The epoxy used in all these experiments was Super-Sap Entropy (by Entropy Resins, Hayward, CA) a low viscosity resin produced for the VARTM process [27]. This epoxy is made up of 37% bio-content that was derived from the byproducts of green industries including those involving wood pulp and bio-fuels [27]. The resin is classified as a USDA Bio Preferred SM Product using ASTM D638 [28]. The resin has a total calculated biomass of 50%. A schematic of the tensile specimen based on ASTM D638 is shown in Figure 3.

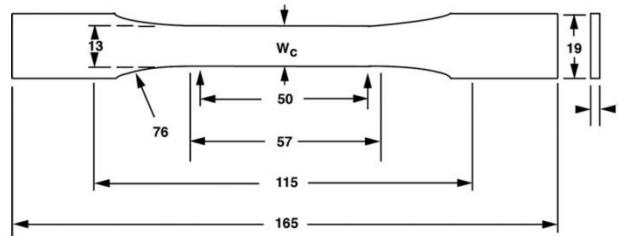


Figure 3. A schematic of the tensile-test specimen

After applying a mold-release agent to the inner mold surface, the CNF preforms were placed inside the mold cavity and the polycarbonate top plate was closed in order to seal the mold. A vacuum pressure was set to 100 KPa approximately during the resin ‘pulling’ process. The resin entered the mold from the inlet and flowed through the CNF preform, and filled the mold cavity, and then came out from the vent onto the resin trap. In order to observe the effects of using the chosen silane agent on mechanical properties of CNF composite, a number of CNF composites were made using silylated preforms and their mechanical properties were compared with the non-silylated samples. For the curing process, the specimens were left in the mold for 24 hours at room temperature. After the removal of the composites’ specimen from the mold, they were put in an oven for post curing at 120 C for 10 minutes. The specimens were then polished further to obtain a suitable surface finish. Likewise, the edges were machined using a low-impact grinding machine



and a high-grit sand paper. The cellulose nano-composites and pure resin specimens made by the improvised LCM setup are shown in Figure 4.



*Figure 4. The CNF and pure resin specimens created for the tensile test.*

### **1.3. Microstructural characterization**

DSC scans were performed on a TA Instruments Q20 with hermetically sealed aluminum pans. All samples were 6-10 mg and monolithic to ensure good surface contact and heat transfer. The DSC profile was a Heat/Cool/Heat cycle from 0°C to 200°C at a rate of 10°C/min. The glass transition temperature ( $T_g$ ) was taken as the point of inflection in the glass transition region.

SEM images were obtained on a LEO 1530 FESEM with a 3kV accelerating voltage using an in-lens detector and a working distance of 1.3 mm. Cross sectional samples of the tensile bars were prepared via fracturing. The samples were gold coated for 30s at 45mA in a Denton Vacuum Desk V sputter coater. All image processing was done in ImageJ [29]. Water Contact Angle (WCA) for the silylated and neat samples was measured on a Dataphysics OCA 15 Optical Contact

Angle Measuring System. Images were taken in triplicate at 0s, 5s, 10s, and 15s at various spots on the sample. The WCA was measured with the supplied SCA-20 software.

#### **1.4. Mechanical Characterization**

Dynamic mechanical analysis is a viscoelastic technique that monitors property changes due to a temperature and/or a frequency or a time change. The technique measures the total energy stored and dissipated in the material due to a dynamic stimulus. The viscoelastic properties are obtained from elastic and viscous responses. The elastic response is a measure of the energy stored in the material and yields the storage modulus ( $E'$ ). The viscous response, on the other hand, measures the energy dissipated in the material due to friction and internal motions, and yields the loss modulus ( $E''$ ).

The effect of CNF reinforcement on the viscoelastic properties was examined using the dynamic mechanical analysis. The study was carried on a Q800 DMA TA instrument (by TA instruments, New Castle, Delaware, USA). A three-point bending mode with a controlled strain mode of 15  $\mu\text{m}$  (displacement) was used. Samples fabricated from pure epoxy and from epoxy reinforced with CNF (with and without silylation treatment) using the LCM method were tested at a constant frequency of 1.0 Hz. A temperature range of 0-80 °C (32-176 °F) and a heating rate of 5 °C/min (9 °F/min) were chosen. The tested samples were approximately 35 x 12-15 x 1.5-2.0 mm (1.4 x 0.5-0.6 x 0.06-0.08 in) in length, width, and thickness, respectively. The supported span width was 20 mm (0.8 in). The test parameters were chosen to comply with the general recommendations of the ASTM D4065-12 and ASTM D5023-07 standards.

The tensile testing for the CNF/epoxy composites and pure epoxy specimens were performed in a displacement-controlled mode at a rate of 1.3 mm/min (0.05 in/min). During the test progress, the crosshead displacement and load values were simultaneously recorded. The load

was applied using an electro-mechanical test system with a 97.8 kN (22 kip) capacity. A load cell with a capacity of 2.2 kN (0.5 kip) was employed to obtain more accurate results. The maximum error of the recorded load was within 22 N (5.0 lb). Since the same operators using the same test machine tested all specimens in a uniform manner, the operator induced errors were minimized. Four CNF/epoxy samples with fiber volume fractions ranging from 1 to 1.3% were tested. Results were compared to those of pure epoxy resin samples, which were used as controls.

## **1.5. Results and discussion**

### **1.5.1. DMA Results**

The results from the dynamic mechanical analysis are shown in Figure 5, Figure 6 and Figure 7. Figure 5 shows a decrease in the storage modulus for the CNF-reinforced samples compared to pure epoxy. However, the silylated sample shows a better behavior and higher storage modulus compared to the non-silylated ones. Figure 6 and Figure 7 show the effect of adding the CNF reinforcement to epoxy on the loss modulus and tan delta plots. Both plots show a peak shift to lower temperatures for the samples reinforced with microfibrillated cellulose scaffolds, which indicates a reduction in the glass transition temperature for the CNF-based composites compared to the pure resin samples. Some studies [30] have replicated this result while others have shown the opposite behavior of the addition of CNF increasing the  $T_g$  [31].

The glass transition temperature for pure epoxy as characterized by the tan delta curves peaks, is around 67 °C (153 °F) and drops to 59 °C (138 °F) for the composite with the silylated CNF reinforcement. Note that the latter figure is close to the  $T_g$  of around 61 °C (142 °F) for the non-silylated CNF based composite. Reinforcing of polymers usually increases the glass transition temperature. Hence, the reduction seen in the transition temperature might be interpreted as an incomplete cure of the resin. The curing process may be slowed or inhibited by the presence of

nano-cellulose [30]. This interference with the curing might not show in the results of DSC or DMA, as a small amount of crosslinking in the later stages of curing can significantly affect the mechanical behavior but requires such a small amount of energy that it is not captured by the calorimetry. The effect on the mechanical behavior might also explain the reduction seen in the storage modulus plots for the microfibrillated cellulose-reinforced specimens. In order to verify the reasons for the reduction in the mechanical properties and the glass transition temperatures, more experimentation should be conducted to interpret the interaction between the resin and the cellulose scaffolds and how it is affecting the thermal and mechanical behavior of the composites. The peak intensities of the cellulose-reinforced samples for loss modulus and  $\tan \delta$  are also remarkably lower compared to neat epoxy samples. The reason for that can be attributed to the interaction between the resin and nano-cellulose which restricts the segmental mobility of polymer chains in the vicinity of reinforcements [31, 32].

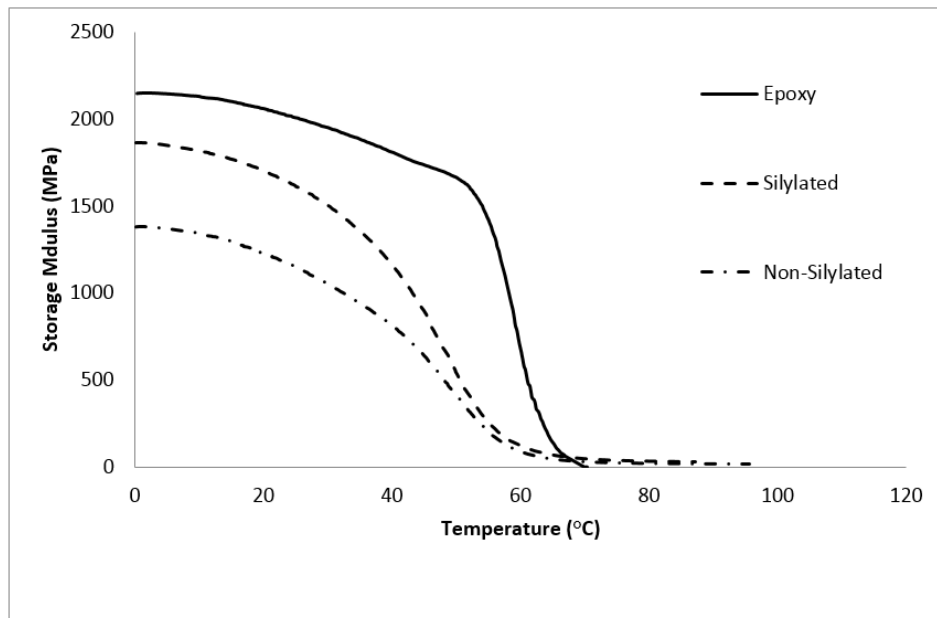


Figure 5. DMA storage modulus plots for pure epoxy and CNF/epoxy specimens

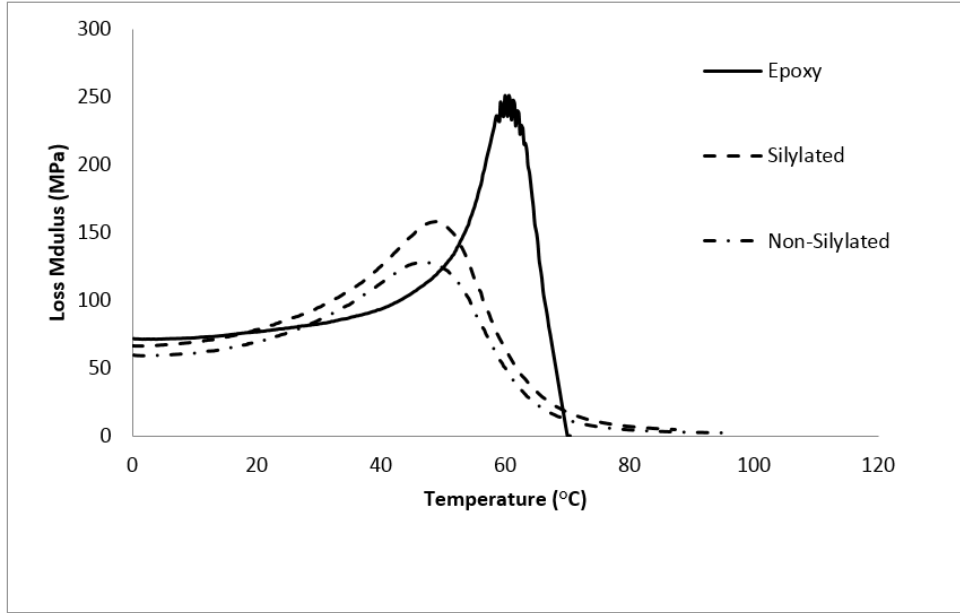


Figure 6. DMA loss modulus plots for pure epoxy and CNF/epoxy specimens

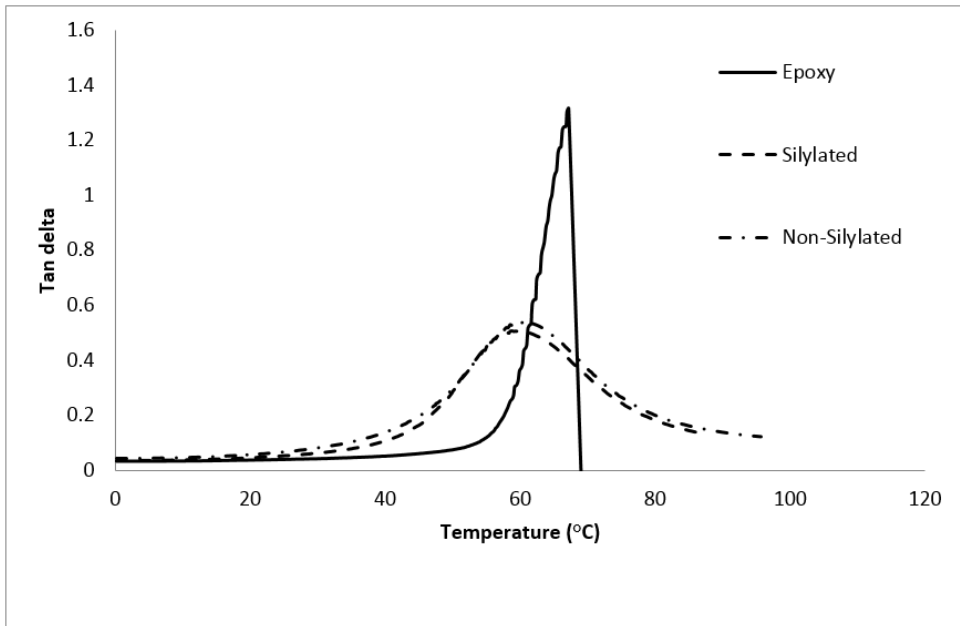


Figure 7. DMA tan delta plots for pure epoxy and CNF/epoxy specimens

### 1.5.2. Tensile test results

Figure 8 shows the experimentally measured stress-strain curves for the pure epoxy samples and CNF reinforced samples with a reinforcement level of 1 and 1.3 vol.%. It is clear that

certain CNF composites have a higher modulus of elasticity compared to pure epoxy: on average, the elastic modulus of the silylated CNF reinforced coupons was observed to be 15% higher.

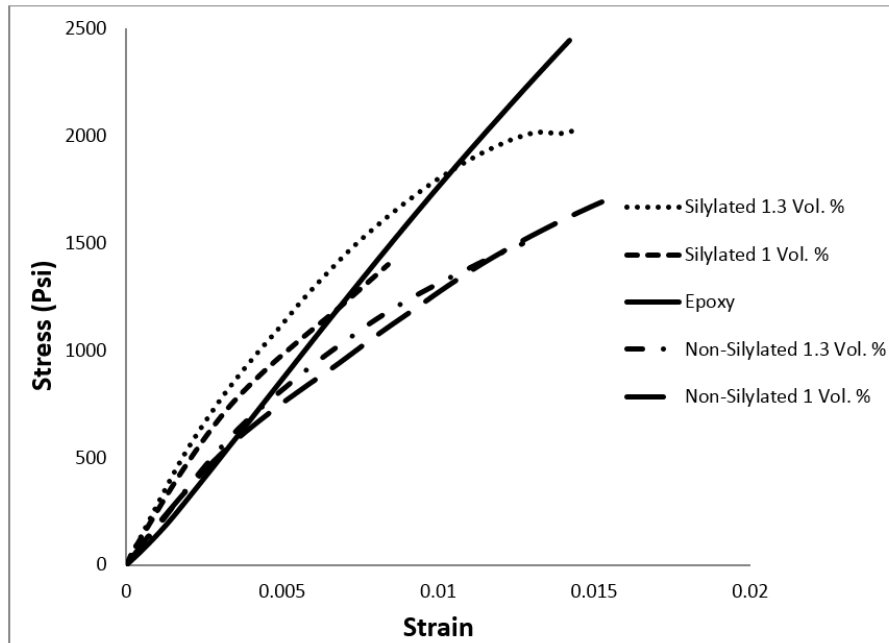


Figure 8. The experimentally measured stress-strain curves for the CNF reinforced and pure epoxy samples

Comparing the response of the silylated and non-silylated specimens, the elastic modulus and ultimate stress of the former is higher. The modulus of the non-silylated CNF composite, which is almost equal to that of pure epoxy in the beginning, declines with an increase in strain. In general, the CNF reinforced specimens showed a nonlinear stress-strain response that was different from the more linear (and more brittle) response of the pure resin specimens<sup>1</sup>.

Additionally, despite the higher mechanical properties of the silylated samples compared to pure epoxy, the former still could not show any significant increase in stiffness and failure

---

<sup>1</sup> According to our experiments, the mechanical properties obtained for pure epoxy did not match the properties as claimed by the manufacturer. There was also a question of inconsistency in resin properties. Also observed were some problems in the flow properties of the resin that may have led to incomplete infusion of the CNF preforms. In future, a more reliable and consistent resin will be considered.

stresses compared to the latter. The reason for this might be the presence of weaker regions in the CNF specimens resulting from the formation of dry spots in CNF preform due to incomplete impregnation by the resin. Further investigation of the mechanical properties using more advanced techniques including nano-indentation can be used to investigate local variations in mechanical properties.

### 1.5.3. Water contact angle measurements

Water contact angle (WCA) is a measure of the hydrophilicity or hydrophobicity of a material's surface. A contact angle of greater than  $90^\circ$  signifies hydrophobicity [33]. Measurements on the CNF preforms show that the silylation process dramatically increases the hydrophobicity of the material which is shown in Figure 9. Note that the contact angle for non-treated CNF could not be measured as the droplet was immediately absorbed, and hence it is not shown in Figure 9. This increased hydrophobicity due to silylation allows the CNF to be easily wetted by the non-polar epoxy resin in the porous structure of the preform during the LCM process. The improved interaction between the resin and fiber provides for a stronger adhesion between the two, thus allowing for better stress transfer [34-36].

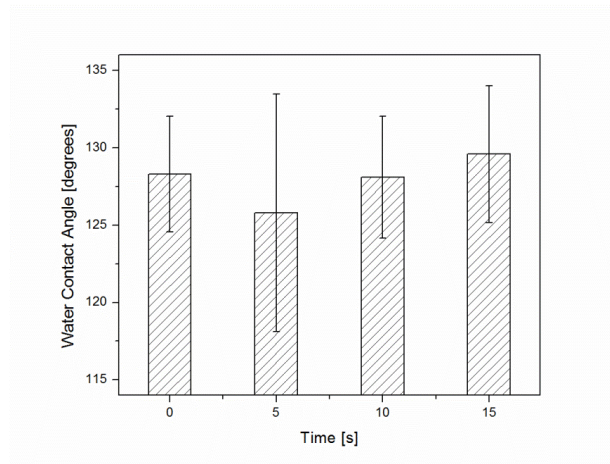


Figure 9. Water contact angle (WCA) measurements for silylated CNF at 0, 5, 10, and 15 seconds after the droplet is placed on the sample.

#### 1.5.4. DSC results

The DSC results shown in Figure 10 and Figure 11 are the first heating and second heating profiles. Even after implementing a post-curing process of 120°C for 10min, all of the samples had some amount of residual cure evident by the change in shape of the plots from first heating to second heating. The dips and rises in the first heating plots are due to a glass transition (around 45° C), degradation, and curing reactions above the  $T_g$ . Degradation peaks are exotherms, and curing reactions or crosslinking events are endotherms. Only the glass transition temperature ( $T_g$ ) remains in the second heating plots as all reactions at the probed temperatures have already occurred in the first heating. The first heating plot for silylated samples is characteristic of latent moisture in the sample, which is expelled and not observed in second heating [37].

The  $T_g$  for each sample, as measured by the point of inflection in the glass transition region, is generally representative of the relative amount of cure attained in the sample. It is observed that inclusion of CNF, whether silylated or not, has the effect of lowering the measured  $T_g$ . Table 1 shows the  $T_g$  of each sample during the first and second heating. The pure epoxy sample has the highest  $T_g$  which generally signifies a higher degree of cure, however it can be noted that the non-silylated sample has a flatter first heating curve which is a representation of the amount of curing being performed during the test; the flatter the curve, the less exothermic and endothermic reactions taking place. This result could also be a symptom of poor heat transfer from the sample to the sensor – a systematic problem for all of the samples that have CNF. In light of the DMA results, the more likely conclusion is that the *inclusion of CNF lowers the ability of the resin to attain a proper level of cure*. The true nature of the change presented by the CNF is unclear but strongly affects thermal and mechanical transitions as well as strength of the composite.



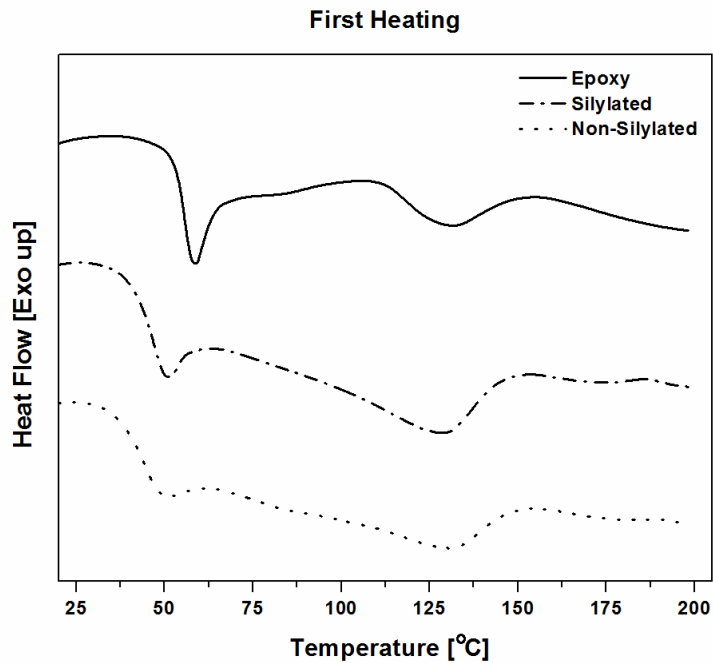


Figure 10. First heating DSC profile

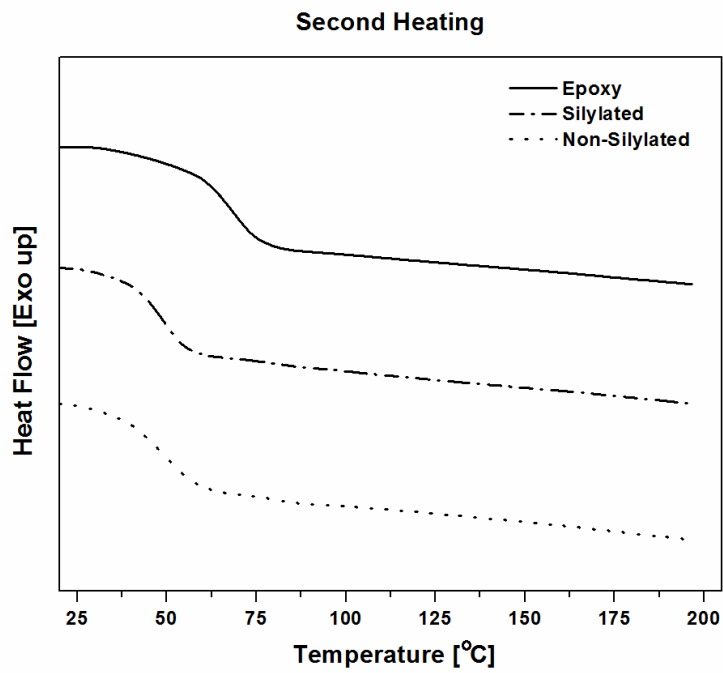


Figure 11. Second heating DSC profile

Table 1.  $T_g$  of each sample during first heating and second heating

<b>Glass Transition Temperature [ ° C] in DSC</b>			
<b>Sample</b>	<b>Epoxy</b>	<b>Silylated</b>	<b>Non-Silylated</b>
<b>First Heating</b>	55.93(±2.91)	46.40(±0.28)	44.37(±0.84)
<b>Second Heating</b>	68.63(±0.86)	49.79(±0.17)	48.63(±2.26)

### 1.5.5. SEM results

SEM results (Figure 12, Figure 13, Figure 14) indicate that the pure epoxy sample fractured in a brittle manner and had little voids or bubbles. The silylated samples show many voids marked by rounded or curved edges and some areas of exposed CNF mesh, denoted by a fibrous mat structure. The non-silylated sample's voids are less numerous and of a more angular shape. The difference in the shapes of the voids is most likely due to hydrophobicity differences and resin preparation causing bubbles in the epoxy resin to be introduced during the mixing and vacuum-suction driven mold-filling processes. Despite the silylated sample's better wettability of the resin, these introduced bubbles become trapped in the pores of the CNF preform whereas the relatively bubble-free resin in the non-silylated sample does not introduce bubbles, but still non-uniformly penetrates the complex pore network of the CNF preform leaving more angular shaped voids. The solid areas of the silylated samples indicate good wetting and bonding at the fibers-resin interface.

Because there is no evidence of CNF fiber pull-out, the decrease in mechanical properties of the CNF composites from the neat matrix can be explained as follows: for the non-silylated sample, poor bonding between the resin and CNF, combined with the tortuous pores of the freeze-dried preform limit the ability of the resin to transfer stress to the fibers. The voids contribute to a smaller cross sectional area and introduce stress concentrations [34, 35]. In the case of the

silylated samples, the bubbles in the resin contribute to similar effects observed in the non-silylated sample, but the smaller size and amount of bubbles leads to less decrease in the mechanical properties than the non-silylated samples. Even though the treated CNF preforms have increased wettability, it has been noted in the literature by several authors that silanes functionalized with long chain aliphatics, such as trimethoxy hexadecylsilane (16 carbon chains) do not bond covalently with the epoxy resin. This results in a reliance on mechanical entanglement between the epoxy and aliphatic chains (in this paper octadecyl = 18 carbon chain) and van der Waals forces which are significantly weaker than covalent bonds [34-36, 38].

While the processability of the silylated preforms is increased due to the enhanced wettability and the application of laser cutting during preform preparation, better control over latent moisture and bubbles in the resin is needed to fully take advantage of the strength of the CNF fibers. In the same vein, silanes that contain amino- or mercapto- functionalities can be used to create covalent bonds with the epoxy while still maintaining a high degree of hydrophobicity [34-36].

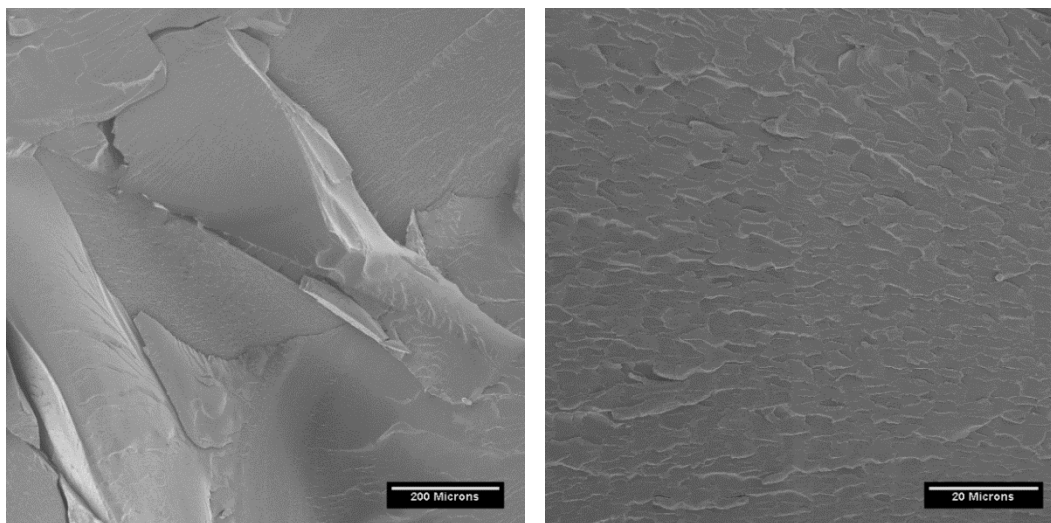


*Figure 12. SEM figures of pure resin*

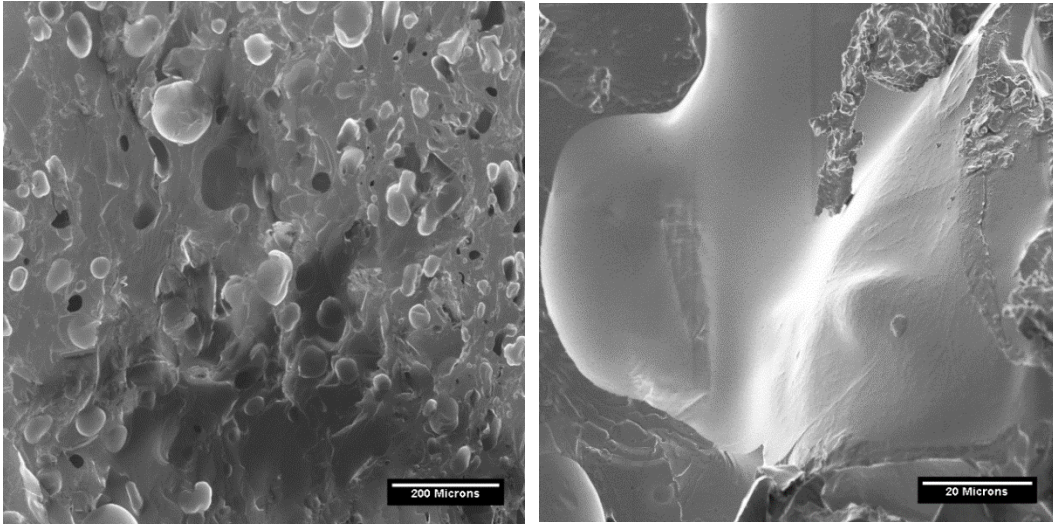


*Figure 13. SEM figures of silylated Sample*

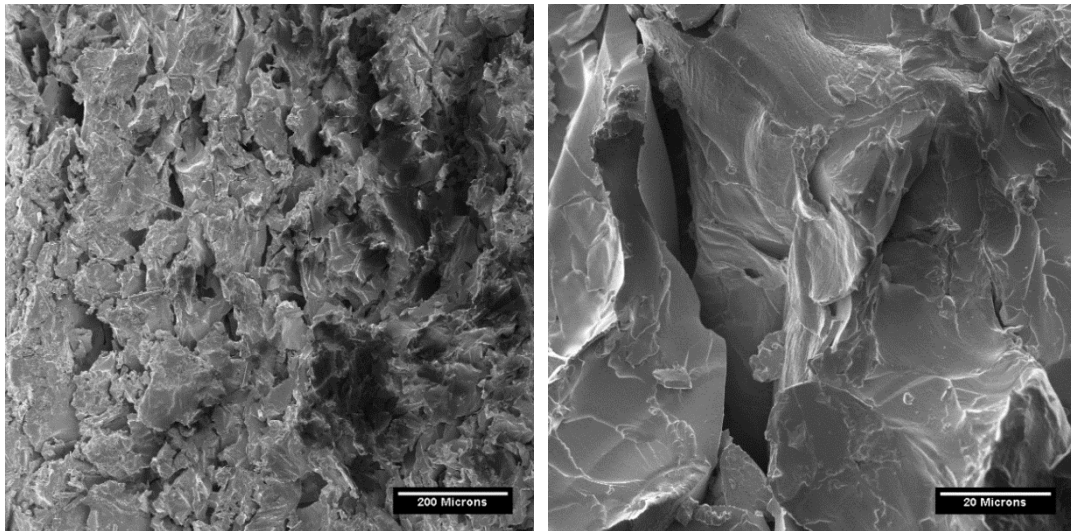


*Figure 14. SEM figures of non-silylated Sample*

## **1.6. Summary & Conclusions**

In this chapter, the epoxy based composites reinforced with silane and non-silane treated CNF preforms were prepared using an improvised LCM type liquid molding process involving vacuum suction of epoxy resin into the preform. Mechanical properties were investigated using DMA and tensile tests. In addition, DSC and SEM tests were employed to study the effects of silylation on the curing process, glass transition temperature and wettability. The investigation

performed reveals that, the silane treated samples show superior mechanical behavior and higher storage modulus compared to the untreated (non-silane) samples. The DMA results also indicate a reduction in the glass transition temperature for the CNF composites compared to the pure resin samples. The tensile results show higher elastic moduli in composites made from silane treated CNF preforms compared to the non silane-treated preforms. The silane-treated composites show higher elastic modulus compared to the pure epoxy samples. The poor mechanical properties of the epoxy used in making the CNF-reinforced composite could be one of the significant reasons for achieving moderate properties in the made CNF composites. The DSC results indicate that inclusion of CNF lowers the ability of the resin to attain a proper level of cure. Indeed, the glass transition temperature was found to decrease in samples with CNF preforms as confirmed by the DMA results. The solid areas of the silylated samples in SEM figures indicates good wetting and bonding at the fibers-resin interface, compared to the non-silylated samples.

## **CHAPTER 2: Study of the Anisotropic Cellulose Nano-Fiber based Composite**

### **2.1. Introduction**

In recent years, the use of natural fibers as a reinforcement in polymer composites has increased in several sectors of engineering such as automotive, aerospace, construction, etc. The growing awareness about the consequences of using synthetic fibers made from fossil resources and increasing demand for environmental friendlier products have enhanced industrial interests in the development of sustainable and renewable composites with lower impact on environment [39, 40]. The natural fiber composites, also categorized as green composites, are one such material. Most recent reports in climate change recommend reduction of greenhouse gas emissions by 70% and increase in the use of clean energy by 2050. As a result, effective strategies such as replacing sustainable, environmental friendly materials with synthetic, fossil-resource based products can decrease the effects of the greenhouse gas and climate change on the environment [41]. Advantages of using natural fibers include economic viability, non-toxicity, biodegradability, low cost machining and enhanced energy recovery. Because of these properties, natural fiber composites have often been used as a substitute for glass- or carbon-fiber composites for reinforcement in secondary structural applications such as door panels, package trays, etc. in industry, especially the automotive sector [40] [42-46].

Responding to the increasing needs for natural composites, various kinds of natural (plant) fibers could be used to make such green composites. Examples of such fibers include cotton, jute, kenaf, coir, and flax. Shih [47] studied the mechanical properties of wastewater bamboo husk fibre/epoxy composites where the addition of treated fiber improved the mechanical properties of composites. Maleque et al. [48] reported an increase in flexural strength by 40%, when banana woven fabric was added to the epoxy matrix. However, the increase in the mechanical properties

is not as much as expected. For instance, for the hemp-fiber/epoxy bio-composites, the tensile strength was limited to 60 MPa at a fiber content of 40 % by weight [21], when the single-fiber strength could be as high as 900 MPa [22].

Natural fibers have typically lower mechanical properties compared to carbon and glass fibers [19]. As a result, the current types of natural-fiber composites suffer from the lower strength and fatigue properties compared with the carbon or glass-fiber based polymer composites.

Cellulose nano-fibers (CNFs) are a novel material made purely from cellulose molecules, have interesting properties compared to other natural fibers, such as enhanced rigidity, low thermal expansion and high surface area, especially at the nanoscales [49]. The first use of nanocellulose as reinforcement in polymers, namely polypropylene, polystyrene and polyethylene, was reported by Boldizar et al. [50]. They found that the tensile modulus increased from 2.4 GPa for neat polystyrene to 5.2 GPa for polystyrene reinforced with 40 wt.-% nanocellulose. The first efforts in making the polymer-matrix biocomposites from high volume fractions of CNF and thermoset polymer matrices resulted in brittle materials [11-13]. CNF has also been used as a reinforcement in different types of nano-composites [14, 15]. Khalid *et al.* [16] investigated using cellulose fillers compared to cellulose fibers with propylene matrix and reported attaining higher mechanical properties. Low et al. [51] reported a significant increase in flexural strength, modulus, fracture toughness, impact strength and impact toughness of cellulose-fiber reinforced epoxy composites. In another study, Barari et. al. employed chemically treated, isotropically porous CNF preforms made from freeze drying process with bio-based epoxy matrix in Liquid Composite Molding (LCM) process and made cellulose nano-composites. Their investigation revealed that using chemical treatments improved modulus of elasticity as well as tensile strength [52].

CNF's appeal as a reinforcement has increased because of recent reductions in energy required for breaking down cellulose fibers into nano-fibers thereby reducing its cost [18]. Despite the enormous advantages presented by cellulose fibers, natural composites made from CNF suffer from several limitations, such as low mechanical properties due to poor interface between the reinforcement and the matrix [19, 20]. Other limitations such as, moisture absorption, low wettability and hydrophilic nature of cellulose (because of hydroxyl groups) reduces the dimensional stability and mechanical properties of such composites [53-55]. As a result, more studies need to be conducted in order to improve resin absorption and wettability in the presence of highly porous structures found in cellulose which lead to lower number of voids and cracks and results in higher mechanical properties.

In this chapter, a novel and anisotropic CNF preform with highly aligned pore structure was made through the freeze-drying method and was used as reinforcement in a biobased epoxy resin, that was partly sourced from plants. Using the freeze-drying method, the suspension of CNF was converted into a form of aerogel that was extremely light-weight and had highly aligned pore channels. The composite was made using an improvised, vacuum-suction driven liquid composite molding (LCM) process. It was presumed that the resin infiltration in such CNF preforms would be increased owing to high porosity (above 95%) and aligned pore structure of the resultant porous medium, and this in turn would lead to the making of composites with high mechanical and micro-structural properties. In isotropic CNF samples, fibers were dispersed randomly in epoxy resin while in anisotropic CNF composites, fibers were in a form of clusters. The basic idea was to improve bonding between CNF and resin by constructing highly aligned channels in anisotropic CNF's micro structure in order to improve the movement of the resin in the CNF preform.



The mechanical behavior of the resulting CNF nanocomposite was evaluated by experimental methods. The tensile strength was estimated using the traditional mechanical testing while the storage modulus, loss modulus and tan delta results of the samples were characterized through DMA. The causes of the failures were investigated using SEM. The effect of silane treatment on the mechanical properties of nano composites was also studied by comparing the strengths of the treated/non-treated samples.

## **2.2. Sample preparation process**

### **2.2.1. Cellulose nano-fiber preforms**

This process of making CNF preforms was carried out at BIONATES labs Lab of the University of Wisconsin, Madison. The CNF aerogel used in this study were derived from Eucalyptus Kraft pulp and processed through TEMPO oxidation, acid hydrolysis and mechanical stress. The CNF aerogel preparing process was initiated with washing, pre-treating and soaking of the Eucalyptus Kraft pulp with acid and water, and then filtering the pre-treated fibers. After filtration, the products were carboxylate with reactants according to the Saito's methodology [26]. The centrifugation process was employed to facilitate the separation of coarse and fine fractions. Then, a nano-fiber suspension was prepared using microfluidizer. In the final step, the CNF preforms were prepared from the nano-fiber suspension using the freeze-drying process. Several aluminum blocks (3" x 1") are added to a styrofoam container (8" x 8" x 5") so that the highest level of the block is near the top of the container. Liquid nitrogen is added to the container until the level of the liquid nitrogen is just below the level of aluminum and the nitrogen ceases to boil. A room temperature solution of 0.5% CNF is poured into cylindrical glass vials (29mm diameter, 65mm height) to  $\frac{3}{4}$  of the way to the top of the vial (to allow for expansion of the material during freezing). The solution filled vials are placed on the cold aluminum blocks and allowed to freeze

from the bottom up over a period of several minutes. Liquid nitrogen is continuously added around the blocks as needed to maintain the same level. The process is finished when the material at the top of the vial is frozen. The vials of directionally frozen CNF solution are placed in a Labconco FreeZone 4.5 lyophilizer under a vacuum of 0.01 Torr and a collector temperature of  $-50^{\circ}\text{C}$  with a reference sample vial of ice water. Samples are left for several days until the reference sample has been completely sublimated.

### **2.2.2. Making cellulose nano-composites using an improvised LCM process**

The CNF composite samples were made by using the anisotropic CNF preform as the reinforcement and a bio-based epoxy resin (Super Sap CLR epoxy) as the matrix in an improvised micro LCM process. Our improvised LCM process is essentially based on the conventional resin transfer molding (RTM) process done using a hard mold while a negative vacuum pressure is applied to create 100 kPa pressure differential to pull the resin through the CNF preform. The experimental setup, consisting of the micro LCM mold, the resin trap and a vacuum pump, is shown in Figure 15. The micro LCM mold was made from an aluminum slab at the base, which had a cavity machined on to the surface, and sealed by a transparent polycarbonate plate at the top. Two aluminum portable inserts, joined to create a mold cavity for making the final tensile and flexural specimens, were placed inside the machined cavity of the base slab. The transparent Lexan® top plate was employed to air seal the mold and also used as a window to track the resin movement inside the mold.

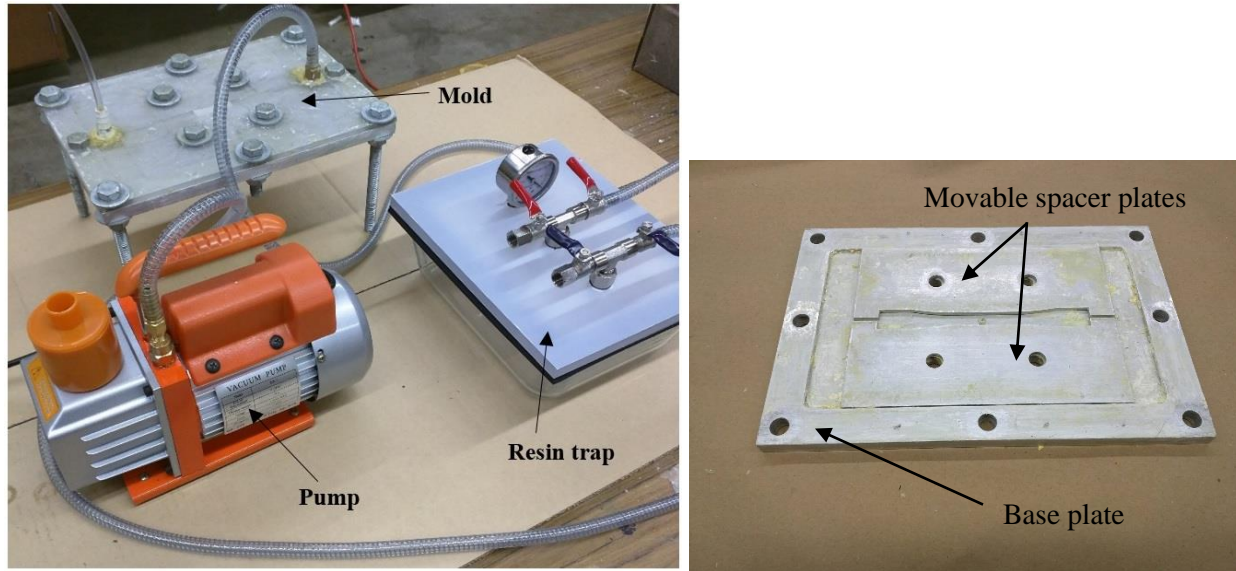


*Figure 15. The improvised vacuum-driven LCM setup and the bottom mold plate with removable two-piece spacer-plate insert*

For making the specimens, the cellulose preform (cut out from the CNF material to be shaped like the ASTM dog-bone D4065-12 standard specimen) was placed inside the specimen cavity while the top polycarbonate plate was fastened on the top of the base slab. The inlet vent was connected to a tube which is dipped into a beaker full of the curing resin and the outlet vent was connected to the vacuum pump through a resin trap in order to prevent any leakage of the resin to the inside of the pump. During the process, the thermosetting resin flows upward through the inlet tube, fills the inlet mold cavity, and passes through the dog-bone shaped CNF preform placed in the mold cavity and is then sucked out to the resin trap through the outlet vent. The resin was set and cured for 24 hours and then the specimen was removed from the mold. After the removal, the specimens were put inside an oven kept at 130 °C for 20 minutes, as per the recommendation of the isothermal DSC experiment learned from authors' former investigations into the making and testing of CNF composites [56]. The specimens were then polished further to

obtain a suitable surface finish. Likewise, the edges were machined smooth using a low-impact grinding machine and a high-grit sand paper.

### **2.3. Microstructural and mechanical characterization**

The fracture surface samples were created via tensile test and studied by means of scanning electron microscopy (SEM). SEM images were obtained by a JOEL JSM-6460LV with a 15 kV accelerating voltage using back scatter electron beam and a working distance of 12 mm. The samples were Palladium coated for 30 s at 45 mA in a Denton Vacuum Desk II sputter coater before imaging.

The effect of CNF reinforcement on viscoelastic properties was examined using DMA. The study was carried on a Q800 DMA TA instrument. A three-point bending mode with a controlled strain mode of 15  $\mu\text{m}$  (displacement) was used. Samples fabricated from pure epoxy and from epoxy reinforced with CNF (with and without silylation treatment) using the LCM method were tested at a constant frequency of 1.0 Hz. A temperature range of 0-100 °C and a heating rate of 5 °C/min (9 °F/min) were chosen. The supported span width was 20 mm (0.8 in). The test parameters were chosen to comply with the general recommendations of the ASTM D4065-12 and ASTM D5023-07 standards.

The stress-strain behavior of CNF/epoxy composites and pure epoxy was determined by applying tensile load on samples. The tensile testing was carried out on specimens by controlling displacement at a rate of 1.3 mm/min (0.05 in/min) using electromechanical test system with a 97.8 kN (22 kip) capacity and utilized by extensometer to obtain strain. In order to achieve more accurate results, the testing machine was equipped by load cell with a capacity of 2.2 kN (0.5 kip). Four CNF/epoxy samples with different fiber volume fractions ranging from 1 to 1.3% were tested and failure results were compared with the reference pure epoxy samples. The failure stress and

strain are respectively the maximum stress and strain that CNF/epoxy composites withstood before breaking. The reported values are the result of individual tests on two replicates.

## **2.4. Results and discussion**

The DMA results for anisotropic CNF composite and pure epoxy samples are shown in Figure 16, Figure 17 and Figure 18. Figure 16 shows an increase in the storage modulus for anisotropic CNF composite compared to pure epoxy while Figure 17 shows a decrease in loss modulus for anisotropic samples compared to pure epoxy. These results show higher strength and stiffness for CNF composites which improves the overall mechanical behavior of the epoxy composite in presence of CNF reinforcements.

The glass transition temperature for pure epoxy, as characterized by the tan delta curves peaks, is around 86 °C and drops to 81 °C for the composite reinforced with anisotropic CNF. Reinforcing of polymers usually increases the glass transition temperature. Hence, the reduction seen in the transition temperature might be interpreted as an incomplete cure of the resin. The curing process may be slowed or inhibited by the presence of nano-cellulose [30]. However, by comparing the DMA results for anisotropic CNF with the isotropic CNF samples (discussed in chapter 1 sec. 1.5.1),  $T_g$  is increased from 67 °C to 81 °C which indicates better curing of the epoxy in presence of the highly-aligned pore structure of anisotropic CNF composites. Another reason for this improvement could be because of better crosslinking and higher mobility of polymer chains in presence of anisotropic CNF compared to the isotropic one.

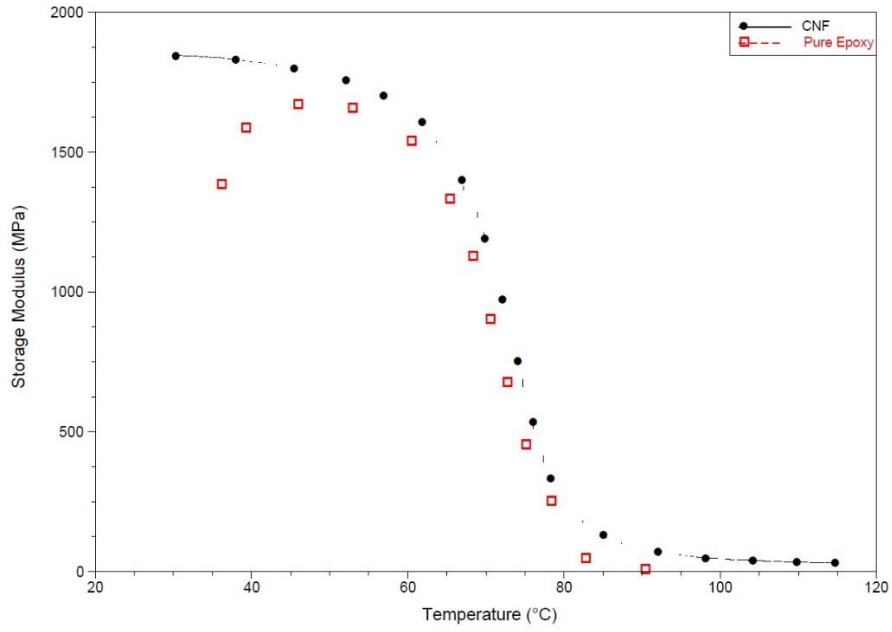


Figure 16. DMA storage modulus plots for anisotropic CNF composite and pure epoxy samples

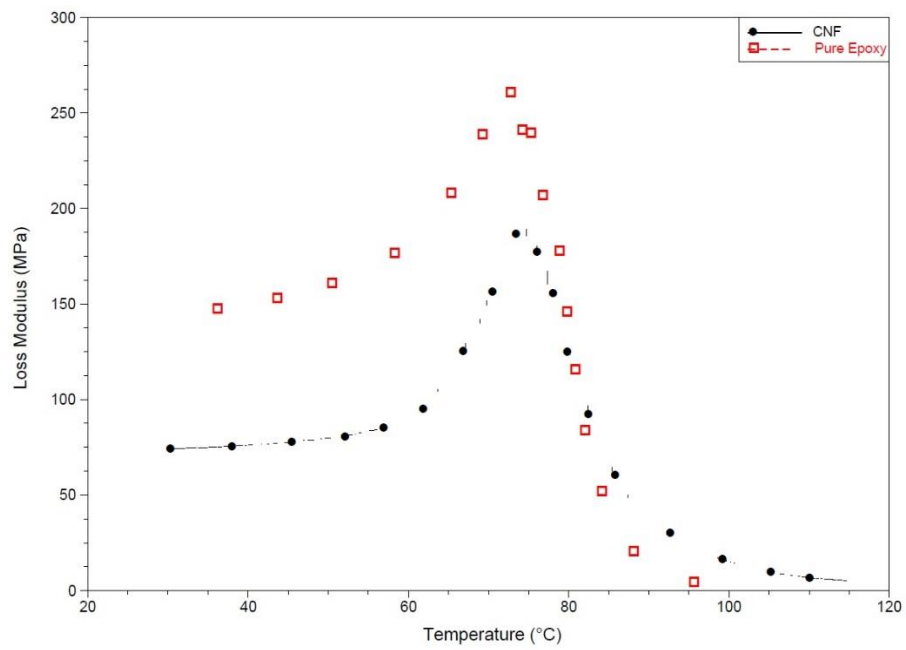
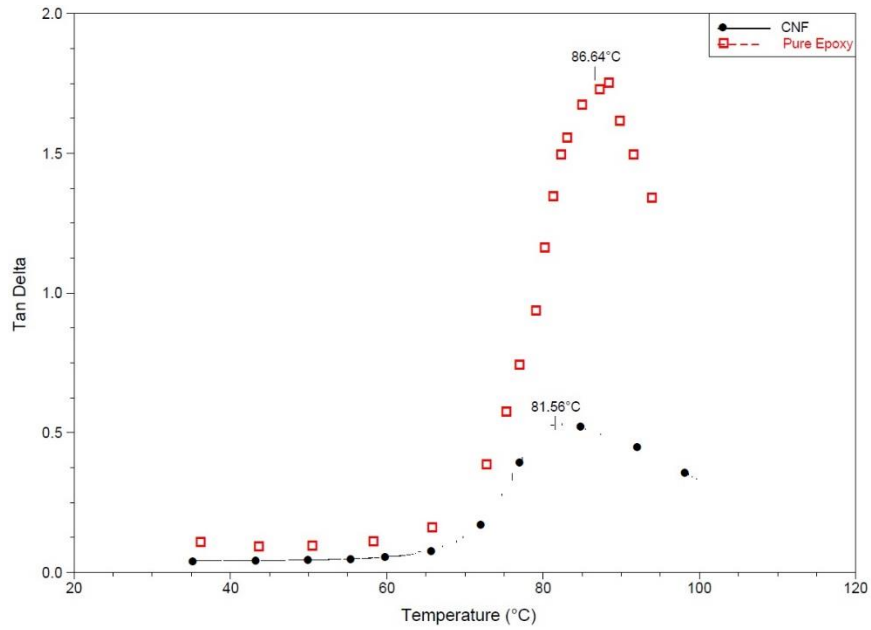
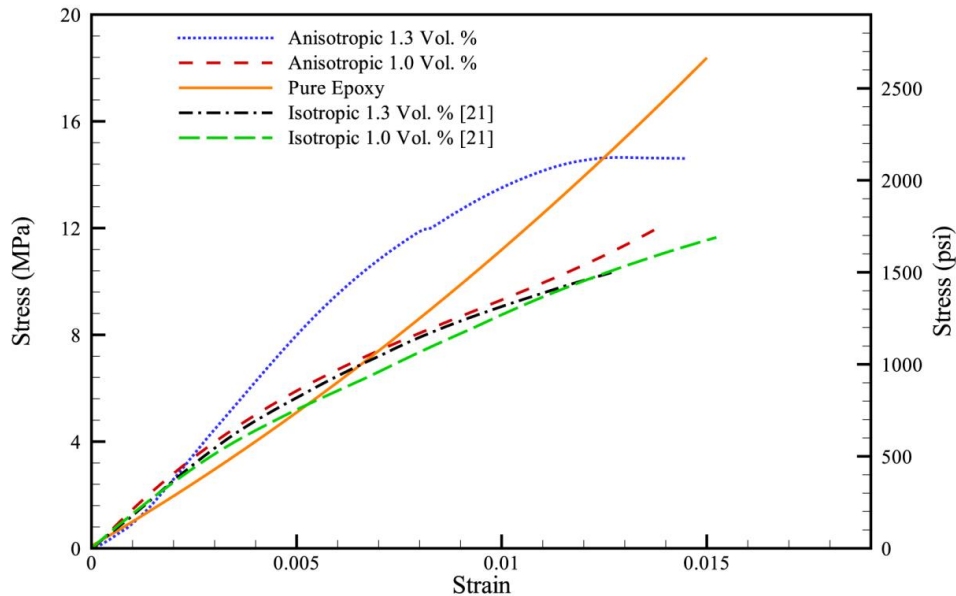


Figure 17. DMA loss modulus plots for anisotropic CNF composite and pure epoxy samples



*Figure 18. DMA tan delta plots for anisotropic CNF composite and pure epoxy samples*

The CNF Composites and pure epoxy samples were subjected to tensile load until the failure occurred on specimens. The stress-strain diagrams of the composite samples were obtained experimentally and then the fracture surfaces were studied using SEM. The stress-strain diagrams of the anisotropic, isotropic [56, 57] CNF composite and the pure epoxy sample are shown in Figure 19.



*Figure 19. The stress-strain diagrams for the anisotropic and isotropic CNF reinforced composite samples and pure epoxy samples.*

In the Figure 19, the stress-strain graphs for anisotropic CNF composites were compared with those for the isotropic CNF composites that were presented in our previous research [56, 57]. It is clear that the modulus of elasticity and ultimate strength of the anisotropic samples were increased by increasing the fiber volume fraction. Changing the pore structure from isotropic to anisotropic also caused an improvement in mechanical properties such that the anisotropic CNF composites showed higher ultimate stress and modulus of elasticity compared to the isotropic CNF composites. Further alterations in the stress-strain behavior of the samples are observable in Figure 19: an almost linear plot for pure epoxy to the increasingly nonlinear plots for CNF composites. This nonlinearity implies that the presence of CNF causes toughening in the samples. The nonlinearity of the anisotropic samples was more than the nonlinearity of the isotropic samples which means the anisotropic samples were tougher compared to the isotropic ones. Higher

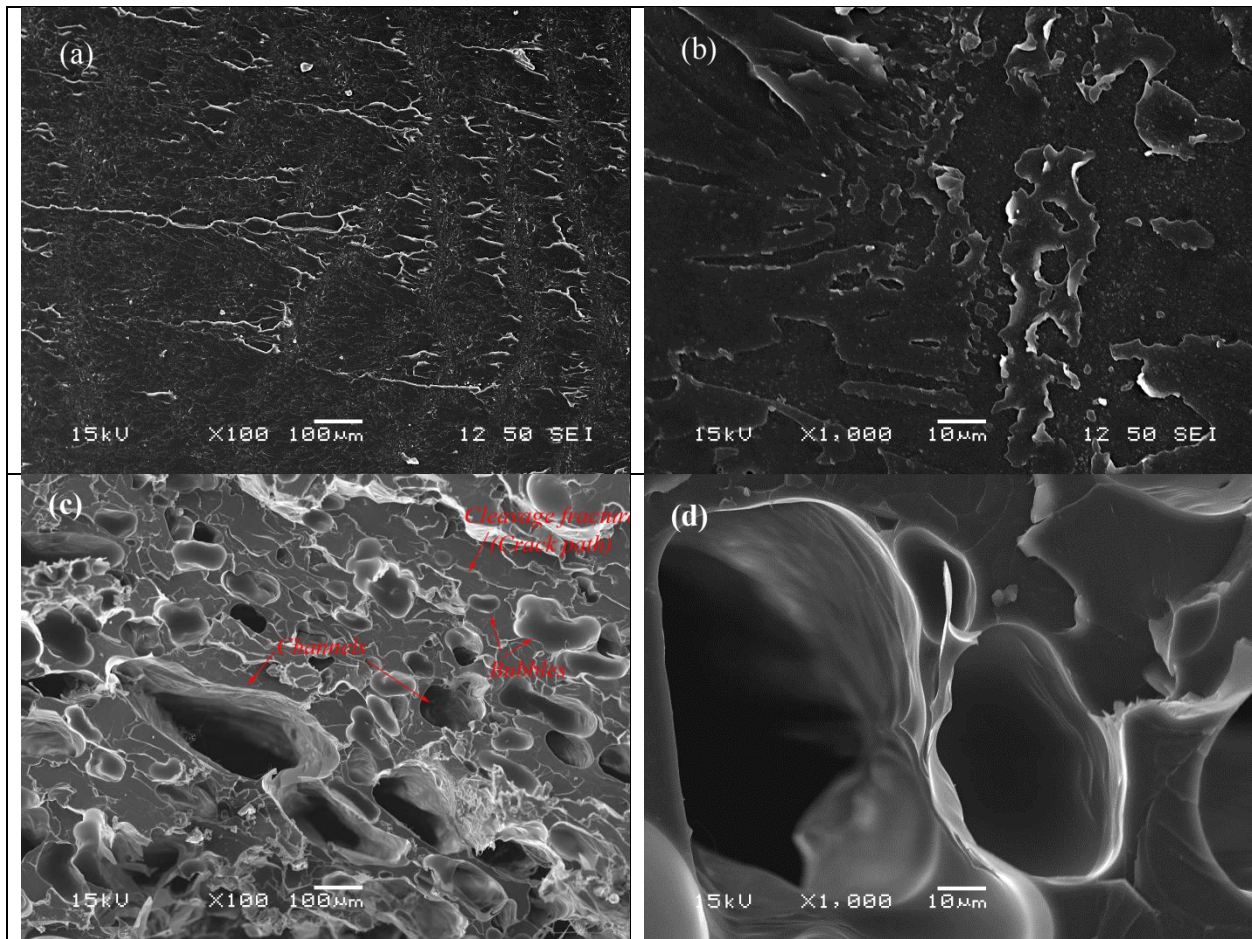


toughness of the CNF samples could be explained by fiber pull out effects or the presence of fibers in the path of a crack during fracture. The honeycomb-like form and highly aligned structure of the solid skeleton of the anisotropic CNF could be one reason that it can deflect the crack and reduce its growth rate. All these lead to an increase in the ultimate strength and other mechanical properties of the composite.

In this study, the fractured surfaces were studied using SEM (Figure 20). The SEM micrographs of pure epoxy displayed regular cracks, indicating a typical brittle fracture. The SEM images showed a uniform fractured surface along with channels and bubbles. The smooth part of the fractured surface indicated that the mode of failure was a cleavage resembling the brittle fracture of metals under tensile tests. Fractured surfaces clearly showed that the fibers clusters have been pulled out and the resultant channels have appeared on the fracture surface. This fiber pulling out appears to be the dominant toughening mechanism for the anisotropic CNF composites. Because of the weaker interfacial bond between the CNF and epoxy, all SEM figures showed smooth surfaces on the channels. Also, the channels, with almost the same size as the holes in the honeycomb shaped aligned pore structure of anisotropic CNF, were perhaps created from the ‘pull-out’ of these individual hollow ‘cylinders’. Bubbles in the epoxy resin were created during the mixing and vacuum-suction driven mold-filling process. The presence of bubbles and the low interfacial bond between CNF solid phase and epoxy resin may be the reasons for having a lower ultimate stress in CNF composites compared to pure epoxy.

Table 2. A comparison of the mechanical properties of the anisotropic and isotropic CNF reinforced epoxy samples and the pure epoxy samples

Samples	Fiber volume fraction (%)	Ultimate tensile stress (UTS) (MPa)	Max Strain	Modulus of elasticity (GPa)
Pure epoxy	0	18.32	0.015	1.14
Anisotropic	1.3	14.64	0.014	1.70
Anisotropic	1.0	12.14	0.014	1.24
Isotropic [56]	1.3	10.29	0.012	1.2
Isotropic [56]	1.0	11.65	0.015	1.08



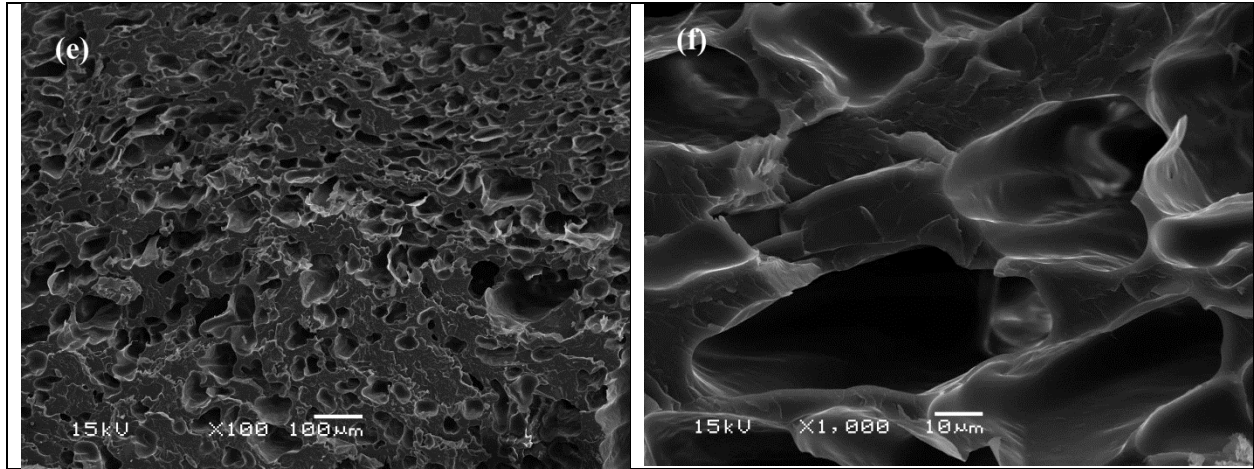


*Figure 20. SEM images of fractured surfaces of samples with different CNF volume fractions and different magnifications: a) Pure epoxy 100x, b) Pure epoxy 1000x, c) 1% CNF 100x, d) 1% CNF 1000x, e) 1.3% CNF 100x, f) 1.3% CNF 1000x*

## **2.5. Summery and Conclusions**

In this study, a type of bio-based epoxy composites reinforced with anisotropic CNF preforms were prepared using an improvised LCM process. Mechanical properties were investigated using the traditional tensile tests and DMA. In addition, the fiber-resin interfaces were studied using SEM micrographs in order to investigate the causes of failure. Our investigations revealed that the anisotropic CNF preform slightly improved the mechanical properties of the bio-epoxy composites. The DMA results also indicate an improvement in the glass transition temperature for the CNF composites compared to the pure resin samples. Also, the glass transition temperature for anisotropic CNF samples was higher compared to the isotropic CNF composites. This means that the new anisotropic CNF composite holds its shape and rigidity till a higher temperature. Also, stronger bonding between the polymer resin and CNF skeleton could be another reason for a higher  $T_g$  and superior mechanical properties. The tensile tests showed higher elastic moduli and ultimate strengths in composites made from anisotropic CNF preforms compared to the composites made from isotropic CNF preforms and compared to the pure epoxy samples.

Finally, the solid areas in SEM figures indicate good wetting and bonding at the interface of CNF solid-phase and resin for the anisotropic CNF composites, compared to the isotropic ones.

## **CHAPTER 3: 2D-Micrograph based Numerical Method of Permeability Estimation in Cellulose nano-Fiber**

### **3.1. Introduction**

The problem of flow and transport of fluids in porous media has been studied extensively in the last hundred years. In the last few decades, the volume averaging method has emerged as a credible method to develop the macroscopic governing equations for modeling fluid flow in porous media [1]. Using these equations, one can predict the volume-averaged velocity, pressure, liquid density, and species concentrations inside any porous medium [58-61].

The basic idea in volume averaging is that the equations for flow and transport in porous media can be extracted using spatial averaging with the help of representative elementary volume or REV [62-64]. Efforts towards developing the volume averaging method were made by several researchers during last few decades. Gray [65] used a generalized function to formulate and prove the volume averaging theorems. The volume averaging method as a powerful technique for upscaling was subsequently used by several authors. Hassanizadeh [66] applied the volume averaging theorem for developing continuum models for multiphase flows in porous media. Bennethum and Cushman [67] used the multiscale hybrid mixture theory along with the volume averaging method to develop continuum equations for swelling porous media. Further studies on upscaling was done by Gray and Miller [68] where averaging of quantities from micro- to macro-scale using a thermodynamically constrained approach was conducted. Whitaker provided perhaps the most comprehensive derivation of the volume averaging theorems based on geometric ideas [69, 70]. Later, Whitaker [1] outlined in detail the volume averaging method based on its *closure* formulations where the macroscopic flow variables were linked to local variations in flow quantities. Such formulations were then used in the derivations of Darcy's law and the volume-

averaged mass-transport equations for single- and multi-scale porous media. Lux et al. [71] combined the volume averaging technique and image analysis to determine the effective thermal-conductivity tensor due to local anisotropy in thermal properties for fibrous materials and obtained good agreement with experimental results.

A great advantage of the volume average method is the development of an effective *micro-macro* coupling, i.e., the coefficients of the macroscopic equations are derived from solving closure formulations in unit cells of real porous media, thus incorporating the effects of pore-scale geometry in the overall upscaled equations. As a result, physical properties such as tortuosity, dispersion, and permeability are estimated after including the features of the microscopic flow, transport and geometry. This approach was used to propose single- and two-equation models for conduction and convection in porous media [72, 73]. A theoretical derivation of the governing equations for the single-phase flow in swelling porous media was investigated by Pillai [74] where novel forms of the mass balance (continuity) and the momentum balance (Darcy's law) were developed using the volume averaging method. A complete flow modeling from pore-scale imaging to absolute permeability tensor estimation was investigated by Guibert [75]. They found that mesh refinement has significant effects on permeability tensor which decreases the difference between the methods of computational measurements. Bear and Bachmat [76] comprehensively presented the volume averaging equations for single-phase, multi-phase and multicomponent systems using some unique and rather complicated proofs of the averaging theorems.

In most real porous media, the size of the REV where volume averaging is done must be much greater than the size of the solid-phase entities (typically particles or fibers) and the characteristic interstitial distances. However, in some with crystal-like microstructure characterized by regularly arranged particles or fibers, the averaging can be conducted in the much

smaller unit-cell employing the benefits of a periodic microstructure. In most studies on scaling up done till now using the closure formulation, a simple square shaped unit-cell with circular solid phase is most often considered [77]. Kim [78] used different aspect-ratio rectangular unit-cells with rectangular inclusions for this purpose as well. Davit [79] worked on local non-equilibrium models for mass transport in dual-porosity, dual-phase porous media where they observed that the volume-averaging-method formulation with the closure and the method of matching spatial moments were equivalent in the one-equation non-equilibrium case. Golfier [80] investigated mass transport in a porous medium containing bio-film to develop the Darcy-scale equations and the effective dispersion tensor using a closure formulation was solved for both cases of simple and complex unit cells.

The use of micro CT scans to map the pore space of a porous specimen in 3D and thus characterize its properties such as porosity and permeability is on the rise [81-83]. Vignoles [84] used high-resolution microtomography to reconstruct 3-D pore space and solved for properties including the permeability and thermal conductivity tensors for a carbon-carbon composite. They found a good agreement between their numerical results and experimental data. Belhouideg and Lagache [85] developed a comprehensive CFD-based model for predicting effective permeability of exfoliated clay as an alternative for asbestos in sealing application. They developed a finite element model using ANSYS to estimate the permeability in samples characterized by SEM micrographs. Guibert [86] numerically evaluated absolute permeability tensors of porous media using core-scale images through several boundary value problems. They also discussed the non-diagonal terms of permeability tensor in isotropic and anisotropic porous media.

In micro-CT based pore-space imaging methods, the following steps are required: reconstruction of the tomographic image, image filtering, segmentation of pore space and fluid

phases, and finally running the fluid-flow model in the pore space. The cost of creating high-resolution tomographic images using micro CT scanners is quite high. (It typically takes several hours in an expensive scanner with high per-hour usage rates to create a high-resolution 3D scan of a small 1 cubic porous specimen.) In fact, the whole process of determining permeability from micro CT images can now be done by commercial software. For example, the permeability is estimated using a single-phase flow numerical simulation in the pore space using 3D analysis software such as Avizo<sup>®</sup> or GeoDict<sup>®</sup>. The permeability is computed by simulating a flow experiment in a specific spatial direction by attaching inlet and outlet distribution elements and imposing periodic boundary conditions on the side walls of a cubic representative elementary volume (REV). Typically, such simulations use the finite volume scheme to simulate Stokes flow and are performed in pores on a length scale larger than the porosity-based REV [87, 88]. Though not very fast, such methods are acceptable for isotropic porous media such as sand or soil. However, for anisotropic media such as those made of oriented rock fissures or aligned fibers, the estimation of full 3D permeability tensor is expected to be quite slow and computationally expensive due to the fact that multiple 1-D flow simulations are required to resolve the full permeability tensor<sup>2</sup> [89]. Note that 3D simulations demand computationally expensive calculations since we deal with much complex 3D geometry and meshes compared to the simpler 2D geometries. In such a scenario, the proposed closure-formulation based method that can estimate the full permeability tensor in a single simulation is marked by fast simulation, low memory and storage requirements, and inexpensive and fast 2-D scanning. Because of these

---

<sup>2</sup> Despite our requests, the companies which are owners of Avizo<sup>®</sup> or GeoDict<sup>®</sup> refused to give us any details of their method of permeability estimation used in their codes.



advantages, the proposed numerical method has the potential of becoming a useful tool in the arsenal of porous-media scientists and researchers.

In this chapter, the porous preform made from cellulose nano-fibers (CNFs) [90] is considered for permeability estimation. CNFs are made purely from cellulose molecules and have very good mechanical property compared to other natural fibers, and even carbon or glass fibers. Recent studies establish that the films or "nano-paper" made from CNFs are the strongest man-made, cellulosic materials [91]. Recently, CNFs have begun receiving serious consideration as potential reinforcement materials. The present research springs from the efforts by the authors on using CNF preforms, porous substrates made using the freeze drying process, for making CNF composites by infiltrating them with thermosetting polymers [52, 57]. CNF preforms used in this study were prepared according to the technique developed by Saito [92].

In this chapter, the closure formulation, developed as a part of the proof for Darcy's law by Whitaker [1], is used to estimate the permeability through the CNF porous media with realistic, irregular pore structures. In the characterization of our porous media, and the subsequent fluid-flow related computations in the pore space, several steps of data analysis were involved. Scanning Electron Microscopy (SEM) was used to take micrographs of the cross sectional areas of the CNF preform. As mentioned before, this method represents a fast, lower-cost method to estimate the permeability – we estimated the permeability from easily-obtained, less expensive 2-D micrographs as compared to the difficult-to-obtain, more expensive micro-CT scan. The SEM micrographs were then transformed into binary pictures (containing only two colors: "white" representing the solid phase, and "black" the void region) and then they were imported into COMSOL multi-physics software. The governing equations for the closure formulation along with the assigned boundary conditions were solved within a unit cell placed at the center of the

micrograph. The permeability tensor could then be obtained from integrating the field of mapping variables inside the unit-cell. In order to check the independence of our results from numerical artefacts, permeability computations were conducted for various mesh sizes and mesh convergence was achieved. Finally, for the CNF preform, the permeability obtained by the numerical simulation was compared with the experimental permeability obtained using the falling head permeameter.

<b>NOMENCLATURE</b>			
<b>B</b>	Closure or mapping variable for velocity	$V_f$	Pore volume or fluid volume
<b>b</b>	Closure or mapping variable for pressure	$V$	REV volume
<b>D</b>	Velocity closure variable in terms of permeability	$x$	Height of liquid during experiment
<b>d</b>	Pressure closure variable in terms of permeability	<b>Greek Symbols</b>	
$f$	Arbitrary continuous function	$\varphi$	Arbitrary flow variable
<b>g</b>	Acceleration due to gravity	$\nabla$	Gradient vector
<b>I</b>	Unity tensor	$\nabla^2$	Laplace operator
<b>K</b>	Permeability tensor	$\rho$	Fluid density
$L$	Porous sample's thickness in experiment	$\mu$	Fluid viscosity
$l_i$	$i = 1, 2, 3$ Lattice vectors	$\varepsilon$	Porosity
<b>n</b>	Unit vector normal to fluid-solid interface	<b>Subscripts</b>	
$p$	Pressure	$f$	Fluid phase
<b>r</b>	Position vector	$fs$	fluid-solid
<b>R</b>	Radius	$fe$	Fluid entrance-exit
$S_{fs}$	fluid-solid interface area on REV	<b>B</b>	Burette
$S_{fe}$	fluid entrance and exit area on REV	<b>P</b>	Porous
$t$	Time	<b>0</b>	Initial
<b>v</b>	Velocity		

## 3.2. Theory

### 3.2.1. Permeability Estimation using Closure Formulation of Volume Averaging Method

The formulation developed by Whitaker [1], based on the volume averaging method, is used in this theoretical model employed for estimating the porous-medium permeability. The flow variables in the pore region of an REV are averaged and the values are used in the macroscopic flow-field. Two types of averaging can be defined for an arbitrary flow variable  $\varphi$  as follow.

Phase Average:

$$\langle \varphi \rangle = \frac{1}{V} \int_{V_f} \varphi dV \quad (3.1)$$

Intrinsic Phase-Average (also known as Pore Average):

$$\langle \varphi \rangle^f = \frac{1}{V_f} \int_{V_f} \varphi dV \quad (3.2)$$

Here  $V$  represents the REV volume and  $V_f$  represents pore volume (or fluid volume in case of single-phase flow) within the REV of a porous medium. For low-Reynolds number flows, the boundary value problem for solving the velocity and pressure fields associated with the Stokes and continuity equations can be expressed as

$$0 = -\nabla p_f + \rho_f \mathbf{g} + \nabla^2 \mathbf{v}_f \quad (3.3)$$

$$\nabla \cdot \mathbf{v}_f = 0 \quad (3.4)$$

$$\text{B.C.1} \quad \mathbf{v}_f = 0 \quad \text{on} \quad S_{fs} \quad (3.5)$$

$$\text{B.C.2} \quad \mathbf{v}_f = f(\mathbf{r}, t) \quad \text{on} \quad S_{fe} \quad (3.6)$$

where  $S_{fs}$  represents the fluid-solid interface area while  $S_{fe}$  stands for the fluid entrance and exit areas in the REV. Using the volume averaging method [1], one can apply the volume averaging theorems to all terms of Eqns. (3.3) and (3.4) to obtain the macroscopic momentum balance equation in the form of Darcy's law. During this process of upscaling, the pressure and velocity terms are decomposed in terms of their intrinsic phase averages,  $\langle p_f \rangle^f$  and  $\langle \mathbf{v}_f \rangle^f$ , and corresponding perturbations,  $\tilde{p}_f$  and  $\tilde{\mathbf{v}}_f$ , as

$$p_f = \langle p_f \rangle^f + \tilde{p}_f \quad (3.7)$$

$$\mathbf{v}_f = \langle \mathbf{v}_f \rangle^f + \tilde{\mathbf{v}}_f \quad (3.8)$$

The use of Eqns. (3.7) and (3.8) during the volume averaging process results in the following equation set to solve for pressure and velocity perturbations:

$$0 = -\nabla \tilde{p}_f + \mu_f \nabla^2 \tilde{\mathbf{v}}_f - \frac{1}{V_f} \left\{ \int_{S_{fs}} \mathbf{n}_{fs} \cdot (-\mathbf{I} \tilde{p}_f + \mu_f \nabla \tilde{\mathbf{v}}_f) dS \right\} \quad (3.9a)$$

$$\nabla \cdot \tilde{\mathbf{v}}_f = 0 \quad (3.9b)$$

$$\text{B.C.1} \quad \tilde{\mathbf{v}}_f = -\langle \mathbf{v}_f \rangle^f \quad \text{on } S_{fs} \quad (3.9c)$$

$$\text{B.C.2} \quad \tilde{\mathbf{v}}_f = f(\mathbf{r}, t) \quad \text{on } S_{fe} \quad (3.9d)$$

Note that Eqns. (3.9a) and (3.9b) result from the momentum and continuity equations. In order to close the system of equations,  $\tilde{p}_f$  and  $\tilde{\mathbf{v}}_f$  are defined in terms of the corresponding averaged quantities as

$$\begin{aligned}\tilde{p}_f &= \mu_f \mathbf{b}_f \cdot \langle \mathbf{v}_f \rangle^f \\ \tilde{\mathbf{v}}_f &= \mathbf{B}_f \cdot \langle \mathbf{v}_f \rangle^f\end{aligned}\quad (3.10)$$

On substituting Eqn. (3.10) in Eqn. (3.9a) and (3.9b), the governing equations for the closure variables,  $\mathbf{b}_f$  and  $\mathbf{B}_f$ , can be developed as

$$0 = -\nabla \mathbf{b}_f + \mu_f \nabla^2 \mathbf{B}_f - \frac{1}{V_f} \left\{ \int_{S_{fs}} \mathbf{n}_{fs} \cdot (-\mathbf{I} \mathbf{b}_f + \nabla \mathbf{B}_f) dS \right\} \quad (3.11a)$$

$$\nabla \cdot \mathbf{B}_f = 0 \quad (3.11b)$$

The closure formulation allows the permeability tensor to be estimated in terms of the closure variables as

$$\frac{1}{V_f} \int_{S_{fs}} \mathbf{n}_{fs} \cdot (-\mathbf{I} \mathbf{b}_f + \nabla \mathbf{B}_f) dS = -\varepsilon_f \mathbf{K}^{-1} \quad (3.12)$$

Use of this definition in Eqn. (3.11a) results in

$$0 = -\nabla \mathbf{b}_f + \nabla^2 \mathbf{B}_f + \varepsilon_f \mathbf{K}^{-1} \quad (3.13)$$

At this point,  $\mathbf{b}_f$  and  $\mathbf{B}_f$  can be replaced by  $\mathbf{d}_f$  and  $\mathbf{D}_f$  [1] through the transformations

$$\begin{aligned}\mathbf{d}_f &= \varepsilon_f^{-1} \mathbf{b}_f \cdot \mathbf{K} \\ \mathbf{D}_f &= \varepsilon_f^{-1} \mathbf{B}_f^0 \cdot \mathbf{K} \\ \mathbf{B}_f^0 &= \mathbf{B}_f + \mathbf{I}\end{aligned}\quad (3.14)$$

On using the expressions given by Eqn. (3.14) in Eqn. (3.13) transforms the pore level ‘momentum’ equation as

$$0 = -\nabla \mathbf{d}_f + \nabla^2 \mathbf{D}_f + \mathbf{I} \quad (3.15)$$

and the pore level ‘continuity’ equation can be stated as

$$\nabla \cdot \mathbf{D}_f = 0 \quad (3.16)$$

Note that the closure formulation described by Eqns. (3.15) and (3.16) is similar to the Stokes boundary value problem that can be solved in an REV [1].

In Stokes flow, the pressure and velocity fields within the REV are controlled by boundary conditions Eqns. (3.5) and (3.6) at the fluid-solid interface and at the entrance and exit regions of REV. The first boundary condition on fluid-solid interface, Eqn. (3.9c), in terms of the closure variables can be expressed as

$$\text{B.C. 1} \quad \mathbf{D}_f = 0 \quad \text{on } S_{fs} \quad (3.17)$$

The second boundary condition given by Eqn. (3.9d) is problematic since it entails the use of an unknown function,  $f$ , to assign deviations at the entrance of the REV [1]. The problem was made tractable by considering a periodic unit cell instead of a full-fledged REV. The corresponding periodicity conditions for the velocity and pressure deviations can be described in terms of the closure variables as

$$\mathbf{D}_f(\mathbf{r} + l_i) = \mathbf{D}_f(\mathbf{r}) \quad (3.18a)$$

$$\mathbf{d}_f(\mathbf{r} + l_i) = \mathbf{d}_f(\mathbf{r}) \quad (3.18b)$$

These periodicity conditions state that the opposite sides of a square-shaped unit cell have the same values of the  $\mathbf{D}$  and  $\mathbf{d}$  components in the considered 2-D domain. Here  $\mathbf{r}$  represents the position vector of any point on the unit-cell boundary, while  $l_i$  are the lattice vectors with  $i \in$

{1, 2} that express the spatially periodic nature of the unit cell in the 2-D space. Enforcing the velocity deviations to add to zero within the REV results in the average-value condition of the form

$$\langle \mathbf{B}_f \rangle^f = 0 \quad (3.19)$$

This is consistent with definition of the spatial deviation as defined in the volume-averaging formulation [1]. On using this result with the definition of permeability tensor stated in Eqn. (3.12) and the definitions of the closure variables given in Eqn. (3.14), we can estimate the permeability tensor in much simpler form as

$$\mathbf{K} = \varepsilon_f \langle \mathbf{D}_f \rangle^f \quad (3.20)$$

The mapping variable  $\mathbf{D}_f$  is first estimated within the unit cell using the closure formulation given by Eqns. (3.15) to (3.19), then  $\mathbf{D}_f$  is integrated in the pore region of the unit-cell to obtain  $\mathbf{K}$  through Eqn. (3.20).

### 3.2.2. Experimental method for estimating permeability

The falling-head permeameter is employed to measure the permeability of porous medium using a liquid level at the inlet that is gradually decreasing with time due to the leakage of liquid through the sample. As shown schematically in Figure 21, the continuously decreasing head at the inlet implies that the inlet pressure driving the flow is decreasing. As a result, the Darcy velocity inside the porous sample is decreasing with time as well. If the initial height of water column in the burette is  $x_0$  at time  $t = 0$ , and the height at each subsequent time  $t$  is  $x$  during the experiment, then the permeability of the porous sample,  $K$ , can be estimated through the formula

$$\ln\left(\frac{x_0}{x}\right) = \frac{K\rho g R_p^2}{\mu L_p R_B^2} t \quad (3.21)$$

where  $L_p$  and  $R_p$  are the porous sample's length and radius, respectively;  $R_B$  is the radius of the burette;  $\rho$  and  $\mu$  are the liquid density and viscosity, respectively. If ordered pairs of  $(x, t)$  are recorded during the experiment and  $\ln\left(\frac{x_0}{x}\right)$  is plotted against time  $t$ , the permeability can be calculated from the slope of the plot.

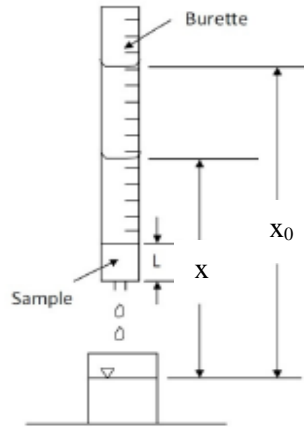


Figure 21. A Schematic of Falling-Head Permeameter

### 3.3. Results and discussion

#### 3.3.1 Initial validation of Closure Formulation Method

In order to evaluate the accuracy of our proposed simulation technique for estimating the permeability using COMSOL, results of a recent study by [93] on a similar determination of the permeability of an idealized porous medium were used. A simple square-shaped unit cell (with side of length  $l$ ) with two different square-shaped solid particles in the center (representing porosities of 0.5 and 0.75) was considered. Governing equations were solved within the



computational domain using the finite element method. The number of triangular mesh elements used for the cases of porosity 0.5 and porosity 0.75 were chosen as 130,048 and 186,880, respectively, after a detailed mesh independence study. The Direct (PARADISO) solver was used by COMSOL to solve the system of equations, and the residuals were limited to  $1e^{-6}$  or less.

The set of closure equations defined in Eqns. (3.15) and (3.16), subject to the boundary conditions Eqns. (3.17) and (3.18), were then solved within the void regions of the two unit cells. As shown in Table 3, there is a very good agreement between the dimensionless permeability values for the unit cells predicted in [93] and in the present study. This clearly establishes the accuracy of our method.

*Table 3. A comparison between the results of this study and those of Lasseux et al. in terms of dimensionless permeability  $K^*$  [93]*

$K^* (= K/l^2)$		
Porosity	Lasseux et al., 2011	Present work
0.5	0.002386	0.002301
0.75	0.013023	0.013022

### **3.3.2. Permeability of porous preform made from CNF**

#### **3.3.2.1. Numerical estimation of the 2D permeability tensor**

Most of the earlier efforts of using the closure formulation were confined to regular idealized 2D or 3D geometries that could be recreated by repeating a unit cell. Kim [78] considered a regular 2D porous medium made of a unit cell consisting of rectangular particles, while Quintard [94] studied a 3D periodic medium with rectangular objects within a unit cell. It was observed that

the 3D model was closer to the experiments as compared to the 2D effort. Some effort has been made to solve Whitaker's closure problem in 3D microstructures and estimate the permeability. Bernard [95] estimated the permeability of binary Al-Cu alloys using micro-CT images and found the permeability tensors for various cases. However, their process was required the use of rather expensive European Synchrotron Radiation Facility. Perhaps because of these reasons, such efforts find limited applications.

Here we will use the closure formulation in 2D to estimate the permeability of CNF sample. As seen in the SEM pictures of CNF (Figure 22), the random distribution of CNF solid phase indicates that the closure formulation cannot be solved in a unit cell due to the lack of periodicity in the CNF solid-phase distribution. However, Whitaker had discovered that the use of a unit cell is permissible for such purposes because the error arising through the use of the periodic boundary conditions is confined to the borders of the unit cell and is not significant [1]. Therefore, in order to solve the closure equations in our pore-level geometry, SEM micrographs of different cross-section of the CNF sample were taken. The SEM images were obtained on a LEO 1530 FESEM with a 3kV accelerating voltage using an in-lens detector and a working distance of 1.3 mm. The samples were gold coated for 30s at 45mA in a Denton Vacuum Desk V sputter coater. All image processing was done in ImageJ [29]. Then the cross-sections were selected in the vertical and horizontal planes, and one of the micrographs (Figure 22) was selected for the purpose of solving the closure-formulation equations.

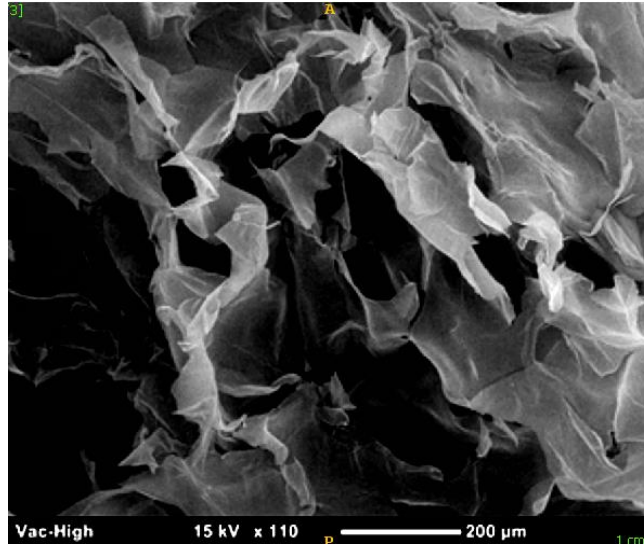


*Figure 22. SEM micrograph of a representative sectioned plane from the CNF sample*

In the present chapter, a 2D micrograph selected from inside of the CNF sample is used as a porous-medium geometry to solve COMSOL in. In order to use the geometry for computations, we assumed that brighter color fibers were closer to the top surface of micrograph while darker ones belong to the lower levels. Then if a cross flow were to occur, the brighter (lighter) color surfaces will act as obstacles (particles) while the darker surfaces can be treated as pores. Based on this assumption, we used ITK-SNAP<sup>®</sup> software to change the thresholding level for the 2D SEM micrograph in order to segment pore and solid parts. As a result, by changing the threshold level, three different geometries were extracted from the CNF micrograph with three different porosities. Subsequently, the SEM micrograph of the CNF sample could be converted into a ‘binary’ picture for use with COMSOL for further analysis. The 2-D geometry extracted from the CNF micrograph is shown in Figure 23 for all the three porosities.

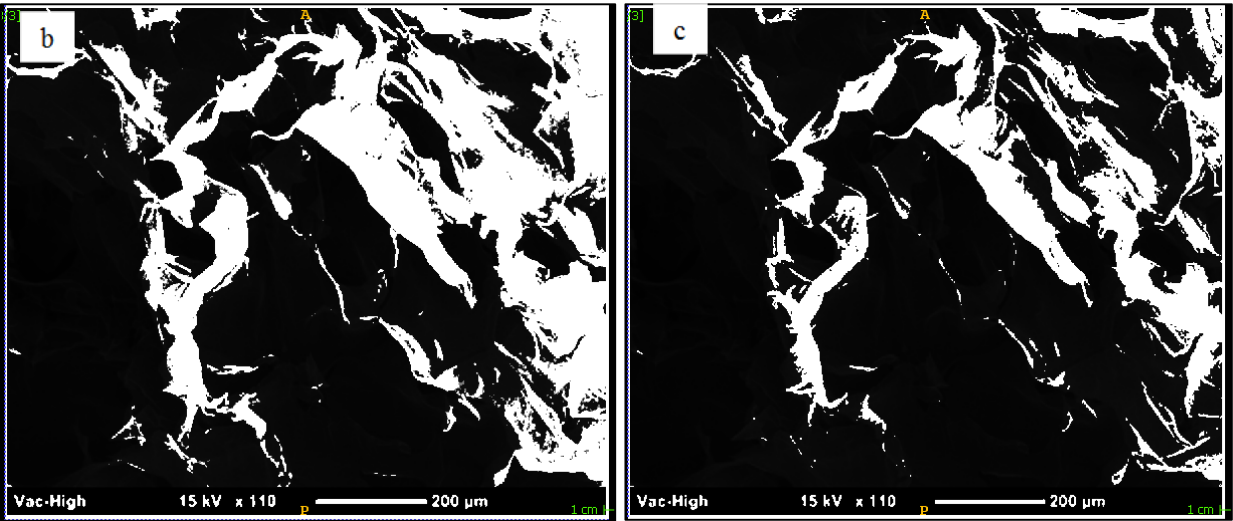
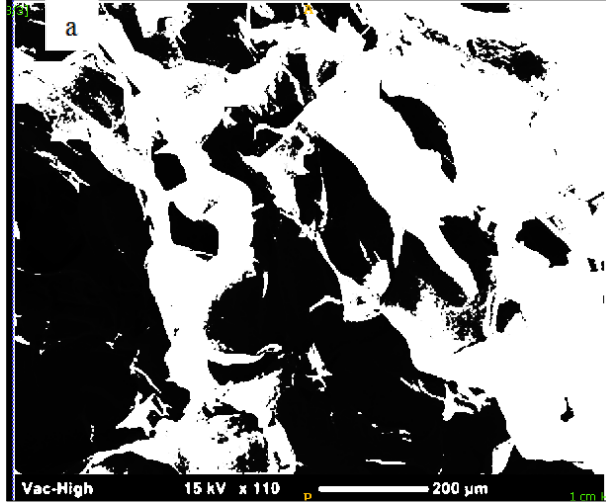


Figure 23. The solid (white) and pore (black) regions of a reconstructed 2-D 'binary' region extracted from the SEM micrograph Figure 22 for various porosities: a) threshold 1 with  $\varepsilon=0.53$ , b) threshold 2 with  $\varepsilon=0.7$  and c) threshold 3 with  $\varepsilon=0.84$

Note that for 2-D samples considered in the present study, the permeability tensor can be obtained through Eqn. (3.20) as

$$\mathbf{K} = \varepsilon_f \begin{bmatrix} \langle D_{11} \rangle^f & \langle D_{12} \rangle^f \\ \langle D_{21} \rangle^f & \langle D_{22} \rangle^f \end{bmatrix} \quad (3.22)$$

where each of the bracketed  $\langle D_{ij} \rangle^f$  terms represents the intrinsic phase-average value of  $D_{ij}$  (an element of the mapping tensor  $\mathbf{D}_f$ ) obtained after integrating it in the entire void region of the reconstructed binary micrograph. Here  $\varepsilon_f$  represents the porosity that is obtained by dividing the total void area with the total area of the micrograph. Different elements of the permeability tensor, Eqn. (3.22), were estimated with COMSOL after the governing equations, Eqns. (3.15) to (3.19), were solved within the void region of the domain. After all these calculations, the final form of the permeability tensor, as obtained for the three different thresholds, is given in Table 4.

*Table 4. Permeability of CNF as obtained from the closure-formulation based numerical simulations for three different thresholds.*

<b>CNF Samples</b>	<b>Porosity</b>	<b>Permeability tensor <math>\mathbf{K}</math> (<math>10^{-10} \text{ m}^2</math>)</b>
Threshold 1	0.53	$\mathbf{K} = \begin{bmatrix} 0.32 \pm 0.09 & 0.02 \pm 0.01 \\ 0.01 \pm 0.01 & 0.91 \pm 0.15 \end{bmatrix}$
Threshold 2	0.7	$\mathbf{K} = \begin{bmatrix} 0.6 \pm 0.12 & 0.03 \pm 0.02 \\ 0.02 \pm 0.01 & 1.31 \pm 0.23 \end{bmatrix}$
Threshold 3	0.84	$\mathbf{K} = \begin{bmatrix} 0.87 \pm 0.17 & 0.09 \pm 0.05 \\ 0.13 \pm 0.01 & 1.9 \pm 0.34 \end{bmatrix}$

The same order-of-magnitude of the diagonal terms in the three permeability tensors indicate that our CNF sample can be characterized as being somewhat isotropic. It is also interesting to note that the non-zero diagonal terms are small and are on the order of 10% of the main diagonal terms. This clearly indicates that the x (horizontal) and y (vertical) coordinates considered in Figure 23 are not the principal or material directions of the porous medium. (If the x and y directions match the principal directions, the permeability-tensor matrix acquires a pure

diagonal form). But the smallness of the non-diagonal terms does point out that the considered x (horizontal) and y (vertical) directions in Figure 23 are quite close to the principal or material directions of the CNF.

It is generally agreed that the permeability tensors are symmetric and hence their non-diagonal terms should be equal. We do notice that the non-diagonal terms of  $\mathbf{K}$  are almost equal, though the difference is larger for threshold 3<sup>3</sup>. This little lack of symmetry is attributed to the errors resulting from the fact that the unit cell constructed from a real porous medium is non-periodic in nature, while the unit cell used to derive the closure formulation is periodic [1].

### 3.3.2.2. Mesh independence study

In order to evaluate the influence of mesh on the closure computations inside pore space, a mesh independence study was done to ensure that the 2D permeability tensor was accurately estimated. Since the finite element method is used in COMSOL, unstructured triangular elements were used to create the mesh inside the pore region. In our simulation for instance, we applied three different mesh-sizes for threshold 3: (1) normal mesh with 39143 elements, (2) fine mesh with 50877 elements, (3) extra-fine mesh with 76131 elements. The three meshes for threshold 3 are shown in Figure 24. Note that the meshes are refined near the solid-fluid interface to resolve sharper gradients present near solid surfaces due to Eqn. (3.17), arising from the no-slip condition present in the original closure formulation based on Stokes equation [1]. We then solved the closure equations using the three meshes.

A comparison of the  $K_{11}$  element of the CNF permeability tensor for all three thresholds is shown in Figure 25. As seen in Figure 25,  $K_{11}$  values are quite equal despite the increase in the

---

<sup>3</sup> Note that thresholds 1 and 2 generate more realistic pore spaces since the resultant porosities are closer to the experimentally measured porosity for CNF. In this respect, the threshold 3 is of rather academic nature.

number of elements, thus confirming the mesh independence of our results. For the rest of our numerical simulations, we used the fine mesh.

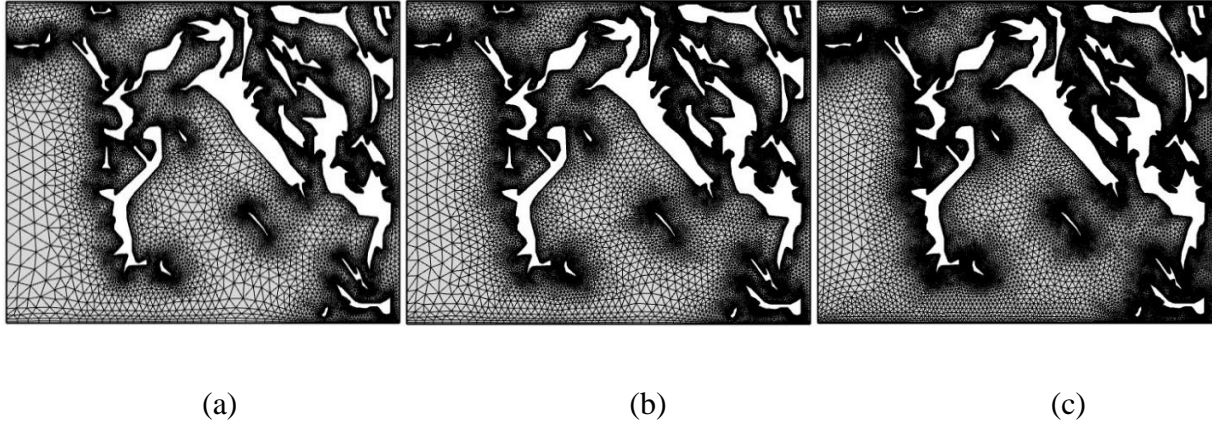


Figure 24. Distribution of triangular elements in a) normal, b) fine and c) extra-fine meshes used in the 2D pore space obtained with threshold 3.

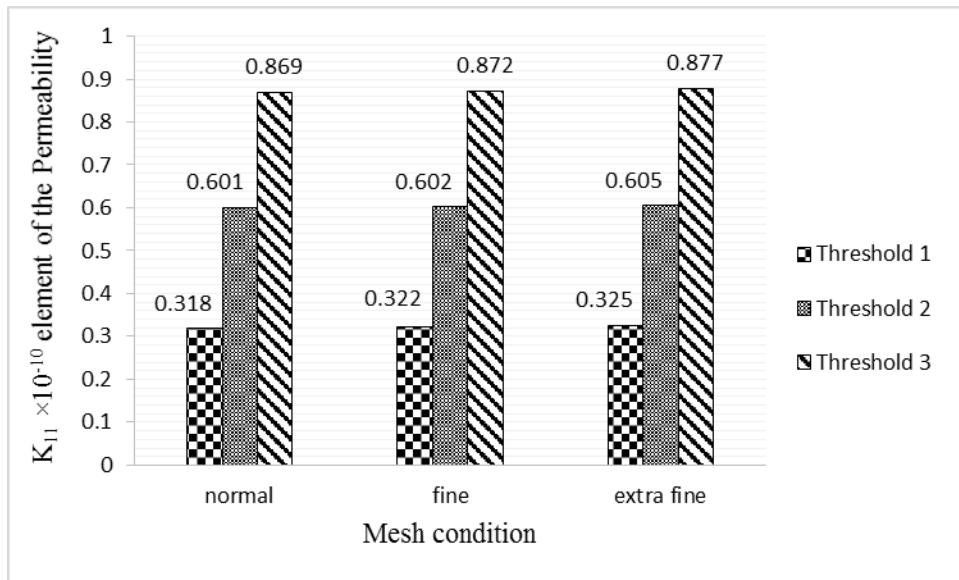


Figure 25. The nine different  $K_{11}$  values resulting from the mesh independence study involving the CNF permeability tensor (Eqn. (3.22)). The values correspond to three different meshes and three different pore-space geometries resulting from the application of the three different thresholds.

### 3.3.3. Experimental CNF permeability

After measuring the CNF permeability using the closure formulation, the falling-head permeameter was used to estimate the permeability of the CNF sample. In these experiments, the height of the liquids was measured as a function of time and the permeability was calculated using Eqn. (3.21) by fitting a linear curve on the data points (Section 3.2.2). Experiments were done using Decane. (This alkane, unlike water, was used since the cellulose does not dissolve in it.) Some of the physical properties of the working fluid and CNF sample are presented in Table 5.

*Table 5: Physical properties of the CNF and the working fluid.*

Decane Viscosity (Pa.sec)	0.000859
Decane Density (kg/m <sup>3</sup> )	730
CNF sample radius (m)	0.004
Syringe radius (m)	0.013
CNF sample length (m)	0.03

The  $\ln(\frac{x_0}{x})$  vs  $t$  plots for these two different working fluids are presented in Figure 26. The slope of the linear part of the diagram is used in the estimation of the permeability. The permeability obtained from the experiments is compared with the numerical estimation in Table 6.



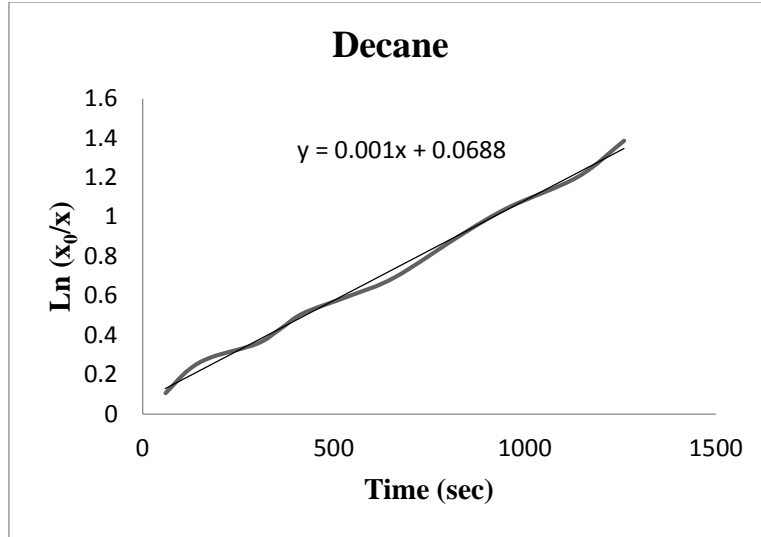


Figure 26. Relationship between the ratio of CNF liquid-column heights and time for (a) Decane (b) Hexane.

Table 6: Comparison of the permeability values obtained from the closure-formulation based numerical simulation and the falling-head permeameter experiments. Units are in  $m^2$ . The scatter is estimated as the 95% confidence interval obtained from three different experiments.

Numerical simulation	Experiments
$\mathbf{K} = \begin{bmatrix} 0.32 & 0.02 \\ 0.01 & 0.91 \end{bmatrix} \times 10^{-10}$	$\mathbf{K} = (0.38 \pm 0.04) \times 10^{-10}$

As shown in Table 6, there is a good agreement between the permeability values obtained from the experiments with Decane as the working fluid on the one hand, and the values of the diagonal elements of the permeability tensor as obtained from the closure formulation on the other. This confirms the accuracy of the proposed simulations.

### 3.4. Discussion

Though the 2-D simulation is not representative of the full 3-D flow happening in the porous media, it can generate, as we saw above, quite accurate results. In this respect, the proposed methodology is quite similar to the analytical models for permeability proposed in the literature: such models (for example, the model by Gebart [96] or the model by Bruschke and Advani [97] for permeability of fibrous porous media) are based on solving easier 2-D Stokes flow in simplified 3-D geometries such as the constant-diameter cylinders arranged in the regular square or hexagonal spatial lattice. Though such models often do not mirror the experimentally-observed random fiber arrangements and the complex 3D flow patterns or do not exactly match the experimentally-measured permeabilities, they are still useful as they give one an order-of-magnitude estimate of this crucial property. We request the reader to treat our method in this same vein.

Despite introducing an improvement in the permeability estimation process for realistic, irregular porous materials, the proposed 2D micrograph based method cannot perfectly represent the 3D pore structure (and thus cannot recreate the complex 3D flow patterns) of the considered porous media. Even though the permeability values obtained from the 2D simulation were close to the experimental observations, it would be more accurate to perform a full 3D analysis using a micro-CT scanner. But such a simulation will be computationally challenging due to (a) higher degrees-of-freedom involved ( $\sim N^3$  in 3D compared to  $\sim N^2$  in 2D), (b) the resulting higher memory and storage requirements because the size of the micro CT images and corresponding mesh files would be thousand times greater compare to 2D SEM geometries. (For example, it took 10 hours to solve the 3D closure problem in a micro-CT scanned pore geometry discretized into 2.4 million elements [95]. While for a typical CNF case, the 2-D pore geometry is discretized into a maximum of 75,000 elements and it took us at the most an hour to solve the closure problem.) It is also to be

remembered that the per-hour costs of still-rare 3D micro-CT scanners are quite high compared to the costs of now-standard 2D SEM scanners. Because of these drawbacks, the full 3D closure-formulation based permeability estimation remains slow and challenging—the corresponding 2D estimation of permeability, which is fast and inexpensive, has the potential to emerge as a powerful tool in the arsenal of porous-media scientists and researchers.

### **3.5. Summary and Conclusions**

In this study, the closure formulation employed by Whitaker [1] to derive Darcy's law using the volume averaging method was used in 2-D to estimate the permeability tensor for porous media found in CNF samples. The main advantage of the proposed closure-formulation method is its direct estimation of the permeability tensor through a single closure-formulation simulation. The SEM micrographs of the CNF sample was used to create 2D binary pictures representing the solid and pore phases. The permeability tensor was estimated by solving the partial differential equations associated with the closure formulation within the pore space of a unit cell. From the closeness of the  $K_{11}$  and  $K_{22}$  terms in the 2-D permeability tensor, the considered porous material was found to be almost isotropic. The presence of small non-diagonal terms indicated that the chosen x and y axis in the micrographs almost match the principal or material directions. The accuracy of the numerical results was established through the convergence of permeability in a mesh convergence study. The numerical permeability thus estimated was compared with the experimental permeability obtained using the falling-head permeameter. A good agreement between the two demonstrated the accuracy of the closure formulation and the resulting simulation. These results also present the closure formulation based method as a viable method to estimate the permeability of porous media using 2D SEM micrographs; such a method harnesses the micro-macro coupling and is marked with absence of any constitutive-relation based assumption for such

upscaling. Such a method is also faster, less expensive and less problematic than the corresponding 3D micro-CT scan based method because of much smaller degrees-of-freedom, and much smaller memory and storage requirements.

## **CHAPTER 4: An Analytical Study of the Absorption Characteristics of Cellulose Nano-Fiber**

### **4.1. Introduction**

The flow of liquids and gases through porous media consisting of non-absorbing, rigid particles or fibers has been studied extensively in the literature [89, 98]. However, the flow of liquids through porous media consisting of liquid-absorbing, swelling particles or fibers is a rather less-studied topic. In recent years, several studies have been conducted involving liquid absorption and swelling (of solid phase) in various types of porous media. Chatterjee and Gupta studied the wicking of water in napkins and wipes that swell during the wicking process [99]. Zhu et. al. applied the hybrid mixture theory and develop a novel flow model for clay-based porous media [100]. Weinstein and Bennethum used the hybrid mixture theory to obtain the transport equation in terms of liquid volume fraction for swelling porous media, including those made from clay and biopolymers [101].

Cellulose nanofibers (CNFs), a new type of nanofibers made purely of cellulose molecules, have very good mechanical property at the nanoscale compared to other natural fibers [7, 9, 13]. In the last decade, the interest in cellulose nanofibers has been rekindled due to some recent technological breakthroughs in their manufacturing that has led a significant reduction in their prices.

CNFs aerogels are an extreme light-weight and porous materials that are made by removing liquid solvent from a gel, as a result of which a solid skeleton is created with large spaces between the solid phases [102]. Formation of CNF aerogels is usually accomplished through common processes including freeze-drying and vacuum-drying. High compatibility with drying processes

and high crosslinking ability make cellulose a good candidate to be used as a reinforcement in making composites [52, 103-106]. Recently attempt has been made to explore the usefulness of CNF as a potential reinforcement material for making polymeric CNF nanocomposite using LCM has been explored [57].

Pillai [74] rigorously derived the governing equations for the single-phase flows encountered in liquid-absorbing swelling porous media, applications of which included the use of natural-fiber preforms in LCM. Using the volume averaging method developed by Whitaker [1], novel forms of the mass balance (continuity) equation were developed to incorporate the liquid-absorbing and swelling nature of the solid phase. In this development, a new parameter called the *absorption coefficient*,  $b$ , was proposed to quantify the relative strengths of rate of liquid volume loss due to absorption and rate of solid-phase volume increase due to swelling. (See the appendix for a derivation of the continuity equation.) The developed set of equations with the assumption  $b = 1$  performed well for predicting the inlet pressure and front location as a function of time during the constant flow-rate, 1-D flow injection of diluted corn-syrup in an RTM mold packed with natural fibers [107, 108]. The same equation set with identical assumption of  $b$  being unity works very well during the 1-D wicking of liquids into a swelling, paper-like substrate with superabsorbent fibers [109, 110].

In these previous studies, the assumption  $b = 1$  was something discovered accidentally during the curve-fitting exercise. However, in the present study, the absorption coefficient,  $b$ , of CNF is to be measured directly by a novel method involving dipping pieces of CNF sheets in water and by measuring the net force experienced using a microbalance. As we shall see, the measured value of  $b$  fell very close to the previously assumed value of  $b$ .

<b>Nomenclature</b>	
<p><math>A</math> Area</p> <p><math>b</math> Absorption coefficient</p> <p><math>b'</math> Non-dimensional term in absorption coefficient measurement</p> <p><math>\mathbf{g}</math> Acceleration due to gravity</p> <p><math>\mathbf{n}</math> Unit vector normal to fluid-solid interface</p> <p><math>\mathbf{q}</math> Arbitrary vector quantity</p> <p><math>S</math> Sink term</p> <p><math>t</math> Time</p> <p><math>T</math> Tension force</p> <p><math>\mathbf{v}</math> Velocity</p> <p><math>V</math> Volume</p>	<p><math>W</math> Weight</p> <p><b>Greek Symbols</b></p> <p><math>\nabla</math> Gradient vector</p> <p><math>\partial</math> derivative</p> <p><math>\varepsilon</math> Porosity</p> <p><math>\rho</math> Fluid density</p> <p><b>Subscripts</b></p> <p><math>f</math> Fluid phase</p> <p><math>fs</math> fluid-solid</p> <p><math>s</math> Solid</p> <p><math>0</math> Initial</p>

#### 4.2. Further details on modeling LCM-type flows in swelling, liquid absorbing porous media

The two main governing equations proposed by Pillai [74] for modeling the saturated flow in swelling, liquid-absorbing media were the classical forms of the continuity equation and Darcy's law:

$$\begin{aligned} \nabla \cdot \langle \vec{v}_f \rangle &= 0 \\ \langle \vec{v}_f \rangle &= -\frac{\mathbf{K}}{\mu_f} \cdot \left[ \nabla \langle p_f \rangle^f - \rho_f \vec{g} \right] \end{aligned} \quad (4.1)$$

The former was obtained after assuming the volumetric rate of liquid absorption to be equal to the volumetric change in the solid phase [i.e., after taking the absorption coefficient  $b = 1$  in Eqn. (A10) of the Appendix]. As mentioned earlier, the previous numerical and analytical predictions by Masoodi et al. [107, 109, 110] confirm that the assumption of  $b$  equal to unity

yields a very good fit with experimental results for the swelling, natural-fiber based porous media. In this section, we are going to list a few examples involving the saturated flow of liquids in such media where we will see that the final governing equations developed in Eqn. (4.1) was successfully employed to explain the experimental observations.

First the case of wicking of water through a strip of composite paper made from cellulose and superabsorbent polymer is considered [110]. Since the strip was rectangular (of similar dimensions as the CNF sheets used in the current study), a 1D saturated flow is created during the imbibition of water from one side of the rectangle under the influence of the capillary suction pressure. The analytical expression for the length of the liquid front,  $L_{lf}$ , as a function of time,  $t$ , was derived from Eqn. (4.1) to be

$$L_{lf} = \sqrt{\frac{2P_c}{\varepsilon_{fo}\mu} e^{(b-1)(\frac{\varepsilon_f}{\varepsilon_{fo}})} \int_0^t e^{(b-1)(\frac{\varepsilon_f}{\varepsilon_{fo}})} K(t') dt'} \quad (4.2)$$

such that  $P_c$  is the capillary suction pressure,  $\varepsilon_{fo}$  is the porosity of the dry medium,  $\mu$  is the liquid viscosity, while  $K$  is the permeability of the medium. Note that the permeability changes as a function of space and time in the wetted portion of the medium (due to swelling of the solid phase and subsequent reduction in porosity), however after ignoring its spatial variation, the permeability is assumed to be a function of time only. A comparison of the length of liquid front for different values of  $b$  in Eqn. (4.2) with the experimental results reported by Schuchardt and Berg [110] is given in Figure 27. Note that the results for  $b=0$  is a bit off, however by increasing the value of  $b$  to unity, the results show better fit with experimental data.



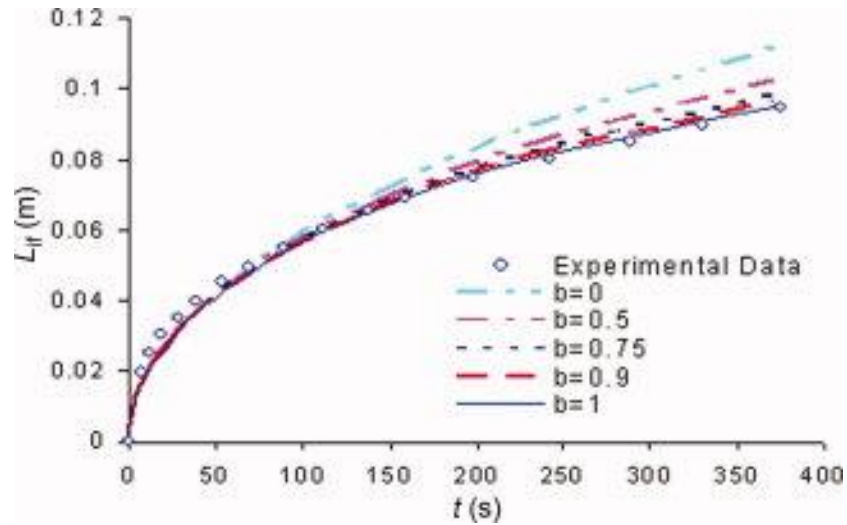


Figure 27. Effect of changing the value of the absorption coefficient,  $b$ , from 0 to 1 on the predicted length of the liquid front,  $L_{lf}$ , [110] as a function of time

After evaluating the efficacy of the equations given in Eqn. (4.1) for modeling the wicking in a natural-fiber medium, let us now consider these equations in modeling the pressurized flow of a liquid through a liquid-absorbing, swelling fabric made of natural fibers. As before, the equations given in Eqn. (4.1) were used for the flow-front prediction numerically, and an estimate of the local variation in the permeability was needed. Two such variations were considered. One variation, to be called the *estimated*  $K$ , was based on a microscopic study of the increase in fiber diameter with time and then using the Kozeny–Carman relation for predicting changes in the permeability with time. The other variation named the *measured*  $K$ , was based on the actual measurement of the permeability of a thin strip of jute fabric. As shown in Figure 28, the numerical simulation of mold filling during the constant inlet-pressure injection using the *measured*  $K$  model was more accurate compared with the one using the *estimated*  $K$  model. However, both these simulations were much better than the *constant*  $K$  simulation, which assumed no swelling effect for the jute fabric. To test the accuracy of the proposed model further, its effect was also studied

on the inlet pressure, another important flow variable in these injection experiments. As shown in Figure 29, during a constant flow-rate injection experiment, the *measured K* model was much more accurate than the *estimated K* and the *constant K* models. More details on these studies can be found in Masoodi et al. [107].

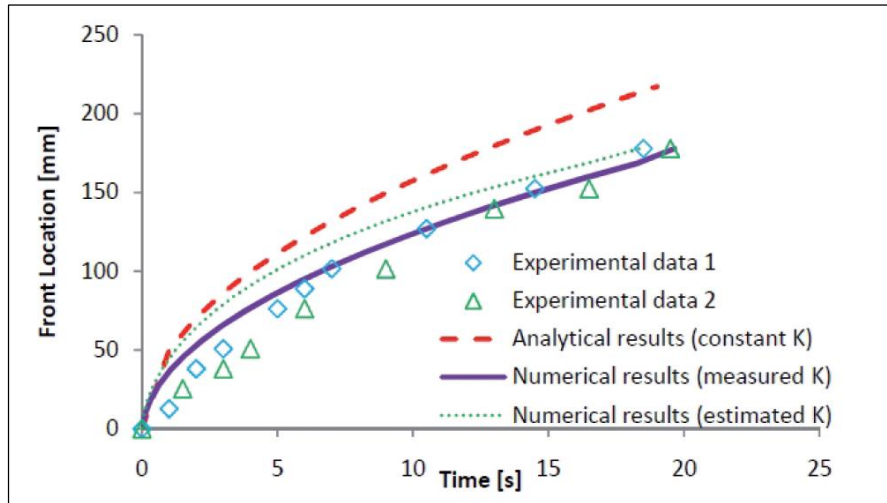
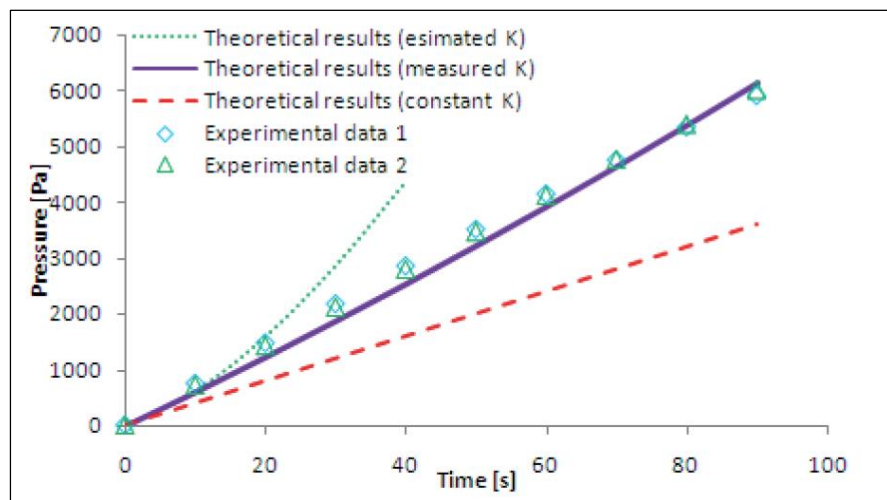


Figure 28. Comparison of the evolution of the flow-front location during a 1D flow experiment involving the flow of a swelling-inducing liquid through a bed of natural fibers for the constant inlet pressure of 12 kPa [107].



*Figure 29. Comparison of the evolution of the inlet pressure during a 1-D flow experiment involving the flow of a swelling-inducing liquid through a bed of natural fibers for the constant flow-rate of 3 ml/s [107].*

Both these studies clearly establish that assuming of the absorption coefficient,  $b$ , to be unity yields good predictions. In the following section, we are going to describe an experimental analysis for actually measuring  $b$  (so that we can find out how close is the measured value to this curve-fitted value).

### **4.3. Theory behind experimental estimation of the absorption coefficient $b$**

In the continuity equation derived for swelling porous media (Eqn. A10), the absorption coefficient,  $b$ , plays an important role in the modified continuity equation. However, this important flow quantity has never been measured directly. In this section, an attempt will be made to directly estimate  $b$  for the CNF preform using the microbalance available in a tensiometer, which is also called the Dynamic Contact-Angle Analyzer (DCA). In order to measure the absorption coefficient, a small piece of CNF preform will be hung from a hook attached to the microbalance (Figure 30). The microbalance reads the net down-wards force acting on the hung specimen. Hence the initial reading in the microbalance will be the weight of the dry CNF preform piece. After immersing the piece in a liquid (where the preform swells after absorbing liquid), the microbalance reading will change due to the buoyancy force acting on the preform. Using the following theory, the microbalance reading before and after the immersion can be used to estimate the absorption coefficient  $b$ . After this estimation, we can then use the exact value of  $b$  in Eqn. (A10) of the appendix to find the final form of the modified continuity equation for swelling CNF porous medium.

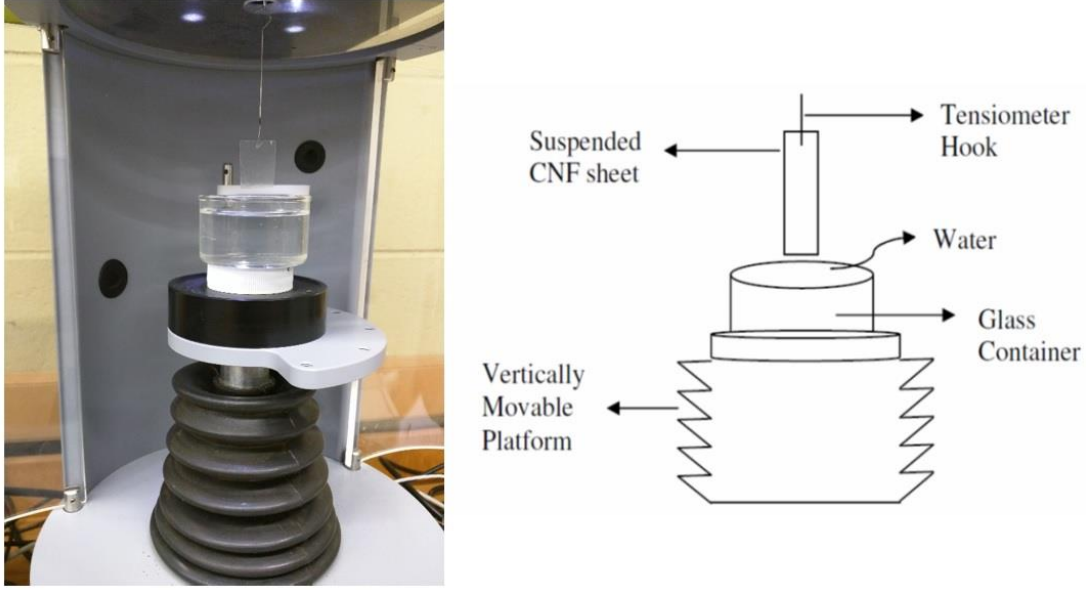


Figure 30. a) Microbalance of DCA tensiometer used for measuring the absorption coefficient, b)

*Schematic of the setup showing the details*

Assuming the dynamic effects to be negligible, we will enforce force balance on the completely-submerged CNF sample suspended from the hook. The general force-balance equation, where the terms representing various forces are a function of time, could be obtained as

$$T(t) + \rho g V(t) = W(t) \quad (4.3)$$

where  $T(t)$  is the tension reading measure by the microbalance,  $\rho g V(t)$  is the buoyancy force experienced by the sample and  $W(t)$  is the CNF sample weight. (Here we are neglecting any surface tension based downward force that will be acting on the wire suspending the CNF specimen from the hook.)  $W(t)$  was obtained by taking the sample out from water after time  $t$ , blowing air into it to shake-off the water sticking to the sample surface, and then using the electronic microbalance. The change in the volume of the CNF specimens,  $(V(t) - V_0)$ , could be obtained through Eqn. (4.3); note that  $V_0$  is the initial volume of dry CNF paper sheet and is

obtained through Eqn. (4.3) at  $t = 0$  while we measure  $T(t)$  and  $W(t)$  for the dry sample at the beginning of the experiment. The volume of water absorbed by CNF specimen as a function of time,  $V_w(t)$ , could be obtained by using the change in the weight of the specimen before and after the dipping process:

$$V_w(t) = \frac{W(t) - W_0}{\rho g} \quad (4.4)$$

Using Eqn. (A9) in the appendix, the absorption coefficient could be expressed as

$$b = \frac{S}{d\varepsilon_s/dt} \quad (4.5)$$

Now the time derivative of the fiber volume fraction,  $\varepsilon_s$ , could be defined using its definition within an REV,  $V$ , and REV volume,  $V_{REV}$ , as

$$d\varepsilon_s/dt = \frac{1}{V_{REV}} \frac{dV}{dt} \quad (4.6)$$

The definition of the sink term,  $S$ , as the rate of depletion of liquid within an REV allows us to express it as

$$S = \frac{1}{V_{REV}} \frac{dV_w}{dt} \quad (4.7)$$

where  $dV_w$  is the differential reduction in the surrounding liquid volume due to absorption. On substituting Eqns. (4.6) and (4.7) in Eqn. (4.5), the absorption coefficient,  $b$ , could be obtained as the ratio of the volume of liquid absorbed to the change in the fiber volume in a given differential time-interval:

$$b = \frac{dV_w}{dV} \quad (4.8)$$

The coefficient  $b$  as defined above is rather difficult to measure experimentally. Instead, we found it convenient to measure a quantity  $b'$  that is defined as

$$b' = \frac{V_w(t)}{V(t) - V_0} \quad (4.9)$$

which is the ratio of total volume of water absorbed by the CNF sample by a given time to change in the sample volume due to swelling during the same time. It turns out that, by taking the derivative of Eqn. (4.9) with respect to  $V(t)$  and using Eqns. (4.8) and (4.9), one can relate  $b$  to  $b'$  through the relation

$$b = (V(t) - V_0) \frac{db'}{dV} + b' \quad (4.10)$$

#### 4.4. Experimental procedure and data analysis

Rectangular, CNF samples were cut from CNF sheets of thickness 0.12 mm and diameter 10 cm. We decided to use water for our experiments since CNF readily absorbs water, a polar liquid, and swells. The DCA tensiometer was calibrated and adapted suitably to measure tension force on the order of sample weight as a function of time during experiment. A total of 9 cut CNF samples of varying sizes were used in our experiments. Each sample was subjected to a cyclical dipping process of 30 seconds time-period for 20 minutes. At the end of this period, it was observed that all CNF samples had reached their maximum-possible saturation states such that they were no longer absorbing any more water. Physical properties and average initial values for each of the CNF samples are shown in Table 7.

Table 7. Physical properties and average initial values for each CNF sample used in the dipping experiment

Samples No.	Sample dimension (mm <sup>2</sup> )	Initial thickness (mm)	Initial Vol. (V <sub>0</sub> ) (E-08 m <sup>3</sup> )	Initial weight (W <sub>0</sub> ) (gr)
1	8×10	0.12	0.96	0.0144
2	10×10	0.12	1.2	0.0174
3	10×13	0.12	1.6	0.0213
4	10×15	0.12	1.8	0.0247
5	15×15	0.12	2.7	0.0363
6	15×18	0.12	3.2	0.0433
7	15×20	0.12	3.6	0.0483
8	17×20	0.12	4.1	0.0563
9	20×20	0.12	4.8	0.065

By measuring tension in the string and weight of sample during the experiment as a function of time and by using Eqn. (4.3) and (4.4), the change in the volume of the CNF sample, ( $V(t) - V_0$ ), and the volume of water absorbed by the sample,  $V_w(t)$ , were evaluated. Using these two values,  $b'$  was estimated through Eqn. (4.9). In order to estimate the value of  $b$  through Eqn. (A10), the derivative of  $b'$  with respect to  $V(t)$  was needed. Therefore, through the plot of  $b'$  against  $V(t) - V_0$  (shown in Figure 31), the slope of the diagram ( $\frac{db'}{dV}$ ) was obtained after fitting a straight line passing through the scattered points. This slope was then used in Eqn. (A10) to measure the final value of the absorption coefficient  $b$ .

Table 8. Final values for the tension in the string, the weight and the absorbed liquid volume for CNF samples

Samples No.	Sample Dimension (mm <sup>2</sup> )	Tension (mN)	Final Vol. (V) (E-07 m <sup>3</sup> )	Final weight (W) (gr)	Vol. of absorbed water, V <sub>w</sub> (E-07 m <sup>3</sup> )
1	8×10	0.023	0.74	0.0144	0.62
2	10×10	0.029	0.89	0.0174	0.74
3	10×13	0.034	1.1	0.0213	0.96
4	10×15	0.035	1.2	0.0247	1
5	15×15	0.054	1.8	0.0363	1.5
6	15×18	0.065	2.3	0.0433	1.9
7	15×20	0.072	2.5	0.0483	2
8	17×20	0.085	2.9	0.0563	2.5
9	20×20	0.110	3.4	0.065	2.9

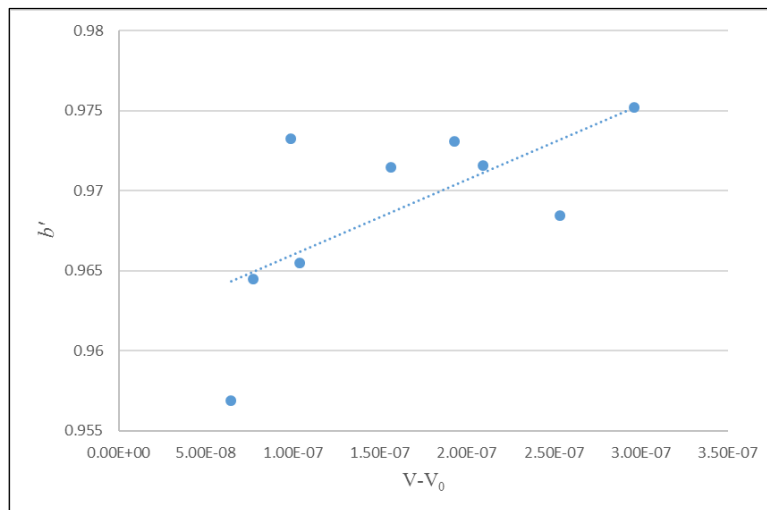


Figure 31. The plot of  $b'$  against  $V(t) - V_0$



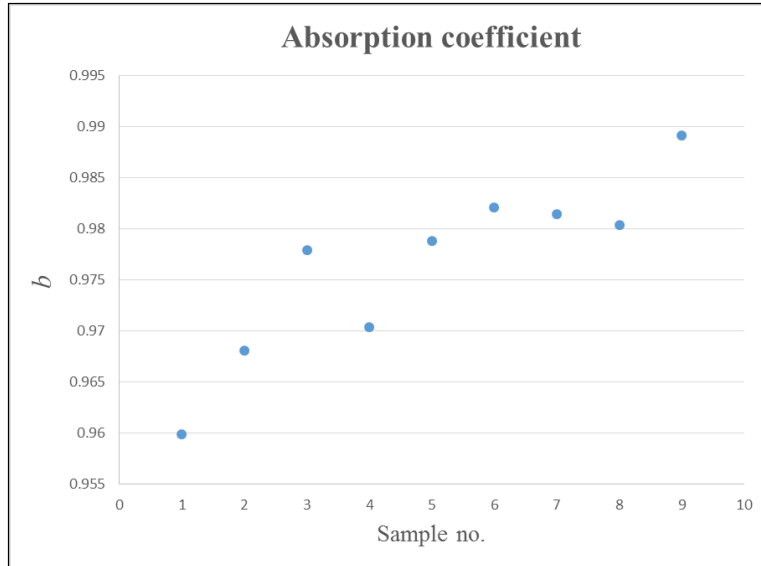


Figure 32. A scatter in the value of the experimentally measured absorption coefficient,  $b$ , estimated for CNF

The average final values for the tension, weight and absorbed volume are shown in Table 8 for all the CNF samples. Using these results, the absorption coefficient  $b$  was estimated and its values are now presented in Figure 32 for all the nine CNF samples. As we can see, the absorption coefficient values for our CNF samples were found to be quite close to unity. This close convergence clearly indicates that the differential liquid volume absorbed by samples and the corresponding differential changes in sample volumes, as indicated by Eqn. (4.8), are clearly equal. In other words, *the changes in the volumes of CNF samples during swelling are entirely due to the volume of water absorbed by it.*

In this study, the  $b$  estimation was done for a free, unconstrained CNF sample. However, during LCM mold filling, the swelling occurs in a preform that is constrained, i.e., the solid phase is constrained from free expansion by both the neighboring solid and liquid phases. However, during the initial phases, the expansion can be thought of as being unconstrained. This implies that

the assumption of using  $b$  as unity for flow models in swelling, liquid absorbing porous media is justifiable, at least during the initial stages.

#### **4.5. Summery and conclusion**

A unique form of the mass balance (continuity) equation, developed as a result of applying the volume averaging method to the single-phase flow of Newtonian fluids in swelling, liquid-absorbing CNF, is the focus of this study. This equation includes sink (due to the absorption of liquid by the solid phase) and source (due to the swelling of the solid phase) terms and is simplified further by defining a new absorption coefficient  $b$ . The case of the absorption coefficient  $b$  being unity, which corresponds to the liquid absorption rate into fibers being equal to the fiber expansion rate, results in the classical form of the continuity equation that is originally derived for rigid, non-deforming porous media.

A novel method of measuring  $b$  directly by dipping of the solid phase into the liquid, while tracking the tension needed to keep the phase stationary, is proposed in this paper. The balance of forces for the hydrostatic case results in a simple formula (Eqn. 4.10) for estimating  $b$ . The assumption of using  $b$  as being unity for flow models involving liquid-absorbing, swelling porous media is found to be correct for CNF preforms used in LCM. This gives one added confidence in the use of the flow model summarized by Eqn. (4.1) which has been found to work well [107-110] for natural-fiber based porous media.

Though the use of  $b = 1$  leads to a form of the continuity equation (Eqn. 1) that is quite ‘regular’ and has been used in the past in LCM flow simulations, this particular form was achieved using the basic assumption that the volume of liquid going into the solid phase is equal to the volume by which the solid phase swells. (That is by balancing the ‘sink’ of liquid absorption into the solid phase with the ‘source’ of solid phase swelling.) This implies that the resin used during

the LCM process will be absorbed by the CNF or natural-fiber based solid phase, and if it is a curing, heat-releasing resin, the fibers will as a result act as a source of heat during the mold-filling process. This has serious consequences as far as the governing equations for LCM mold-filling are concerned—we can expect to find several source and sink terms in the temperature and cure equations. Important future work needs to be done to establish such an equation set rigorously.

#### 4.6. Appendix

Here we will present a detailed derivation of the modified mass balance or the continuity equation (first equation of Eqn. 4.1) using the volume averaging method in order to present the assumptions that went into the derivation of the seemingly innocuous and utterly conventional continuity equation.

In our analysis concerning saturated flow in a porous medium, we assume to have only two phases: the fluid phase,  $f$ , corresponding to the resin flow inside the preform and the solid phase,  $s$ , of the CNF (or any other natural fiber) preform. Based on the volume averaging theorem developed by Whitaker [1], the first averaging theorem is used to transform the phase average of the divergence of any vector quantity into the divergence of the phase average of the same quantity:

$$\langle \nabla \cdot \mathbf{q}_f \rangle = \nabla \cdot \langle \mathbf{q}_f \rangle + \frac{1}{V_{REV}} \int_{A_{fs}} \mathbf{q}_f \cdot \mathbf{n}_{fs} dA \quad (A1)$$

The angled brackets signify the volume average of any physical quantity. Here  $\mathbf{q}_f$  is the vector quantity,  $A_{fs}$  is the fluid-solid interface area within an REV,  $\mathbf{n}_{fs}$  is the unit normal to the interface, and  $V_{REV}$  is the REV volume. (REV stands for Representative Elementary Volume that is used for doing volume integrals during the volume averaging process [111].) The second

averaging theorem is used to convert the volume average of the time-derivative of any quantity into the time-derivative of the volume average of the same quantity:

$$\left\langle \frac{\partial q_f}{\partial t} \right\rangle = \frac{\partial \langle q_f \rangle}{\partial t} - \frac{1}{V_{REV}} \int_{A_{fs}} q_f \mathbf{v}_s \cdot \mathbf{n}_{fs} dA \quad (\text{A2})$$

Here  $q_f$  is a scalar quantity while  $\mathbf{v}_s$  is the velocity of the fluid-solid interface.

After defining the 1<sup>st</sup> and 2<sup>nd</sup> volume averaging theorem, let us now undertake the derivation of the volume-averaged form of the new continuity equation. The point-wise continuity equation for the flow of a Newtonian liquid through the pore space of a swelling, liquid-absorbing porous media can be expressed as

$$\nabla \cdot \mathbf{v}_f = 0 \quad (\text{A3})$$

On taking the volume average of this equation and applying the 1<sup>st</sup> averaging theorem, it can be written as

$$\nabla \cdot \langle \mathbf{v}_f \rangle + \frac{1}{V_{REV}} \int_{A_{fs}} \mathbf{v}_f \cdot \mathbf{n}_{fs} dA = 0 \quad (\text{A4})$$

On adding and subtracting the surface integral of  $\mathbf{v}_s$  ‘dotted’ with the differential area on the interface, we get

$$\nabla \cdot \langle \mathbf{v}_f \rangle + \frac{1}{V_{REV}} \int_{A_{fs}} \mathbf{v}_s \cdot \mathbf{n}_{fs} dA + \frac{1}{V_{REV}} \int_{A_{fs}} (\mathbf{v}_f - \mathbf{v}_s) \cdot \mathbf{n}_{fs} dA = 0 \quad (\text{A5})$$

On assuming  $q_f$  being equal to unity in the 2<sup>nd</sup> average theorem, Eqn. (A2), and noting that  $\langle 1 \rangle = \varepsilon_f$ , we obtain

$$0 = \frac{\partial \varepsilon_f}{\partial t} - \frac{1}{V_{REV}} \int_{A_{fs}} \mathbf{v}_s \cdot \mathbf{n}_{fs} dA \quad (\text{A6})$$

On using Eqn. (A6) with Eqn. (A5), we have

$$\nabla \cdot \langle \mathbf{v}_f \rangle + \frac{\partial \varepsilon_f}{\partial t} + \frac{1}{V_{REV}} \int_{A_{fs}} (\mathbf{v}_f - \mathbf{v}_s) \cdot \mathbf{n}_{fs} dA = 0 \quad (\text{A7})$$

On describing the third term as sink,  $S$ , in Eqn. (A7), we can express the new volume-averaged continuity equation as

$$\nabla \cdot \langle \mathbf{v}_f \rangle = -S - \frac{\partial \varepsilon_f}{\partial t} \quad (\text{A8})$$

Here  $S$  represents how much liquid volume is absorbed within an REV by the solid phase during its swelling after exposure to the liquid phase.

Eqn. (A8) is a simple but powerful result that emerges from applying the two averaging theorems to the point-wise continuity equation. In the right hand side of Eqn. (A8), the first term  $-S$  is a negative term while the second term is positive (i.e., a source term) because the porosity decreases with time due to the progressive squeezing-out of the pore space between the solid phase during swelling. Since the left hand side of Eqn. (A8) represents the divergence of the macroscopic fluid velocity, the positivity or the negativity of the right hand side implies that the fluid velocity will either *accelerate* or *decelerate*, respectively. At this stage, the new continuity equation leaves us at a tantalizing point—the relative strengths of the source and sink terms will decide whether the macroscopic velocity speeds up or slows down during liquid infusion into a swelling preform.

By using the simplification developed by Masoodi et al. [109, 110] which proposed that the sink term,  $S$ , is proportional to the rate of increase of the solid-phase volume which is directly

proportional to the rate of change of the porosity. Using these suppositions,  $S$  can be reformulated as

$$S = b \frac{\partial \varepsilon_s}{\partial t} = -b \frac{\partial \varepsilon_f}{\partial t} \quad (\text{A9})$$

Note that here  $b$  is described as the *absorption coefficient* and falls in the range  $0 \leq b \leq 1$ . One can allow  $b$  to be greater than 1 if the increase in solid volume is larger than the volume of the liquid being absorbed by the solid phase. Here  $\varepsilon_s$  is the fiber volume fraction while  $\varepsilon_f$  is the porosity. Using Eqn. (A9) in Eqn. (A8) leads to the penultimate form of the continuity equation for swelling medium as

$$\nabla \cdot \langle \mathbf{v}_f \rangle = (b-1) \frac{\partial \varepsilon_f}{\partial t} \quad (\text{A10})$$

In the case of  $b=1$ , the right hand side of Eqn. (A10) reduces to zero and this equation is reduced to the classical mass-balance equation which is commonly used for flows in rigid non-swelling porous media. In such a situation, the rate of decrease in liquid volume around the solid phase due to the sink effect is compensated by the rate of increase in solid volume due to swelling. Then the macroscopic flow velocity neither accelerates nor decelerates due to the preform absorption effects.

## **CHAPTER 5: Mechanical, Physical and Tribological Characterization of Nano-Cellulose Fibers Composites**

### **5.1. Introduction**

In recent years, the natural fibers have been considered as an alternative to the synthetic fibers for reinforcement in polymeric composites because of the economic and environmental advantages. The increasing world awareness of the environmental issues along with an intensification of the global energy crisis has generated an interest in utilizing natural fibers in industries and academics [3, 112]. Other advantages of natural fibers compared to synthetic fibers are - abundance, non-toxicity, non-corrosiveness, bio-degradability, lower cost, and low energy production costs - which makes them potential candidates in the secondary structural applications in automotive industry, including door panel and package trays [113, 114]. In recent years, many investigators have conducted research on different types of natural fibers as reinforcement for various polymer matrices. The effects of using plant-derived fibers, such as hemp, jute, kenaf, bamboo and treated palm-tree fiber on mechanical strength, stiffness, thermal and tribological properties of the produced composites have been investigated. It was found that the natural fibers possess poor mechanical properties as compared to the synthetic fibers, such as the carbon and glass fibers. As a result, the natural-fiber composites suffer from low mechanical, thermal and tribological properties. These poor properties are essentially due to the inherent polarity and their incompatibility with non-polar polymers. [115-121].

Many studies have been conducted in recent years to investigate the mechanical properties of the natural-fiber reinforced composites. Several factors on the influence of natural fibers on mechanical performance of the composites have been studied. These factors include interfacial adhesion, orientation, strength and physical properties of the fibers. Alwar et al. [115] investigated

the effects of chemical treatment on surface morphology for date palm tree fibers. Based on their study, fibers treated with 1% Sodium Hydroxide (NaOH) solution showed the optimum mechanical properties of the composites. However, hydrochloric acid (HCl) treatment resulted in deterioration in mechanical properties of the composites. Saha et al. [120] studied the influence of alkali treatment on tensile strength of jute fiber reinforced composites under ambient temperature. Their investigation indicated that dipping fibers in alkali solution lead to an increase in the tensile strength of the composites. Furthermore, several studies have showed a positive effect of adding kenaf, hemp and cotton fibers to alkali solution to enhance the tensile strength of Polypropylene composites [122, 123]. Plackett et al. [124] reported that adding jute fibers to polylactic acid (PLA) enhanced the tensile strength of the composites up to 75%. Barari et al. [52] studied the effects of silane treatment on bonding between cellulose nano-fibers and epoxy, and detected its overall effect on mechanical properties of the final composite. This study also includes other aspects, such as moisture absorption, impurities and volume fraction which play an important role on the properties of manufactured composite. Masoodi et al. [19] studied the crack behavior of cellulose nano-fiber composites.

Determining an optimum value of fiber volume fraction for the best strength is another significant topic in field of composites. Hence, the effects of fiber volume fraction on the strength-related properties have been investigated by several researchers. These studies have shown that the natural fibers tend to weaken the bonding with the matrix at high fiber volume fraction ( $>> 50%$ ) [122, 125-127]. Further, some studies have reported on the influence of fiber-matrix interface on mechanical properties of the composites as it is a key parameter in transferring stress from the matrix to the fibers [128].



The tribological properties of polymeric composites reinforced by natural fibers have been a topic of interest in the field of green tribology in recent years [129]. As most of the engineering parts are exposed to tribological effects, such as adhesion and abrasion, understanding the tribological behavior of the natural fiber reinforced composite is as essential as understanding the mechanical performance of the composites. Some research has been done on investigating the tribological properties of natural-fiber reinforced composites, such as wear and frictional behavior of polymer composites reinforced with kenaf [117], oil palm [130], and bamboo [131], jute [132]. These studies have shown a diverse tribological behavior based on the type of reinforcement used in the composites. However, no investigations have been conducted till date on the effects of natural nano-fibers on the tribological behavior of nanocomposites.

Cellulose nano-fiber (CNFs), a new type of natural nanoscale fiber, made purely from cellulose molecules, have shown a remarkable mechanical properties compared to other natural fibers as well as glass and carbon fibers [8, 9, 13]. However, a drawback of using nano-fibers in the last few decades was due to a bottleneck in their manufacture from cellulose molecules due to the extremely high energy needed till now to separate cellulose molecules from pulp. Recent improvement in the technologies and techniques for making highly porous cellulosic nano-fiber based aerogels reduced the production costs to reasonable values. This led to an increased interest on investigating many aspects of the composites using CNFs as reinforcement in natural composites in the last few years [10, 26, 31]. Aerogels are light-weight and highly porous materials that are prepared by removing liquid solvent from a gel, as a result of which a solid skeleton is created with large number of pores inside the solid phase. Formation of aerogels is usually accomplished through common processes including freeze-drying and vacuum-drying. CNF aerogels owing to low density ( $0.004\text{--}0.5\text{ g/cm}^3$ ) and very high porosity (above 90%) can be

employed as a porous reinforcement that can be easily infiltrated with resin under pressure to manufacture composites [102-104].

In this chapter, the silylated and non-silylated CNF aerogels were used as reinforcements and a bio-based epoxy as the matrix materials for making CNF/epoxy nanocomposite using an improvised Liquid Composite Molding (LCM) process. The curing of silylated and non-silylated CNF composites was investigated through isothermal and non-isothermal Differential Scanning Calorimetry (DSC) tests. Mechanical properties, such as tensile strength and modulus of elasticity of these composites were investigated using the traditional tensile-testing process. The effect of silane treatment on the mechanical properties of nanocomposites was also studied by comparing the strengths of the treated and non-treated samples. Tribological investigations, such as the friction coefficient and wear behavior of the CNF composites were studied under various sliding speeds and loads. The worn surfaces were analyzed using Scanning Electron Microscopy (SEM) and optical profilometer.

## **5.2. Manufacturing process**

### **5.2.1. Cellulose nano-fiber (CNF) aerogels**

The CNF aerogels used in the present investigation were derived from commercially-supplied Eucalyptus Kraft pulp which were used as raw material and were processed using acid hydrolysis, TEMPO (tetramethylpiperidine-1-oxyl) oxidation, and mechanical stress. The CNF aerogel preparing process was initiated with washing, pre-treating and soaking of the Eucalyptus Kraft pulp with acid and water, and then filtering the pre-treated fibers. After filtration, the products were carboxylate with the reactants according to Saito's methodology [26]. The centrifugation process was used to facilitate the separation of coarse and fine fractions. Then, a nano-fiber suspension was prepared using microfluidizer. In the final step, the CNF preforms were

prepared from the nano-fiber suspension using the freeze-drying process. The process could be manipulated to create either randomly oriented pore or highly aligned unidirectional pores in the preforms [57]. This micro-scale structure would allow the preform to be used as high-porous preforms for making CNF composites. In order to increase the wettability and infusion properties of such preforms, the CNF preforms were placed in a glass vacuum desiccator above 1mL of trimethoxy-octadecyl silane (for each preform) and stored in a vacuum oven at 1 inch Hg and 120°C for 18hrs.

### **5.2.2. Manufacturing of CNF composites using an improvised Liquid Composite Molding (LCM) process**

The CNF composites are manufactured using an improvised LCM process where the CNF aerogels are used as preform and the bio-based epoxy as the matrix. The improvised LCM process was essentially based on a conventional vacuum-assisted resin transfer molding (VARTM) process where a vacuum up to 100 kPa was applied to pull the resin through the preform inside a mold [52, 133]. The experimental setup consists of a vacuum pump, a resin trap and a ‘micro’ LCM mold. The micro LCM mold was made from aluminum and sealed by polycarbonate cap at the top. Two aluminum portable inserts, used to create tensile and flexural specimens, were placed inside the base slab. The transparent Lexan<sup>®</sup> cap was employed to air seal the mold and also used as a window to track the resin movement inside the mold.

The bio-based resin used in the present experimental processes was Super-Sap Entropy<sup>®</sup> [27], which is derived from industrial waste products, such as wood pulp, and has an overall bio-content of around 50%. This resin was designed to be cured at room temperatures, and thus has an enhanced processability during the VARTM process.

In the manufacturing process, the cellulose preform was placed inside the mold cavity (Figure 15) while the Lexan<sup>®</sup> cap was fastened on the top. The inlet vent was connected to a beaker full of curing resin and the outlet vent was connected to the resin trap in order to prevent any leakage of the resin to the inside of the vacuum pump. During the process, the resin was made to pass through the porous and permeable preform along the mold cavity and then was made to exit through the outlet vent to the resin trap. The resin was set and cured for 24 hours and then the specimens were removed from the mold. Thereafter, the specimens were placed inside an oven that was set at 130 °C for 20 minutes. The freeze-dried CNF preform, being an aerogel, typically had very low solid-phase volume fractions. As a result, the manufactured CNF composite had very low fiber volume fractions (FVF) where the samples typically had FVF from 0.9 to 1.4 %. For tribological studies, cylindrical samples with hemispherical-shaped tip were prepared from the specimen by machining.

### **5.3. Characterization and testing**

#### **5.3.1. Differential scanning calorimetry tests**

Differential scanning calorimetry (DSC) tests were performed on the prepared samples using a Q1000 DSC developed by TA Instruments. In these experiments, 25 mg of uncured bio-epoxy fiber composite was placed in T-Zero aluminum pans under 50 mL/min of nitrogen purge gas. To study the curing process of the composites, both the isothermal and non-isothermal tests were performed. In addition, the glass transition temperature of the cured composites was measured by performing additional heating and cooling cycles. Three individual tests were carried out to ensure reliability of measurements. For non-isothermal tests, a heat-cool-heat cycle for temperature range between -60 to +250 °C at a heating rate of 10 °C/min was used for the uncured sample. The onset temperature for curing ( $T_{on}$ ), the melting temperature ( $T_m$ ), and the glass

transition temperature ( $T_g$ ) were obtained using the Universal Analysis 2000 software that is attached to the data acquisition electronics of the DSC.

For isothermal studies, three different temperatures were selected based on the curing peak position of the non-isothermal tests. The temperatures were selected in such a way that it should range between a temperature below the onset of the reaction, a temperature midway to the peak maximum, and a temperature well above the peak position. Prior to performing isothermal experiments, the chamber was heated to the desired isothermal temperature using an initial temperature program segment. The chamber was rapidly opened for loading the sample and was then immediately closed. When the measured temperature was within 4°C of the desired isothermal temperature, the data acquisition was initiated.

### **5.3.2. Mechanical characterization**

The tension coupons prepared from CNF/bio-epoxy composite were tested using a tensile testing machine. The loading force was set using a displacement controlled device at the rate of 1.3 mm/min (0.05 in/min). The crosshead displacement and loading force were recorded during the experiments. The load was applied through an electro-mechanical test system with a 97 kN capacity. A sample length of 89 mm (3.5 in) was considered as the gauge length in the tensile testing process. All the specimens were tested by the same operator using the same testing machine in order to avoid any errors that might occur due to variations in the testing conditions. The CNF composites with various fiber volume fractions were tested and the strength and module of elasticity values were compared. In addition, the effects of silane treatment on mechanical properties of CNF composites were investigated in order to compare the tensile strength and elastic modulus values.

### 5.3.3. Tribological characterization

The pin-on-disk tests (ASTM G99) under dry condition were performed to investigate the tribological behavior of the composites at ambient conditions. In the test, a stationary pin was made to slide against a rotating disk. From the fabricated composite specimens, cylindrical samples (10 mm in length, 3 mm in diameter, and with rounded contact surface) were prepared by machining. The disks were made of hardened 440C stainless steel with hardness of 230 HBN and initial surface roughness ( $R_a$ ) of  $0.3\pm 0.05$   $\mu\text{m}$ . The disk dimensions were 55 mm in diameter and 10 mm in thickness. In addition, the tribological properties were studied by varying the tribological testing parameters, such as normal loads (4N, 7N and 10N) and sliding speeds (low (0.15 m/s), medium (0.25 m/s) and high (0.35 m/s)). For each test, the sliding distance was fixed to 1 km in order to consider the steady-state friction values. The COF (coefficient of friction) value presented for each test was the average of the friction values. In addition, the linear wear-loss was acquired through a linear variable differential transducer (LVDT) with an encoder, which recorded the vertical displacement of the pin. After the tests, the worn surfaces were analyzed using SEM. The linear wear loss of each pin was converted into a volumetric wear loss using Eq. (5.1) derived from the geometry of a spherical cap.

$$V = \frac{\pi h^2}{3}(3r - h) \quad (5.1)$$

In Eq. (5.1),  $h$  is the linear displacement (mm) in the vertical (longitudinal) axis for the pin,  $r$  is the pin radius (mm), which is assumed to be constant throughout the test, and  $V$  is the volumetric wear loss ( $\text{mm}^3$ ). For a given set of testing conditions, at least three repetitive tests were performed and the results of the average of three tests were presented.

## 5.4. Results and discussion

### 5.4.1. DSC characterization

#### 5.4.1.1. Dynamic DSC characterization

The effects of coupling agents on curing of the fiber/bio-epoxy composites were systematically studied using dynamic DSC methods by analyzing temperature ramp curve for pure bio-epoxy, cellulose nano-fibers (CNFs)/bio-based epoxy composites, and chemically modified silylated cellulose nano-fibers (CNFs)/bio-based epoxy composite. All thermographs showed an exothermic peak ranging from 40°C to 150 °C. The onset temperature for curing ( $T_{on}$ ), the melting temperature ( $T_m$ ), and the glass transition temperature ( $T_g$ ) are presented in Table 9.

*Table 9. Characteristic temperatures of pure bio-epoxy and composites, obtained using the temperature ramp analysis*

	$T_m$	$T_{on}$	$T_g$
Pure bio-epoxy	128	87	73
Silylated CNF/ Bio-epoxy composite	125	79	55
Non- silylated CNF/ Bio-epoxy composite	124	87	57

Compared to the pure bio-epoxy sample, the onset temperature for curing for the unmodified CNF remained unchanged, however, the onset temperature was decreased for the fiber modified CNF. The peak temperature ( $T_m$ ) remained almost unaffected for both the surface modified and unmodified fibers. These variations can be explained by the catalytic effects of the fibers during the curing process of bio-epoxy. At the initial stages of curing, the decrease in the onset temperature can be considered as an evidence of acceleration in curing in the early stage of the

curing process. Siloxane functional groups ( $-\text{SiO}_2$ ) on the surface of the CNF react with the bio-epoxy ring and this is expected to modify the curing behavior. The slight acceleration in curing of the unmodified fibers in the early stage of the reaction is a result of decrease in the activation energy with the addition of the CNF. However, fibers hinder the reaction after that step and this can explain the unchanged peak temperature of the pure and filled bio-epoxy. The lack of bio-epoxy-chain mobility in the presence of fibers retards the polymer chain extension process.

The thermo-mechanical stability of polymers is closely related to their glass transition temperature, which itself would change with the molecular structure, the functionality of the system, the degree of the cure, the type of the curing, etc. The glass transition temperature of a system is expected to increase with a decrease in the chain mobility. The glass transition temperatures of the CNF reinforced composites are lower than those of the unfilled bio-epoxy. This is because of the restricted mobility of the polymer chains in the vicinity of the fibers. In addition, the fibers are also inducing a stiffening effect that promotes  $T_g$ .

#### **5.4.1.2. Isothermal DSC**

The isothermal DSC characterization of the silylated and non-silylated CNF composites for three different temperatures was conducted. The variation of heat flow with time is shown in Figure 33a. As displayed in the isothermal results (Figure 33b), both silylated and non-silylated samples reached to full conversion at  $130^\circ\text{C}$ . At the higher temperatures, the silylated samples reached the maximum conversion in a shorter time compared to the non-silylated samples while this tendency was quite the opposite at lower temperatures. The silylated samples showed higher conversion by increasing the isothermal temperature. However, this effect was more pronounced when the temperature was high enough. By increasing the temperature in the isothermal DSC process, the time required to achieve full conversion was decreased. This implies that the fiber



induced modification was enhanced only during the initial stages of curing by decreasing the activation energy. In addition, the kinetic parameters were calculated using the normalized heat flow vs time curves as shown in Figure 1b where the normalized curves were used to derive an equation for curing percentage as a function of time. The equation model is derived using the Sigmoidal Dose-Response equation as

$$\alpha(t) = A_1 + \frac{A_2 - A_1}{1 + 10^{[(\text{Log} t_0 - t)p]}} \quad (5.2)$$

where  $A_1$  is the y-minimum plateau,  $A_2$  is the y-maximum plateau,  $\text{Log } t_0$  is the t value when  $\alpha(t)$  is halfway between the bottom and the top, and p is the hillslope or the steepness of the curve. All the above mentioned parameters for the conversion equation are presented in Table 10.

*Table 10. Parameters of Eqn. (5.2), conversion equation as a function of time parameters.*

<b>Temperature</b>	<b>Sample</b>	<b>A<sub>1</sub></b>	<b>A<sub>2</sub></b>	<b>Logt<sub>0</sub></b>	<b>p</b>
80	Silylated	-13.9	1	-14.48	0.07
	Non-silylated	-20.33	1	-13.33	0.1
100	Silylated	-2635.72	0.98	-22.56	0.15
	Non-silylated	-875.02	0.99	-11.25	0.25
130	Silylated	-0.73	1	0.15	1.27
	Non-silylated	-4.5	1	-0.73	0.82

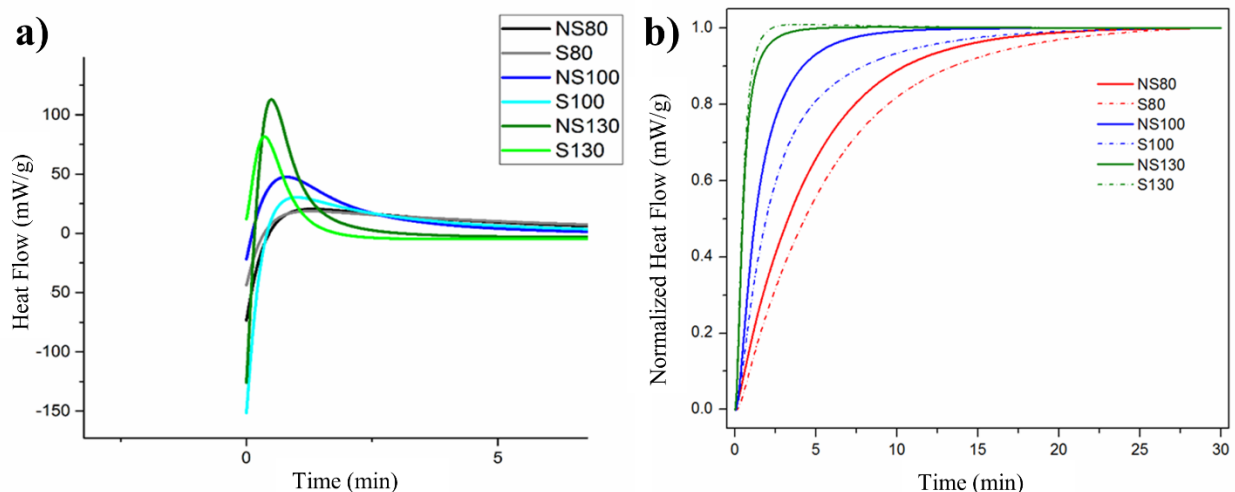


Figure 33. a) Variation of heat flow with time for the silylated “S” and non-silylated “NS” CNF samples at 80, 100 and 130 °C and b) Normalized Heat flow with time diagram for silylated and non-silylated CNF samples at 80, 100 and 130 °C.

#### 5.4.2. Mechanical properties

The stress-strain diagram measured by tensile test for the silylated and non-silylated CNF composite samples is shown in Figure 34. As shown in the stress-strain diagram, the silylated CNF shows superior ultimate tensile strength and higher modules of elasticity when compared to the non-silylated samples. The stress-strain relations for the silylated and non-silylated CNF composites are almost linear at the beginning and the linearity declines with increasing strain. In general, the CNF reinforced specimens showed a nonlinear stress-strain response that indicates lowering of the brittleness of the bio-epoxy composites in the presence of CNF preform. This could be explained by the observed formation of dry spots inside the composite at the CNF/bio-epoxy interface due to incomplete infusion of CNF preforms.

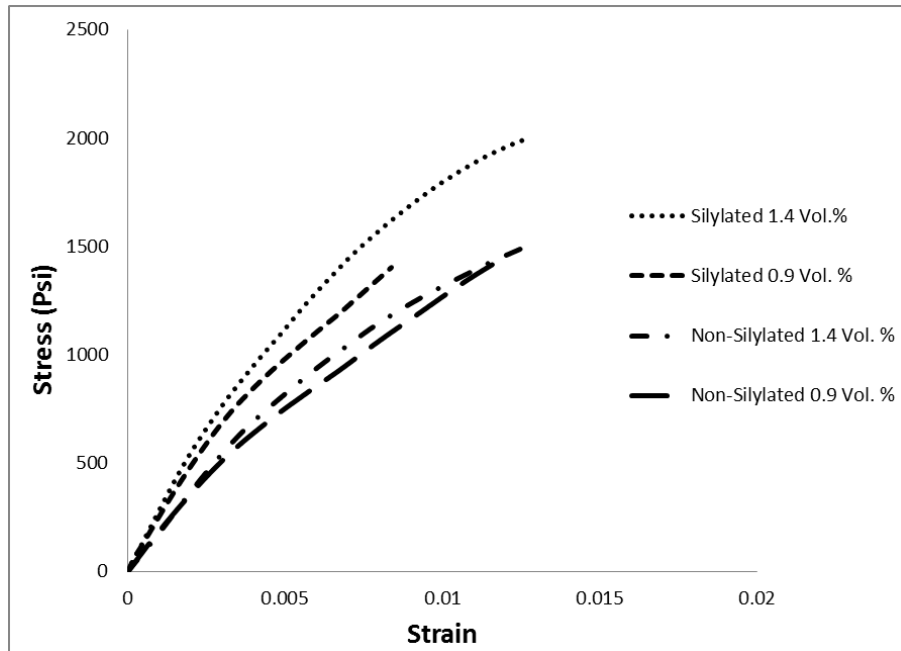
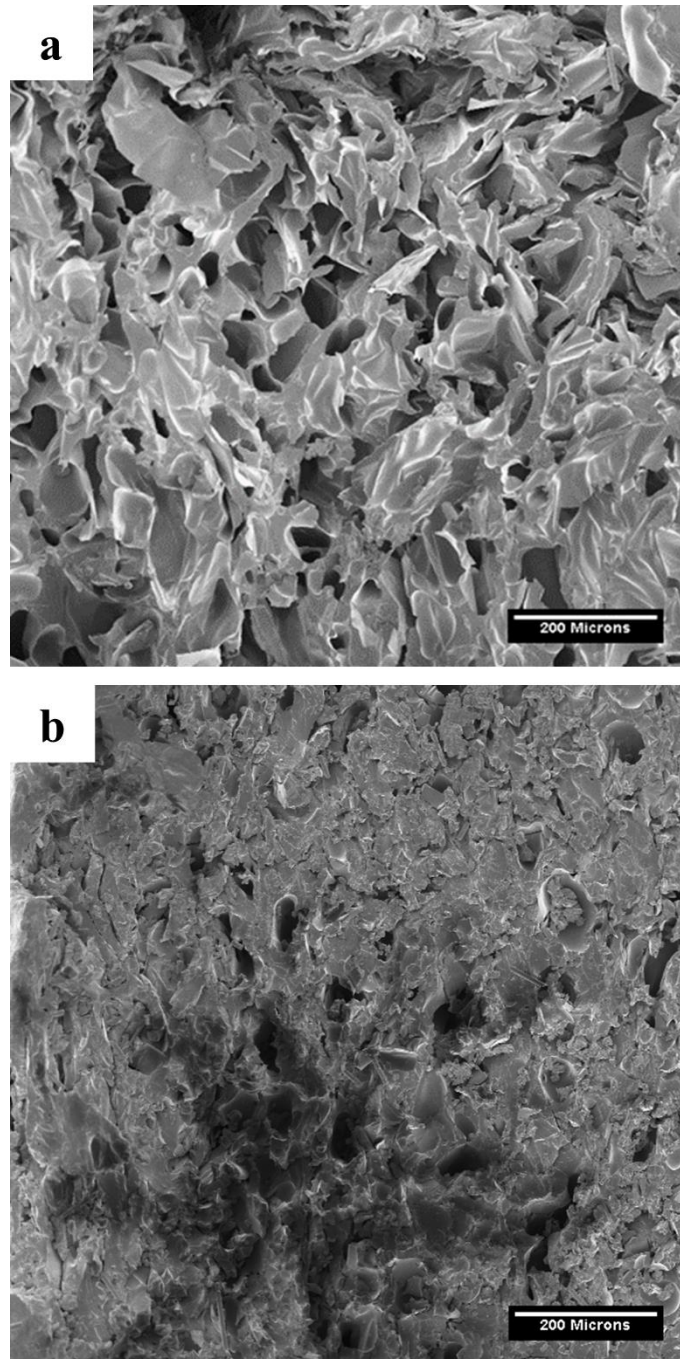


Figure 34. Experimentally measured stress-strain curves for the CNF/bio-epoxy composites

The SEM micrographs of the fractured surface of the CNF composites are shown in Figure 35. The silylated sample shows much less bubbles or voids compared to the non-silylated sample; the latter displays more numerous round voids. This difference can be attributed to the better wettability of the CNF preform by the resin in presence of the silane agent. The silane agent also improves the mechanical entanglement between the CNF reinforcement and bio-epoxy matrix due to better bonding between them during the curing process. Both these effects (i.e., reduced void formation and improved entanglement) work together to create a better CNF composite.



*Figure 35. SEM micrographs of: (a) non-silylated CNF composite, (b) silylated CNF composite.*

### **5.4.3. Tribological Properties**

In the pin-on-disk experiments, the continuous rotating steel counterface slide against the stationary surface of the sample (composite material). This rubbing action results in creation of

continuous grooves on the specimen surface, and subsequently the material detaches from the specimen surface due to continuous rubbing, and finally leading to material removal from the specimen surface. As the mechanical properties of the composites reinforced by silylated CNF are superior to those of the composites reinforced by non-silylated CNFs and it is well known that the mechanical properties strongly influence tribological properties [134], hence, the tribological properties of silylated CNFs/bio-epoxy composites were investigated in this study. Experiments were performed to determine the influence of the presence of nano-cellulose in the bio-epoxy matrix on the tribological properties, such as coefficient of friction (COF) and wear volume loss of the composites.

#### **5.4.3.1. Effect of volume fraction**

Figure 36 (a), (b) and (c) shows the effect of the presence of nano-cellulose in the bio-epoxy matrix on COF at different normal loads and sliding speeds. In the figures, the connecting data points pertain to the average values of the three tests. Figure 36(a) shows the variation of the COF with volume fraction of nano-cellulose in the bio-epoxy matrix at 4N, 7N and 10 N for a sliding speed of 0.15 m/s. It can be seen that the COF decreases with increasing volume fraction of nano-cellulose in the bio-epoxy for all the three normal loads during the low sliding speed of 0.15 m/s. Interestingly, the reduction in COF is significant for larger normal loads. It is also obvious that the reduction in friction is substantial when the volume fraction of nano-cellulose is increased from 0% to 0.9% than 0.9% to 1.4%. It can be inferred from Figure 36(a) that the neat bio-epoxy showed better tribological performance at lower normal loads and the 1.4% composite showed better tribological performance at higher normal loads due to the presence of nano-cellulose on contact surfaces.

Figure 36(b) shows the variation of COF with volume fraction of nano-cellulose in the bio-epoxy matrix at 4N, 7N and 10 N when the tests were performed for a constant sliding speed of 0.25 m/s. Akin to 0.15 m/s, the coefficient of friction decreases when 0.9% volume fraction of nano-cellulose was added to the bio-epoxy for all the three normal loads. However, the COF increases for 4N and 7N when 1.4% nano cellulose added to the bio-epoxy matrix, although, they have lower COF than the neat bio-epoxy. Interestingly, for 10N, the COF continuously decreases although the reduction in COF is less substantial. Incidentally, the 10N load led to the lowest COF. Here too, the neat bio-epoxy showed better tribological performance at lower normal loads and the 1.4% composite showed superior tribological performance at higher normal loads.

Figure 36(c) shows the variation of COF with volume fraction of nano-cellulose in the bio-epoxy matrix at 4N, 7N and 10 N for a constant sliding speed of 0.35 m/s. At this high sliding speed, the variation of COF with volume fraction of nano-cellulose showed completely different trends. At 4N normal load, the variations in the COF is increased when 0.9% volume fraction of nano-cellulose is added to the bio-epoxy matrix and then the COF is slightly decreased when 1.4% nano-cellulose is added to the bio-epoxy matrix. The COF was found to be lowest for the neat bio-epoxy when compared to the nano composites. For 7N normal load, the COF does not change much with nano-cellulose volume fraction. Interestingly, at the highest normal load of 10N, the COF decrease with the increasing volume fraction of nano-cellulose as observed for the 0.15 m/s and 0.25 m/s sliding speeds. From the above results, it can be inferred that the neat bio-epoxy has poor tribological properties and suitable only at low loads and low sliding speeds applications. However, for severe tribological conditions, the higher volume fraction of the nano-cellulose would be preferred in the CNF composites.

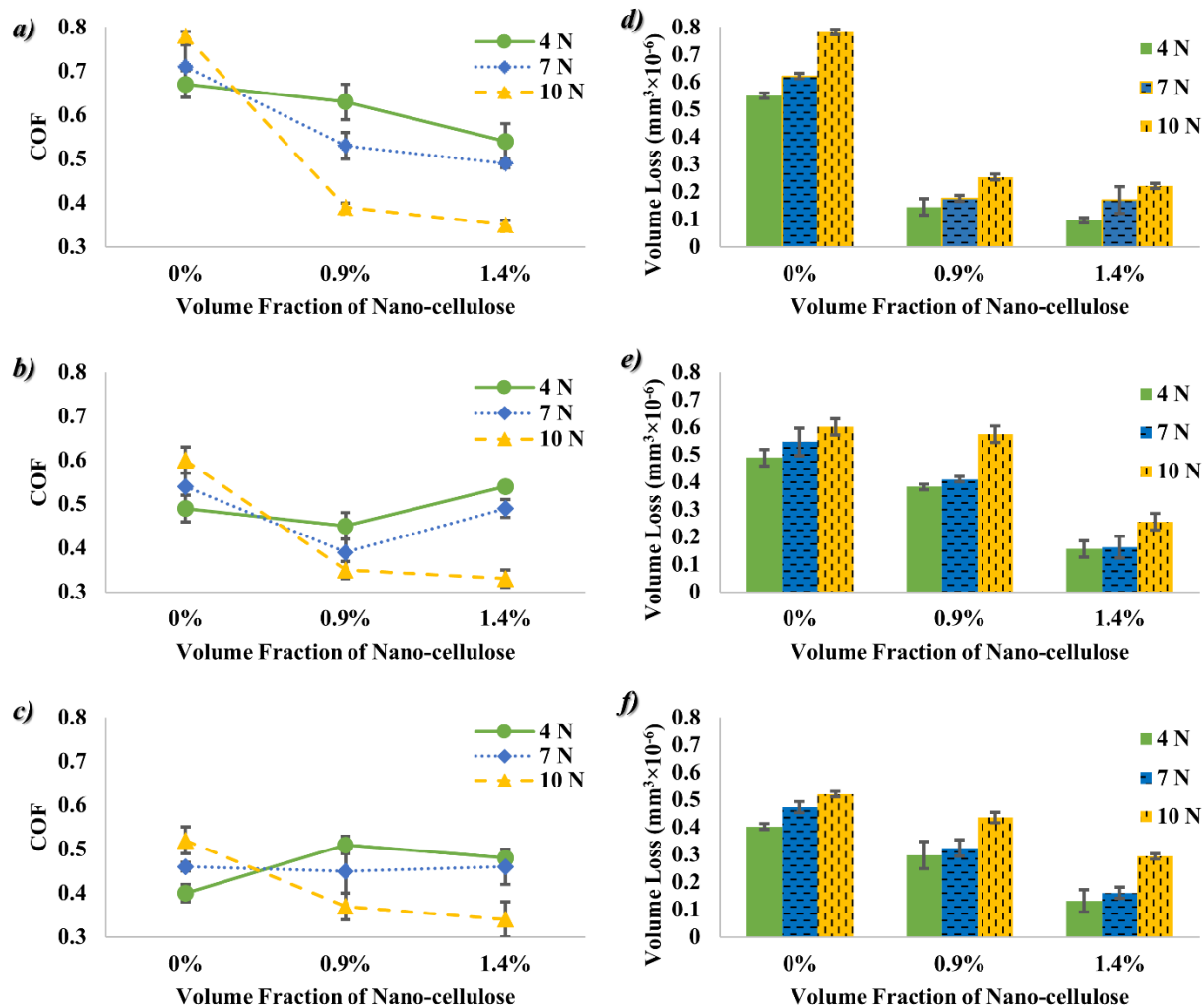


Figure 36. Effect of nano-cellulose content in bio-epoxy on coefficient of friction at different normal loads for a) 0.15 m/s, b) 0.25 m/s, and c) 0.35 m/s sliding speeds and effect of nano-cellulose in bio-epoxy on wear volume at different normal loads for d) 0.15 m/s, e) 0.25 m/s, and f) 0.35 m/s sliding speeds.

Figure 36(d), (e) and (f) show the variation of wear rate (volume loss) with volume fraction of nano-cellulose in the bio-epoxy matrix for various normal loads (4N, 7N and 10 N) at sliding speeds of 0.15 m/s, 0.25 m/s and 0.35 m/s, respectively. It can be seen that for a given volume fraction, the wear rate increases with increasing normal load. The wear rate decreases with the increasing volume fraction of the cellulose in the bio-epoxy matrix. Furthermore, the wear rate

decreases with the increasing sliding speed. The volume loss in nano-cellulose/bio-epoxy composites is significantly less than that of the neat bio-epoxy. This is because the incorporation of nano-cellulose in the bio-epoxy matrix effectively improves the mechanical and tribological properties of bio-epoxy due to the enhancement in strength properties as shown in Figure 34 and the ability of nano-cellulose fibers to resist the bending force as reported in the literature [135]. Although, the hardness of the material has long been regarded as a primary material property that defines the wear resistance, there are strong evidences to suggest that the elastic modulus can also have an important influence on the wear behavior [136]. Subsequently, the bio-epoxy matrix reinforced by 1.4% CNFs have better wear properties due to higher elastic modulus as shown in Figure 34. In addition, the cellulose fibers play a significant role in enhancing fracture toughness of polymer matrices through several energy absorbing mechanisms, such as fiber pullout, fiber fracture and fiber-bridging [51]. These mechanical factors have significant effect on the tribological properties of nano-cellulose/bio-epoxy composites. Besides, the addition of nano-cellulose into bio-epoxy results in an improvement in the COF and reduction in the volume loss of nanocomposites. In general, as demonstrated in Figure 36 (d), (e) and (f), superior improvement in wear rate occurred at the highest volume fraction of CNFs due to the increase in stress transferred to the fiber and the ability of cellulose fibers to resist the bending forces [137] and can carry the major load and support the bio-epoxy matrix. Table 11 shows the amount of improvements in COF and wear rate of the CNFs reinforced composites.

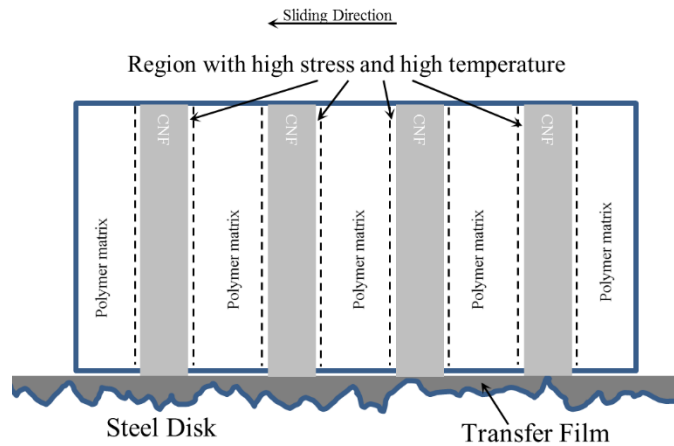


Table 11 Summary of improvement in COF and wear rate of composites

Sliding Speed	Load	CNFs Volume Fraction			
		0.9%	1.4%	0.9%	1.4%
		COF Improvement		Volume Loss Improvement	
0.15 m/s	4 N	6.0%	19.4%	73.8%	82.5%
	7 N	25.4%	31.0%	71.7%	72.6%
	10 N	50.0%	55.1%	67.5%	71.6%
0.25 m/s	4 N	8.2%	- 10.2%	21.9%	67.9%
	7 N	27.8%	9.3%	25.0%	70.2%
	10 N	41.7%	45.0%	4.5%	57.4%
0.35 m/s	4 N	- 27.5%	- 20.0%	25.6%	66.9%
	7 N	2.2%	0.0%	31.3%	65.8%
	10 N	28.8%	34.6%	16.5%	43.6%

Figure 37 presents a schematic illustration of the wear mechanisms prevalent during sliding wear of the composites reinforced by CNFs. The continuous transfer film formed during the running-in stage is mainly composed of worn matrix material and can effectively reduce the ‘direct contact’ of the composite with asperities of the hard metallic counterface [138, 139]. During the sliding process, the CNFs reinforcement may carry most of the contact load and wear against the counterpart. Furthermore, thermal–mechanical failure of the material in this contact region may

occur, due to the high friction and local heating [140]. In this case, the polymeric matrix in the interfacial region around CNFs solid phase suffers higher stress and temperature. As a result, the CNFs will be removed more easily which is associated with a progressive increase in the wear rate of the composites. Therefore, detached CNFs solid phase can fill the gap between the asperities and reduce the roughness of the counterpart and consequently, decrease the COF and volume loss.



*Figure 37. Schematic illustration of the failure mechanism for the sliding wear of CNFs/bio-epoxy nanocomposites*

To understand the role of nano-cellulose fibers on the wear mechanism, two composite samples with different CNFs contents and a neat bio-epoxy sample were chosen for comparison. Their worn surfaces were further investigated by using stereo-macrograph and SEM. The texture of worn surfaces clearly depicts the composition-dependent wear behavior. For comparison purpose, all the selected samples were subjected to the same normal loads and sliding speed. The surface damage on the worn surface is decreased by adding nano-cellulose to the bio-epoxy matrix. This reduced the wear volume loss and hence the nanocomposites showed improved wear resistance when compared to the neat bio-epoxy materials as there were no fibers to support the matrix of neat bio-epoxy. Hence, the important reason for better wear resistance of the composites is the load bearing ability of CNFs in the matrix. Moreover, by increasing the content of CNF,

more fibers can shoulder the load which tends to decrease the wear rate at higher volume fraction of CNFs. The SEM image of the worn surface of neat bio-epoxy showed more debris and fine cutting chips similar to those produced during machining. It means that the wear mechanism of neat bio-epoxy is abrasive. The detached debris act as third body abrasive. These debris can further increase the depth of the grooves by ploughing action and the material is continually displaced sideways to form ridges adjacent to the developing groove by plastic deformation. In addition, the debris can cut the surface similar to micromachining and all the material displaced by the debris is removed as a chip. Consequently, the volume loss increases in neat bio-epoxy as confirmed by the experimental results presented.

On the other hand, a minimal amount of debris is seen on the surface of 0.9% CNFs/bio-epoxy composites and no debris are found on the surface of 1.4% CNFs/bio-epoxy composites. Therefore, the composites exhibited lower wear rates. The SEM image of the worn surfaces exhibit that the dominant wear mechanism for the composites is adhesion due to plastic deformation and in some regions transfer layer is seen on the composite surfaces. A distinguishing feature of this wear process is the back transfer of material from one surface to another where iron from steel is transferred to the polymer surface [141]. A similar observation is reported in the literature where a soft aluminum materials slide against a hard steel counter material and iron from the steel counter material is transferred to the soft aluminum sample surface [142, 143]. This phenomena occurs due to the localized bonding between the contacting solid surfaces [138]. Because of the presence of some debris on the worn surface of 0.9% CNFs/bio-epoxy composites, the wear mechanism for this composite is a combination of abrasion and adhesion with latter being dominant. On the other hand, the wear mechanism of 1.4% CNFs/bio-epoxy composites is completely adhesive in nature.

By investigating the worn surfaces, it is obvious that the surfaces of the composites are smoother than that of the neat bio-epoxy. The smooth surface is indicative of the lower wear rates being prevalent for the composites. The 3D images of the worn surfaces (Figure 38) confirm that the surface of composites are less coarse with the roughness parameter, the maximum heights of the profile ( $R_t$ ), being 37.3, 22.9, and 21.6  $\mu\text{m}$  for the neat bio-epoxy, 0.9% CNFs/bio-epoxy, and 1.4% CNFs/bio-epoxy, respectively. Generally, once the nano-cellulose fibers were incorporated, the worn surfaces appear much smoother even at severe wear conditions (at the highest normal load and sliding speed), in comparison with the neat bio-epoxy without nanofibers.

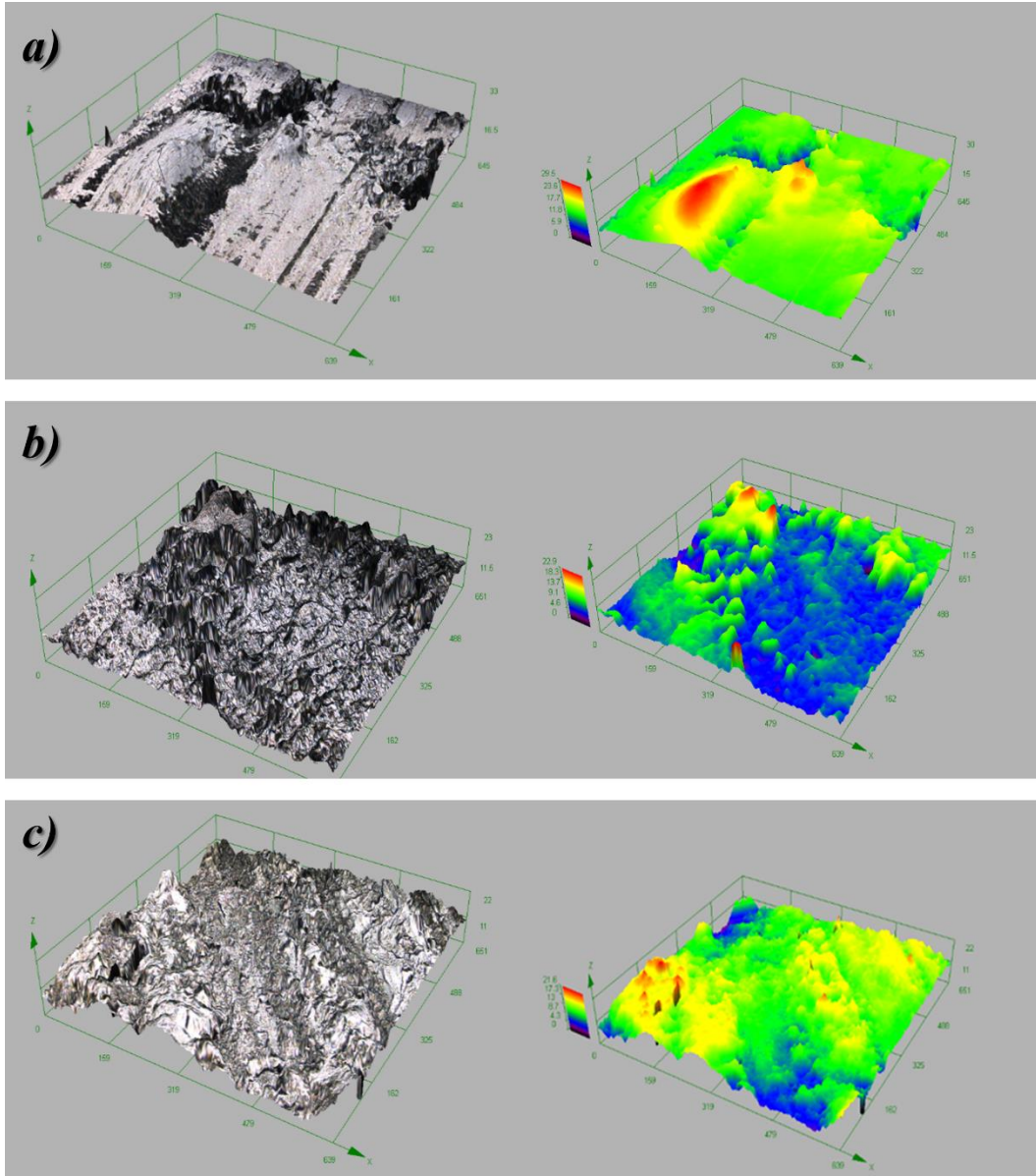
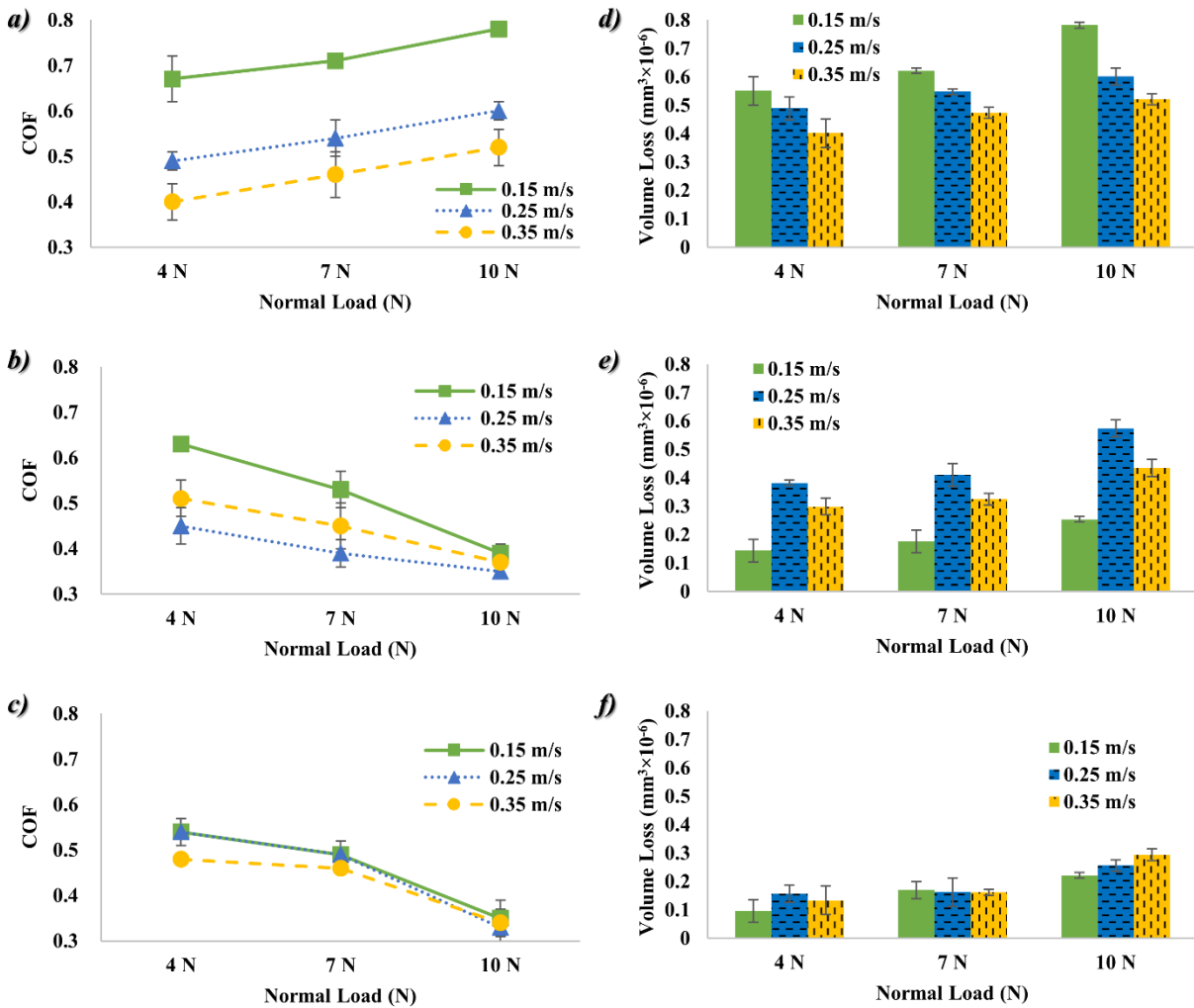


Figure 38. 3D surface topography of a) neat epoxy, b) bio-epoxy reinforced by 0.9 vol.% nano-cellulose, and c) bio-epoxy reinforced by 1.4 vol.% nano-cellulose at 7N normal load and 0.15 m/s

#### 5.4.3.2. Effect of normal load

The effect of normal load on COF of neat bio-epoxy and nano-cellulose/bio-epoxy composites is shown in Figure 39(a), (b) and (c). It can be seen that the COF increases with

increasing normal load for neat bio-epoxy while the COF decreases with increasing normal load for nano-cellulose/bio-epoxy nanocomposites. The effect of normal load on wear volume loss of neat bio-epoxy and nano-cellulose/bio-epoxy is shown in Figure 39(d), (e) and (f). Increasing the normal load tends to increase the wear volume loss due to high deformation and more detritions on the surface of composites. As stated earlier, more CNF reinforcements are exposed to the contact surface at higher normal load. Hence, a transfer layer forms at the contact surface which reduces direct surface contact. Consequently, the coefficient of friction is decreased.



*Figure 39. Effect of normal load on COF of a) neat bio-epoxy, b) 0.9 vol.% nano-cellulose/bio-epoxy, and c) 1.4 vol.% nano-cellulose/bio-epoxy at different sliding speeds and effect of normal load on wear volume of d) neat bio-epoxy, e) 0.9 vol.% nano-cellulose/bio-epoxy, and f) 1.4 vol.% nano-cellulose/bio-epoxy at different sliding speeds*

Figure 40(a) and (b) exhibits the worn surface of bio-epoxy nanocomposites reinforced by 1.4 vol. % nano-cellulose at a constant sliding speed 0.15 m/s for low and high normal load conditions. It is obvious that there are cracks on the surface of composites tested with higher load while no crack can be found on the surface of composites with low loads. Consequently, the wear rate is greater at the higher applied load due to the deterioration of materials in the presence of cracks. In addition, Figure 40(c) and (d) shows that the bonding between nano-cellulose and bio-epoxy was broken at higher normal load, therefore, CNFs were not able to carry the load and hence the load bearing ability of CNFs decreased and it tended to have higher wear rates at higher normal loads.

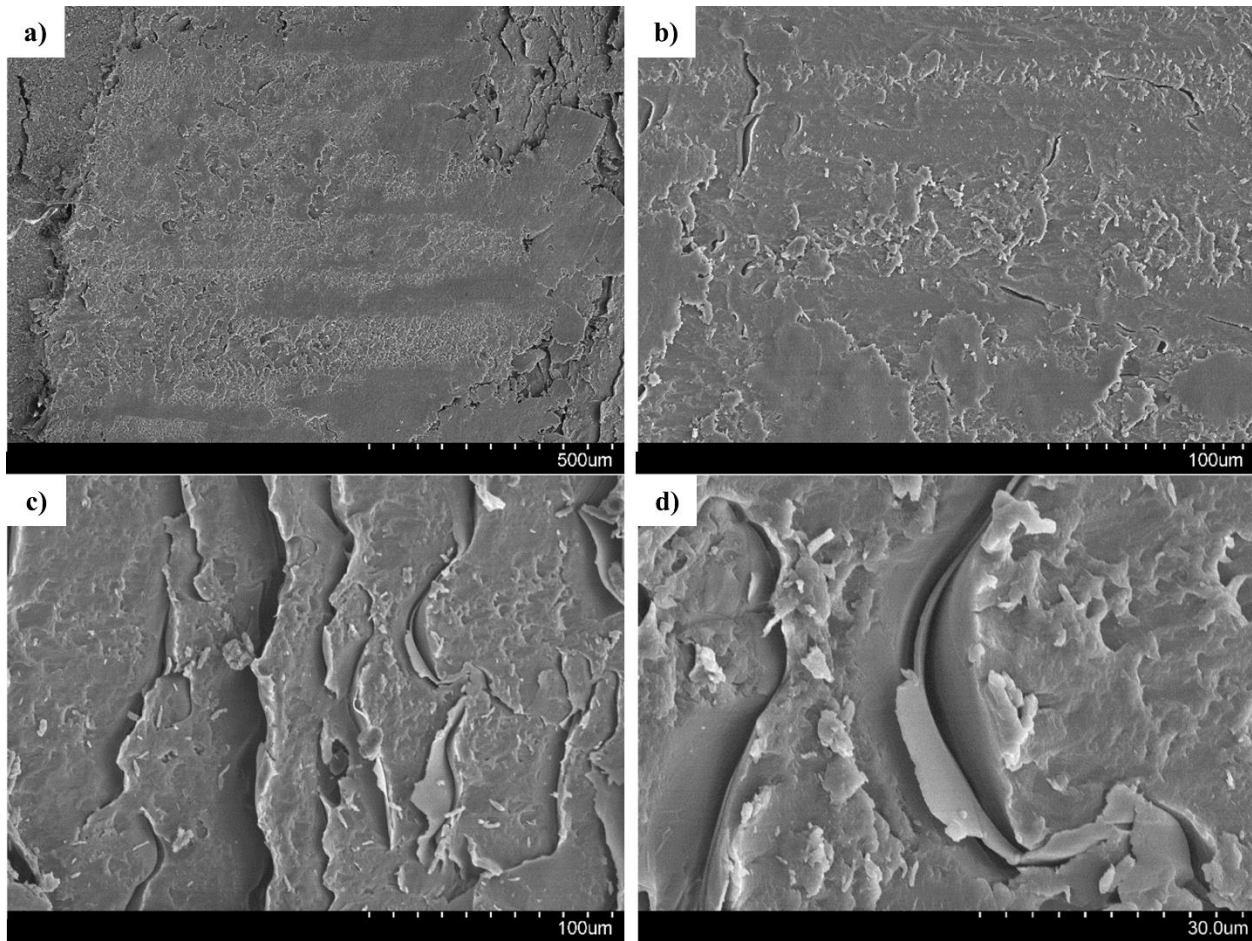


*Figure 40. Worn surface of bio-epoxy nanocomposites reinforced by 1.4 vol.% nano-cellulose at a) 4N and b) 10N applied load at 0.15 m/s and worn surface of bio-epoxy nanocomposites reinforced by 1.4 vol.% nano-cellulose at 10N applied load and 0.15 m/s sliding speed at (c) 500X and (d) 1800X magnifications.*

### **5.4.3.3. Effect of sliding speed**

Figure 41(a), (b) and (c) shows the variation of COF with sliding speed for the neat bio-epoxy and the nano-cellulose/bio-epoxy nanocomposites at different normal loads. The neat bio-epoxy shows a reduction in COF with increasing sliding speed. For the 0.9 vol.% nano-cellulose/bio-epoxy composite, the COF decreased with increasing sliding speed up to 0.25 m/s and then it further increased with the increasing sliding speed till 0.35 m/s. These variations are significantly less at the 10N normal load. Despite having an increasing COF with the increasing



speed, the COF of nanocomposite is less than that of the neat bio-epoxy. The 1.4 vol.% nano-cellulose/bio-epoxy composite exhibits different tribological behavior at low, medium, and high normal loads. The COF increases and then slightly decreases for the 4N normal load. For the 7N normal load, the COF does not change much when the speed changes from 0.15 to 0.25 m/s. However, it slightly decreases for 0.35 m/s. On the other hand, at the higher normal load of 10 N, the COF decreases and then increases with the increasing sliding speed. The variation of wear volume with the sliding speed for the neat bio-epoxy and the nano-cellulose/bio-epoxy nanocomposites at different normal loads is depicted in Figure 41(d), (e) and (f). When the sliding speed increases, the wear volume of the neat bio-epoxy decreases. For the 0.9 vol.% nano-cellulose/bio-epoxy, the wear volume increases with the increasing sliding speed up to 0.25 m/s and then it decreases at the sliding speed of 0.35 m/s where the wear of the nanocomposite is less than that of the neat bio-epoxy. The wear volume for the 1.4 vol.% nano-cellulose/bio-epoxy increases with the increasing sliding velocity, but this variation is less significant when compared with that of the neat bio-epoxy and 0.9 vol.% nano-cellulose/bio-epoxy composites.

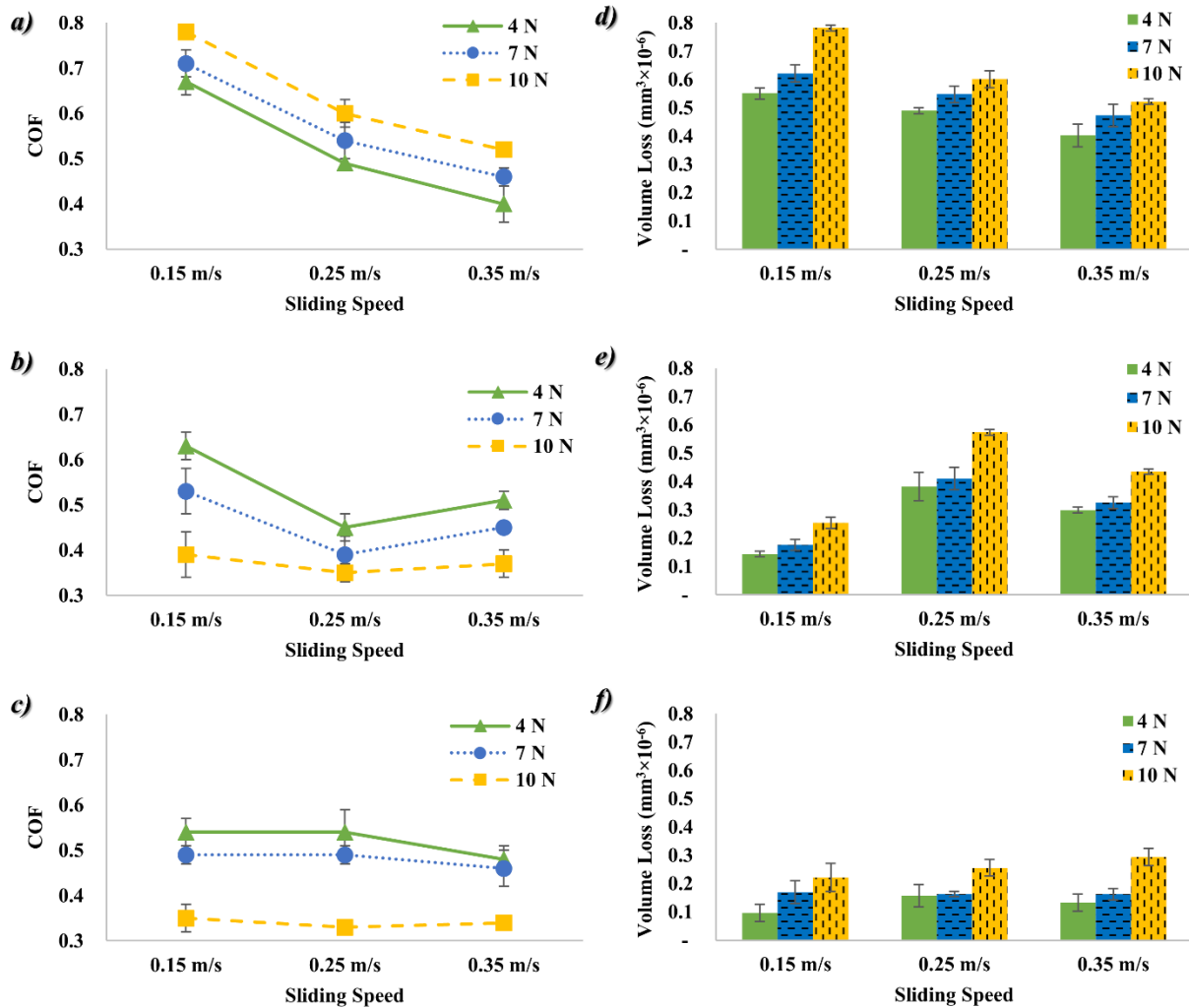


Figure 41. Effect of sliding speed on COF of nano-cellulose/ bio-epoxy nanocomposites for a) neat bio-epoxy, b) 0.9 vol.% nano-cellulose/bio-epoxy, and c) 1.4 vol.% nano-cellulose/bio-epoxy at different normal loads effect of sliding speed on wear volume of nano-cellulose/ bio-epoxy nanocomposites for d) neat bio-epoxy, e) 0.9 vol.% nano-cellulose/bio-epoxy, and f) 1.4 vol.% nano-cellulose/bio-epoxy at different normal load.

## 5.5. Summery and Conclusions

In this study, a bio-based epoxy composite reinforced with freeze dried, silylated and non-silylated CNF preforms was prepared using an improvised LCM process where the resin was imbibed inside the preform through vacuum suction. The isothermal and dynamic DSC tests were conducted to investigate the cure kinetics of bio-epoxy in the presence of CNF preforms. The

investigations revealed that the reaction between the siloxane groups and the bio-epoxy rings showed catalytic effects on the curing of bio-epoxy in the presence of CNFs which improved the mechanical properties of the silylated CNF composites compared to the non-silylated samples. In addition, the kinetic behavior of the treated and non-treated CNF composites was studied and a relation was derived for the conversion as a function of time. The mechanical testing results also correlated with the results obtained by DSC where the highest ultimate strength and elastic moduli obtained for the silylated CNF coupons. The moderate global mechanical properties of the manufactured CNF composites could be explained as a result of low mechanical properties of the used bio-based epoxy and low fiber volume fractions due to the highly porous structure of CNF. Tribological behavior of the silylated CNFs composites showed lower COFs and wear volumes than the neat bio-epoxy due to the formation of a transfer film on the mating surfaces, which led to a decrease in the 'direct contact' of the composite with the asperities of the hard metallic counterface. At higher loads, the COF is decreased for the composites due to the higher wear rates and more exposed CNF fibers on the surfaces. No consistent correlation between the sliding speed and COF/volume loss was observed.

## References

1. Whitaker, S., *The method of volume averaging*. Vol. 13. 1998: Springer.
2. Fowler, P.A., J.M. Hughes, and R.M. Elias, *Biocomposites: technology, environmental credentials and market forces*. Journal of the Science of Food and Agriculture, 2006. **86**(12): p. 1781-1789.
3. Brosius, D., *Natural fiber composites slowly take root*. Composites Technology, 2006: p. 32-37.
4. Abdul Khalil, H., M. Marliana, A. Issam, and I. Bakare, *Exploring isolated lignin material from oil palm biomass waste in green composites*. Materials & Design, 2011. **32**(5): p. 2604-2610.
5. Khalil, H.A., A. Bhat, and A.I. Yusra, *Green composites from sustainable cellulose nanofibrils: A review*. Carbohydrate Polymers, 2012. **87**(2): p. 963-979.
6. Ho, M.-p. and K.-t. Lau, *Design of an impact resistant glass fibre/epoxy composites using short silk fibres*. Materials & Design, 2012. **35**: p. 664-669.
7. Eichhorn, S., A. Dufresne, M. Aranguren, N. Marcovich, J. Capadona, S. Rowan, C. Weder, W. Thielemans, M. Roman, and S. Renneckar, *Review: current international research into cellulose nanofibres and nanocomposites*. Journal of Materials Science, 2010. **45**(1): p. 1-33.
8. Henriksson, M., L.A. Berglund, P. Isaksson, T. Lindström, and T. Nishino, *Cellulose nanopaper structures of high toughness*. Biomacromolecules, 2008. **9**(6): p. 1579-1585.
9. Lee, S.-Y., S.-J. Chun, I.-A. Kang, and J.-Y. Park, *Preparation of cellulose nanofibrils by high-pressure homogenizer and cellulose-based composite films*. Journal of Industrial and Engineering Chemistry, 2009. **15**(1): p. 50-55.

10. Teixeira, E.d.M., D. Pasquini, A.A. Curvelo, E. Corradini, M.N. Belgacem, and A. Dufresne, *Cassava bagasse cellulose nanofibrils reinforced thermoplastic cassava starch*. Carbohydrate polymers, 2009. **78**(3): p. 422-431.
11. Nakagaito, A. and H. Yano, *The effect of morphological changes from pulp fiber towards nano-scale fibrillated cellulose on the mechanical properties of high-strength plant fiber based composites*. Applied Physics A, 2004. **78**(4): p. 547-552.
12. Nakagaito, A. and H. Yano, *Novel high-strength biocomposites based on microfibrillated cellulose having nano-order-unit web-like network structure*. Applied Physics A, 2005. **80**(1): p. 155-159.
13. Henriksson, M. and L.A. Berglund, *Structure and properties of cellulose nanocomposite films containing melamine formaldehyde*. Journal of Applied Polymer Science, 2007. **106**(4): p. 2817-2824.
14. Jonoobi M, M.A.P., Abdi M, Makinejad M, Oksman K, *A comparison of modified and unmodified cellulose nanofiber reinforced polylactic acid (PLA) prepared by twin screw extrusion*. Journal of Polymers and the Environment, 2012. **20**(4): p. 991-997.
15. Sehaqui, H., Q. Zhou, and L.A. Berglund, *Nanostructured biocomposites of high toughness—a wood cellulose nanofiber network in ductile hydroxyethylcellulose matrix*. Soft Matter, 2011. **7**(16): p. 7342-7350.
16. Khalid, M., C.T. Ratnam, T.G. Chuah, S. Ali, and T.S. Choong, *Comparative study of polypropylene composites reinforced with oil palm empty fruit bunch fiber and oil palm derived cellulose*. Materials & Design, 2008. **29**(1): p. 173-178.

17. Mottershead, B. and S. Eichhorn, *Deformation micromechanics of model regenerated cellulose fibre-epoxy/polyester composites*. Composites science and technology, 2007. **67**(10): p. 2150-2159.
18. Siró, I. and D. Plackett, *Microfibrillated cellulose and new nanocomposite materials: a review*. Cellulose, 2010. **17**(3): p. 459-494.
19. Masoodi, R., R. El-Hajjar, K. Pillai, and R. Sabo, *Mechanical characterization of cellulose nanofiber and bio-based epoxy composite*. Materials & Design, 2012. **36**: p. 570-576.
20. Barari, B., Pillai, K. M., Qamhia, I. I., El-Hajjar, R., Ellingham, T. K., Turng, L-S, Sabo, R., *Mechanical Testing Of Scaled Cellulose Nano-Fiber Based Composites Made Using Micro-Rtm Process*, in *19th International Conference On Composite Materials*. 2013: Montreal, Canada.
21. Islam, M.S., K.L. Pickering, and N.J. Foreman, *Influence of alkali fiber treatment and fiber processing on the mechanical properties of hemp/epoxy composites*. Journal of Applied Polymer Science, 2011. **119**(6): p. 3696-3707.
22. Wainwright, S.A., *Mechanical design in organisms*. 1982: Princeton University Press.
23. Lu, J., P. Askeland, and L.T. Drzal, *Surface modification of microfibrillated cellulose for epoxy composite applications*. Polymer, 2008. **49**(5): p. 1285-1296.
24. Kuo, P.-Y., N. Yan, and M. Sain, *Influence of cellulose nanofibers on the curing behavior of epoxy/amine systems*. European Polymer Journal, 2013. **49**(12): p. 3778-3787.
25. Shibata, M. and K. Nakai, *Preparation and properties of biocomposites composed of bio-based epoxy resin, tannic acid, and microfibrillated cellulose*. Journal of Polymer Science Part B: Polymer Physics, 2010. **48**(4): p. 425-433.

26. Saito, T., M. Hirota, N. Tamura, S. Kimura, H. Fukuzumi, L. Heux, and A. Isogai, *Individualization of nano-sized plant cellulose fibrils by direct surface carboxylation using TEMPO catalyst under neutral conditions*. *Biomacromolecules*, 2009. **10**(7): p. 1992-1996.
27. *EntropySuperSap-100/1000*. <[http://www.entropyresins.com/sites/default/files/SuperSap-100\\_1000\\_TDS.pdf](http://www.entropyresins.com/sites/default/files/SuperSap-100_1000_TDS.pdf)>
28. *ASTM Standard D6866-11. Standard test methods for determining the bio-based content of solid, liquid, and gaseous samples using radiocarbon analysis*. . ASTM International, 2011.
29. Rasband, W.S., *ImageJ*, U. S. National Institutes of Health. Bethesda, Maryland, USA, <http://imagej.nih.gov/ij/>, 1997-2014.
30. Qamhia, I.I., R.C. Sabo, and R.F. Elhajjar, *Static and Dynamic Characterization of Cellulose Nanofibril Scaffold-Based Composites*. *BioResources*, 2013. **9**(1): p. 381-392.
31. Jonoobi, M., J. Harun, A.P. Mathew, and K. Oksman, *Mechanical properties of cellulose nanofiber (CNF) reinforced polylactic acid (PLA) prepared by twin screw extrusion*. *Composites Science and Technology*, 2010. **70**(12): p. 1742-1747.
32. Bondeson, D., P. Syre, and K.O. Niska, *All cellulose nanocomposites produced by extrusion*. *Journal of Biobased Materials and Bioenergy*, 2007. **1**(3): p. 367-371.
33. Förch, R., H. Schönherr, and A.T.A. Jenkins, *Surface design: applications in bioscience and nanotechnology*. 2009: John Wiley & Sons.
34. Abdelmouleh, M., Boufi, S, Belgacem, M Ns, Dufresne, A, *Short natural-fibre reinforced polyethylene and natural rubber composites: effect of silane coupling agents and fibres loading*. *Composites Science and Technology*, 2007. **67**(7): p. 1627-1639.

35. Abdelmouleh, M., S. Boufi, M.N. Belgacem, A. Dufresne, and A. Gandini, *Modification of cellulose fibers with functionalized silanes: effect of the fiber treatment on the mechanical performances of cellulose–thermoset composites*. Journal of applied polymer science, 2005. **98**(3): p. 974-984.
36. Xie, Y., C.A. Hill, Z. Xiao, H. Militz, and C. Mai, *Silane coupling agents used for natural fiber/polymer composites: A review*. Composites Part A: Applied Science and Manufacturing, 2010. **41**(7): p. 806-819.
37. Osswald, T.A. and G. Menges, *Materials science of polymers for engineers*. 2012: Carl Hanser Verlag GmbH Co KG.
38. Grunert, M. and W.T. Winter, *Nanocomposites of cellulose acetate butyrate reinforced with cellulose nanocrystals*. Journal of Polymers and the Environment, 2002. **10**(1-2): p. 27-30.
39. Bismarck, A., C. Burgstaller, K.Y. Lee, B. Madsen, J. Muessig, C. Santulli, and C. Scarponi, *Recent Progress in Natural Fibre Composites: Selected Papers from the 3rd International Conference on Innovative Natural Fibre Composites for Industrial Applications, Ecocomp 2011 and BEPS 2011*. Journal of Biobased Materials and Bioenergy, 2012. **6**(4): p. 343-345.
40. Koronis, G., A. Silva, and M. Fontul, *Green composites: a review of adequate materials for automotive applications*. Composites Part B: Engineering, 2013. **44**(1): p. 120-127.
41. Rwawiire, S., J. Okello, and G. Habbi, *Comparative Evaluation of Dynamic Mechanical Properties of Epoxy Composites Reinforced with Woven Fabrics from Sansevieria (Sansevieria trifasciata) Fibres and Banana (Musa sapientum) Fibres Primerjalna ocena dinamičnih mehanskih lastnosti epoksi*. Tekstilec, 2014. **57**(4).



42. Bergenstråhle, M., L.A. Berglund, and K. Mazeau, *Thermal response in crystalline I $\beta$  cellulose: a molecular dynamics study*. The Journal of Physical Chemistry B, 2007. **111**(30): p. 9138-9145.
43. Eichhorn, S. and G. Davies, *Modelling the crystalline deformation of native and regenerated cellulose*. Cellulose, 2006. **13**(3): p. 291-307.
44. Matsuo, M., C. Sawatari, Y. Iwai, and F. Ozaki, *Effect of orientation distribution and crystallinity on the measurement by X-ray diffraction of the crystal lattice moduli of cellulose I and II*. Macromolecules, 1990. **23**(13): p. 3266-3275.
45. Nishino, T., K. Takano, and K. Nakamae, *Elastic modulus of the crystalline regions of cellulose polymorphs*. Journal of Polymer Science Part B: Polymer Physics, 1995. **33**(11): p. 1647-1651.
46. Hsieh, Y.-C., H. Yano, M. Nogi, and S. Eichhorn, *An estimation of the Young's modulus of bacterial cellulose filaments*. Cellulose, 2008. **15**(4): p. 507-513.
47. Shih, Y.-F., *Mechanical and thermal properties of waste water bamboo husk fiber reinforced epoxy composites*. Materials Science and Engineering: A, 2007. **445**: p. 289-295.
48. Maleque, M., F. Belal, and S. Sapuan, *Mechanical properties study of pseudo-stem banana fiber reinforced epoxy composite*. The Arabian journal for science and engineering, 2007. **32**(2B): p. 359-364.
49. Li, J., Z. Song, D. Li, S. Shang, and Y. Guo, *Cotton cellulose nanofiber-reinforced high density polyethylene composites prepared with two different pretreatment methods*. Industrial Crops and Products, 2014. **59**: p. 318-328.

50. Boldizar, A., C. Klason, J. Kubat, P. Näslund, and P. Saha, *Prehydrolyzed cellulose as reinforcing filler for thermoplastics*. International Journal of Polymeric Materials, 1987. **11**(4): p. 229-262.
51. Low, I.M., J. Somers, H. Kho, I. Davies, and B. Latella, *Fabrication and properties of recycled cellulose fibre-reinforced epoxy composites*. Composite Interfaces, 2009. **16**(7-9): p. 659-669.
52. Barari, B., T. Ellingham, I.I. Qamhia, K.M. Pillai, R. El-Hajjar, L.-S. Turng, and R. Sabo, *Mechanical characterization of scalable cellulose nano-fiber based composites made using liquid composite molding process*. Composites Part B: Engineering, 2015.
53. Wang, B., S. Panigrahi, L. Tabil, and W. Crerar, *Pre-treatment of flax fibers for use in rotationally molded biocomposites*. Journal of reinforced plastics and composites, 2007. **26**(5): p. 447-463.
54. Dhakal, H., Z. Zhang, and M. Richardson, *Effect of water absorption on the mechanical properties of hemp fibre reinforced unsaturated polyester composites*. Composites Science and Technology, 2007. **67**(7): p. 1674-1683.
55. Leman, Z., S. Sapuan, A. Saifol, M.A. Maleque, and M. Ahmad, *Moisture absorption behavior of sugar palm fiber reinforced epoxy composites*. Materials & Design, 2008. **29**(8): p. 1666-1670.
56. Barari, B., T. Ellingham, I. Qamhia, K. Pillai, R. El-Hajjar, L.-S. Turng, and R. Sabo, *Mechanical characterization of scalable cellulose nano-fiber based composites made using liquid composite molding process*. Composites Part B: Engineering, 2015.

57. Barari, B. and K.M. Pillai, *Search for a 'Green' Composite Material: An Attempt to Fabricate Cellulose Nano-Fiber Composites using Liquid Composite Molding*. Journal of the Indian Institute of Science, 2015. **95**(3): p. 313–320.
58. Slattery, J.C., *Flow of viscoelastic fluids through porous media*. AIChE Journal, 1967. **13**(6): p. 1066-1071.
59. Whitaker, S., *Diffusion and dispersion in porous media*. AIChE Journal, 1967. **13**(3): p. 420-427.
60. Whitaker, S., *Advances in theory of fluid motion in porous media*. Industrial & engineering chemistry, 1969. **61**(12): p. 14-28.
61. Anderson, T.B., Jackson, R., *A fluid mechanical description of fluidized beds*. Ind Eng Chem Fundam, 1967. **6**: p. 527-39.
62. He YQ, S.J., *On the spatial-temporal averaging method for modeling transport in porous media*. Transp Porous Media 1996. **22**(1): p. 1-51.
63. J., M., *On the existence of the derivative of the volume average*. Transp Porous Media 1987. **2**: p. 615-21.
64. WG., G., *General conservation equations for multi-phase systems: Constitutive theory including phase change*. Adv Water Resour 1983. **6**: p. 130-40.
65. Gray WG, L.P., *On the theorems for local volume averaging of multiphase systems*. Int J Multiphase Flow 1977. **3**: p. 333-40.
66. Hassanizadeh M, G.W., *General Conservation Equations for Multi-Phase Systems: 1. Averaging procedure*. Adv Water Resour 1979. **2**: p. 131-44.
67. Bennethum L, C.J., *Multiscale, hybrid mixture theory for swelling systems*. Int J Eng Sci 1996. **34**(2): p. 125-45.

68. Gray WG, M.C., *Thermodynamically constrained averaging theory approach for modeling flow and transport phenomena in porous medium systems: 1. Motivation and overview*. Adv Water Resour 2005. **28**(2): p. 161-80.
69. Howes FA, W.S., *The spatial averaging theorem revisited*. Chem Eng Sci 1985. **40**: p. 1387-92.
70. S., W., *A simple geometrical derivation of the spatial averaging theorem*. Chem Eng Educ, 1985. **19**(1): p. 50-52.
71. Lux, J., A. Ahmadi, C. Gobbe, and C. Delisée, *Macroscopic thermal properties of real fibrous materials: Volume averaging method and 3D image analysis*. International Journal of Heat and Mass Transfer, 2006. **49**(11): p. 1958-1973.
72. Hsu, C.T., *A closure model for transient heat conduction in porous media*. Journal of heat transfer, 1999. **121**(3): p. 733-739.
73. Nakayama, A., Kuwahara, F., Sugiyama, M., Xu, G., *A Two-Energy Equation Model for Conduction and Convection in Porous Media*. Int J Heat Mass Transfer 2001. **44**(22): p. 4375-9.
74. Pillai, K.M., *Single-Phase Flows In Swelling, Liquid-Absorbing Porous Media: A Derivation Of Flow Governing Equations Using The Volume Averaging Method With A Nondeterministic, Heuristic Approach To Assessing The Effect Of Solid-Phase Changes*. Journal of Porous Media, 2014. **17**(10).
75. Guibert, R., M. Nazarova, P. Horgue, G. Hamon, P. Creux, and G. Debenest, *Computational Permeability Determination from Pore-Scale Imaging: Sample Size, Mesh and Method Sensitivities*. Transport in Porous Media, 2015. **107**(3): p. 641-656.

76. Bear, J.a.B., Y., *Introduction to Modeling of Transport Phenomena in Porous Media*. 1990, Dordrecht: Kluwer Academic.
77. Quintard, M., Bletzacker, L., Chenu, D., and Whitaker, S., *Nonlinear, Multicomponent, Mass Transport in Porous Media*. Chem. Eng. Sci., 2006. **61**: p. 2643-69.
78. Kim J. H., O., J. A. and Whitaker, S., *Diffusion in anisotropic porous media*. Transport porous media, 1987. **2**: p. 327-56.
79. Yohan Davit, M.Q., Gérald Debenest, *Equivalence between volume averaging and moments matching techniques for mass transport models in porous media*. International Journal of Heat and Mass Transfer, 2010. **53**: p. 4985-4993.
80. Golfier, F., Wood, B. D., Orgogozo, L., Quintard, M., Buès, M., *Biofilms in porous media: development of macroscopic transport equations via volume averaging with closure for local mass equilibrium conditions*. Advances in water resources, 2009. **32**(3): p. 463-485.
81. Mostaghimi, P., M.J. Blunt, and B. Bijeljic, *Computations of absolute permeability on micro-CT images*. Mathematical Geosciences, 2013. **45**(1): p. 103-125.
82. Blunt, M.J., B. Bijeljic, H. Dong, O. Gharbi, S. Iglauer, P. Mostaghimi, A. Paluszny, and C. Pentland, *Pore-scale imaging and modelling*. Advances in Water Resources, 2013. **51**: p. 197-216.
83. Piller, M., G. Schena, M. Nolic, S. Favretto, F. Radaelli, and E. Rossi, *Analysis of hydraulic permeability in porous media: from high resolution X-ray tomography to direct numerical simulation*. Transport in porous media, 2009. **80**(1): p. 57-78.
84. Vignoles, G.L., O. Coindreau, A. Ahmadi, and D. Bernard, *Assessment of geometrical and transport properties of a fibrous C/C composite preform as digitized by x-ray computerized*

- microtomography: Part II. Heat and gas transport properties*. Journal of materials research, 2007. **22**(06): p. 1537-1550.
85. Belhouideg, S. and M. Lagache, *Prediction of the effective permeability coefficient in random porous media using the finite element method*. Journal of Porous Media, 2014. **17**(9).
86. Guibert, R., P. Horgue, G. Debenest, and M. Quintard, *A Comparison of Various Methods for the Numerical Evaluation of Porous Media Permeability Tensors from Pore-Scale Geometry*. Mathematical Geosciences, 2015: p. 1-19.
87. Zhang, S., R. Klimentidis, and P. Barthelemy. *Porosity and permeability analysis on nanoscale FIB-SEM 3D imaging of shale rock*. in *SCA Symposium*. 2011.
88. Avizo Software, V.W.O.U.M.A.a. and <http://www.vsg3d.com/avizo/overview>.
89. Bear, J., *Dynamics of fluids in porous media*. Eisevier, New York, 764p, 1972.
90. Sabo, R.C., R.F. Elhajjar, C.M. Clemons, and K.M. Pillai, *Characterization And Processing Of Nanocellulose Thermosetting Composites*, in *Handbook of Polymer Nanocomposites. Processing, Performance and Application*. 2015, Springer. p. 265-295.
91. Ankerfors, M., Lindström, T. *NanoCellulose Developments in Scandinavia*. in *Paper and Coating Chemistry Symposium (PCCS)*. 2009.
92. Saito, T., Hirota, M., Tamura, N., Kimura, S., Fukuzumi, H., Heux, L., Isogai, A., *Individualization of nano-sized plant cellulose fibrils by direct surface carboxylation using TEMPO catalyst under neutral conditions*. Biomacromolecules, 2009. **10**(7): p. 1992-1996.

93. Lasseux, D., Arani, A.A., Abbasian Ahmadi, A., *On the stationary macroscopic inertial effects for one phase flow in ordered and disordered porous media*. Physics of Fluids (1994-present), 2011. **23**(7): p. 073103.
94. Quintard, M., *Diffusion in isotropic and anisotropic porous systems: Three-dimensional calculations*. Transport in Porous Media, 1993. **11**(2): p. 187-199.
95. Bernard, D., Ø. Nielsen, L. Salvo, and P. Cloetens, *Permeability assessment by 3D interdendritic flow simulations on microtomography mappings of Al–Cu alloys*. Materials Science and Engineering: A, 2005. **392**(1): p. 112-120.
96. Gebart, B., *Permeability of unidirectional reinforcements for RTM*. Journal of composite materials, 1992. **26**(8): p. 1100-1133.
97. Brusckhe, M. and S. Advani, *Flow of generalized Newtonian fluids across a periodic array of cylinders*. Journal of Rheology (1978-present), 1993. **37**(3): p. 479-498.
98. Dullien, F.A., *Porous media: fluid transport and pore structure*. 2012: Academic press.
99. Chatterjee, P.K. and B.S. Gupta, *Absorbent technology*. Vol. 13. 2002: Elsevier.
100. Zhu, H., A. Dhall, S. Mukherjee, and A.K. Datta, *A model for flow and deformation in unsaturated swelling porous media*. Transport in porous media, 2010. **84**(2): p. 335-369.
101. Weinstein, T. and L.S. Bennethum, *On the derivation of the transport equation for swelling porous materials with finite deformation*. International journal of engineering science, 2006. **44**(18): p. 1408-1422.
102. Innerlohinger, J., H.K. Weber, and G. Kraft. *Aerocellulose: Aerogels and Aerogel-like Materials made from Cellulose*. in *Macromolecular Symposia*. 2006. Wiley Online Library.

103. Tan, C., B. Fung, J. Newman, and C. Vu, *Organic aerogels with very high impact strength*. *Advanced materials*, 2001. **13**(9): p. 644-646.
104. Hüsing, N. and U. Schubert, *Aerogels—airy materials: chemistry, structure, and properties*. *Angewandte Chemie International Edition*, 1998. **37**(1-2): p. 22-45.
105. Tingaut, P., T. Zimmermann, and G. Sèbe, *Cellulose nanocrystals and microfibrillated cellulose as building blocks for the design of hierarchical functional materials*. *Journal of Materials Chemistry*, 2012. **22**(38): p. 20105-20111.
106. Li, W., K. Lu, and J. Walz, *Freeze casting of porous materials: review of critical factors in microstructure evolution*. *International Materials Reviews*, 2012. **57**(1): p. 37-60.
107. Masoodi, R., K.M. Pillai, N. Grahl, and H. Tan, *Numerical simulation of LCM mold-filling during the manufacture of natural fiber composites*. *Journal of Reinforced Plastics and Composites*, 2012. **31**(6): p. 363-378.
108. Masoodi, R. and K.M. Pillai, *Modeling the processing of natural fiber composites made using liquid composites molding*. *Handbook of Bioplastics and Biocomposites Engineering Applications*, ed. by S. Pilla, Scrivener-Wiley, 2011.
109. Masoodi, R., H. Tan, and K.M. Pillai, *Numerical simulation of liquid absorption in paper-like swelling porous media*. *AIChE Journal*, 2012. **58**(8): p. 2536-2544.
110. Masoodi, R. and K.M. Pillai, *Darcy's law-based model for wicking in paper-like swelling porous media*. *AIChE journal*, 2010. **56**(9): p. 2257-2267.
111. Bear, J., *Dynamics of fluids in porous media*. 2013: Courier Corporation.
112. Omrani, E., P.L. Menezes, and P.K. Rohatgi, *State of the art on tribological behavior of polymer matrix composites reinforced with natural fibers in the green materials world*. *Engineering Science and Technology, an International Journal*, 2015.



113. Cheung, H.-y., M.-p. Ho, K.-t. Lau, F. Cardona, and D. Hui, *Natural fibre-reinforced composites for bioengineering and environmental engineering applications*. Composites Part B: Engineering, 2009. **40**(7): p. 655-663.
114. Wambua, P., J. Ivens, and I. Verpoest, *Natural fibres: can they replace glass in fibre reinforced plastics?* composites science and technology, 2003. **63**(9): p. 1259-1264.
115. Alawar, A., A.M. Hamed, and K. Al-Kaabi, *Characterization of treated date palm tree fiber as composite reinforcement*. Composites Part B: Engineering, 2009. **40**(7): p. 601-606.
116. Chand, N. and U. Dwivedi, *High stress abrasive wear study on bamboo*. Journal of materials processing technology, 2007. **183**(2): p. 155-159.
117. Chin, C. and B. Yousif, *Potential of kenaf fibres as reinforcement for tribological applications*. Wear, 2009. **267**(9): p. 1550-1557.
118. Hepworth, D., J. Vincent, G. Jeronimidis, and D. Bruce, *The penetration of epoxy resin into plant fibre cell walls increases the stiffness of plant fibre composites*. Composites Part A: Applied Science and Manufacturing, 2000. **31**(6): p. 599-601.
119. Qamhia, I.I., S.S. Shams, and R.F. El-Hajjar, *Quasi-Isotropic Triaxially Braided Cellulose-Reinforced Composites*. Mechanics of Advanced Materials and Structures, 2015. **22**(12): p. 988-995.
120. Saha, P., S. Manna, S.R. Chowdhury, R. Sen, D. Roy, and B. Adhikari, *Enhancement of tensile strength of lignocellulosic jute fibers by alkali-steam treatment*. Bioresource technology, 2010. **101**(9): p. 3182-3187.

121. Virk, A.S., W. Hall, and J. Summerscales, *Failure strain as the key design criterion for fracture of natural fibre composites*. Composites Science and Technology, 2010. **70**(6): p. 995-999.
122. Venkateshwaran, N., A. Elayaperumal, and G. Sathiya, *Prediction of tensile properties of hybrid-natural fiber composites*. Composites Part B: Engineering, 2012. **43**(2): p. 793-796.
123. Kim, S.-J., J.-B. Moon, G.-H. Kim, and C.-S. Ha, *Mechanical properties of polypropylene/natural fiber composites: comparison of wood fiber and cotton fiber*. Polymer testing, 2008. **27**(7): p. 801-806.
124. Plackett, D., T.L. Andersen, W.B. Pedersen, and L. Nielsen, *Biodegradable composites based on L-poly lactide and jute fibres*. Composites Science and Technology, 2003. **63**(9): p. 1287-1296.
125. Haque, M.M., M. Hasan, M.S. Islam, and M.E. Ali, *Physico-mechanical properties of chemically treated palm and coir fiber reinforced polypropylene composites*. Bioresource Technology, 2009. **100**(20): p. 4903-4906.
126. Ku, H., H. Wang, N. Pattarachaiyakoop, and M. Trada, *A review on the tensile properties of natural fiber reinforced polymer composites*. Composites Part B: Engineering, 2011. **42**(4): p. 856-873.
127. Shibata, S., Y. Cao, and I. Fukumoto, *Press forming of short natural fiber-reinforced biodegradable resin: Effects of fiber volume and length on flexural properties*. Polymer testing, 2005. **24**(8): p. 1005-1011.
128. Shalwan, A. and B. Yousif, *In State of Art: Mechanical and tribological behaviour of polymeric composites based on natural fibres*. Materials & Design, 2013. **48**: p. 14-24.

129. Yousif, B., S.T. Lau, and S. McWilliam, *Polyester composite based on betelnut fibre for tribological applications*. Tribology international, 2010. **43**(1): p. 503-511.
130. Yousif, B. and N. El-Tayeb, *Adhesive wear performance of T-OPRP and UT-OPRP composites*. Tribology letters, 2008. **32**(3): p. 199-208.
131. Nirmal, U., J. Hashim, and K. Low, *Adhesive wear and frictional performance of bamboo fibres reinforced epoxy composite*. Tribology International, 2012. **47**: p. 122-133.
132. Chand, N. and U. Dwivedi, *Effect of coupling agent on abrasive wear behaviour of chopped jute fibre-reinforced polypropylene composites*. Wear, 2006. **261**(10): p. 1057-1063.
133. Barari, B. and K. Pillai, *Calibration of one-dimensional flow setup used for estimating fabric permeability using three different reference media*. Polymer Composites, 2014.
134. Menezes, P.L., M. Nosonovsky, S.V. Kailas, and M.R. Lovell, *Friction and wear*, in *Tribology for Scientists and Engineers*. 2013, Springer. p. 43-91.
135. Alamri, H. and I.M. Low, *Microstructural, mechanical, and thermal characteristics of recycled cellulose fiber-halloysite-epoxy hybrid nanocomposites*. Polymer Composites, 2012. **33**(4): p. 589-600.
136. Leyland, A. and A. Matthews, *On the significance of the H/E ratio in wear control: a nanocomposite coating approach to optimised tribological behaviour*. Wear, 2000. **246**(1): p. 1-11.
137. Alamri, H. and I.M. Low, *Mechanical properties and water absorption behaviour of recycled cellulose fibre reinforced epoxy composites*. Polymer testing, 2012. **31**(5): p. 620-628.

138. Myshkin, N., M. Petrokovets, and A. Kovalev, *Tribology of polymers: adhesion, friction, wear, and mass-transfer*. Tribology International, 2006. **38**(11): p. 910-921.
139. Bahadur, S., *The development of transfer layers and their role in polymer tribology*. Wear, 2000. **245**(1): p. 92-99.
140. Chang, L. and K. Friedrich, *Enhancement effect of nanoparticles on the sliding wear of short fiber-reinforced polymer composites: a critical discussion of wear mechanisms*. Tribology international, 2010. **43**(12): p. 2355-2364.
141. Xian, G., R. Walter, and F. Hauptert, *Friction and wear of epoxy/TiO<sub>2</sub> nanocomposites: Influence of additional short carbon fibers, Aramid and PTFE particles*. Composites Science and Technology, 2006. **66**(16): p. 3199-3209.
142. Menezes, P.L. and S.V. Kailas, *Influence of surface texture and roughness parameters on friction and transfer layer formation during sliding of aluminium pin on steel plate*. Wear, 2009. **267**(9): p. 1534-1549.
143. Menezes, P.L. and S.V. Kailas, *On the effect of surface texture on friction and transfer layer formation—a study using Al and steel pair*. Wear, 2008. **265**(11): p. 1655-1669.

# Curriculum Vitae

## BAMDAD BARARI

### CURRENT POSITION

---

- PhD at University of Wisconsin-Milwaukee, Department of mechanical Engineering, Laboratory for Flow and Transport Studies in Porous Media (Sep 2012-May 2016).
- I am principal investigator on several research topics funded from industry and academia on various fields of Numerical and experimental studies on flow and transport in different media, Microfluidic, Flow modeling and heat transfer in micro heat-pipe and micro channel, cooling electronic device using Micro heat-pipes, Heat Transfer, Numerical and experimental Flow modeling and simulation.

### SUMMARY OF QUALIFICATIONS

---

- ❖ PhD, MSc and BSc in Mechanical Engineering with multidisciplinary engineering experience in research and developing, design, modeling and experimental testing.
- ❖ Computational Fluid Dynamics (CFD), LES, RANS technics for flow modeling and heat transfer simulation in various industrial cases including electrical circuits and electronic components, Compressible and transitional flow and etc.
- ❖ Proficient in design and modeling software: COMSOL, ANSYS, Pro-E and LabVIEW; experimental process: LCM, RTM, Injection molding, sensor/transducer implementation, data acquisition systems, measurement setup for physical properties.
- ❖ Proficient in characterization and testing: SEM, DSC, DMA, Tensile, tensiometer, permeameter and good knowledge in XRD, RAMAN, TGA and optical microscope.
- ❖ Demonstrated excellent knowledge of flow and transport in porous media, flow modeling in single and multi-phase flow, heat transfer, micro/nano simulations, fluid mechanics, material and structure, cause of failure, stress and fatigue, mechanical properties and fracture investigation.
- ❖ Proven ability in numerical modeling with software and design experimental validation setup.
- ❖ Excellent understanding of product design, development cycle, fabrication processes and manufacturing methods, and developing procedures and tools for testing and validation.
- ❖ Strong ability to work with machining tools, measurement and electronic test tools.
- ❖ Proven ability to work and communicate well within cross-functional teams with limited supervision. A talent for creative and simple solutions to challenging engineering

problems. Strong analytical and problem solving ability. Ability to learn quickly in new areas outside of specialty areas.

## EDUCATION

---

- ❖ **PhD candidate in Mechanical Engineering (since 2012)**  
**University of Wisconsin-Milwaukee**  
Advisor: Prof. Krishna M. Pillai  
**Thesis title:** Experimental and Numerical Characterization of Bio-based, “Green”, Cellulose Nano-Fiber Composite.
  
- ❖ **MSc in Mechanical Engineering (Heat Transfer and Fluid Mechanics, 2010)**  
**Shiraz University, Shiraz, IRAN.**  
**Thesis title:** Numerical Analysis of Heat Transfer and Fluid Flow in Micro Heat Pipe.
  
- ❖ **BSc in Mechanical Engineering (Fluid Mechanics, 2007)**  
**Amirkabir University of Technology (Tehran Polytechnic), Tehran, IRAN.**  
Thesis Title: "Numerical Analysis of Two- Phase Turbulent Flow in Horizontal Channel"

## PROFESSIONAL EXPERIENCE

---

- ❖ **RESEARCH EXPERIENCE**
  - Graduate research assistant, Laboratory for Flow and Transport Studies in Porous Media, Department of Mechanical Engineering, University of Wisconsin-Milwaukee (Sep 2012-present).
  - Graduate research assistant for inter-disciplinary research project, Department of Material Engineering, University of Wisconsin-Milwaukee (Sep 2014-present).
  - Graduate research assistant, Department of Mechanical Engineering, University of Shiraz (Sep 2008- Aug 2010).
  
- ❖ **TEACHING EXPERIENCE**
  - **Instructor**  
Intermediate fluid mechanics, Basic heat transfer, Thermodynamics, Engineering fundamental I & II at Department of Mechanical Engineering, University of Wisconsin-Milwaukee
  - **Teaching Assistant**  
Basic heat transfer, Basic fluid mechanics at Department of Mechanical Engineering, University of Wisconsin-Milwaukee
  - **Other Teaching Experiences**

Dynamic, Machine Dynamics, Internal Combustion Engine, Engineering Drawing & Pro-E, Machine design

❖ **CHARACTERIZATION AND TESTING EXPERIENCE**

SEM, DSC, DMA, DIS, XRD, TGA, EDX, RAMAN, Optical Microscope, Tensiometer, 1D Permeameter, Resin Transfer Molding (RTM), Liquid Composite Molding (LCM), Injection Molding.

**HONORS AND AWARDS**

---

- ❖ Distinguished Dissertation Fellowship for 16500 USD, University of Wisconsin, March 2016.
- ❖ CEAS Deans Scholarship Award, University of Wisconsin-Milwaukee, 2014-2015.
- ❖ Chancellor`s graduate student award, University of Wisconsin-Milwaukee, 2013-2014.
- ❖ Chancellor`s graduate student award, University of Wisconsin-Milwaukee, 2012-2013.
- ❖ Nominated for Iranian Society of Mechanical Engineers` best BSc thesis award.
- ❖ Ranked top 4% out of more than 10,000 Mechanical Engineering Students in National Graduate Studies Entrance Examination (600 out of 15000).
- ❖ Ranked top 0.1% out of more than 300,000 Students in National Under-Graduate Studies Entrance Examination (321 out of 300,000).

**JOURNAL PAPERS**

---

- ❖ **Bamdad Barari** and Krishna M. Pillai, "*Measuring Absorption Characteristics of Cellulose Nano-Fibers for LCM Mold-Filling Simulations*", **Composite Science and Technology**, **2016**, (Under review).
- ❖ **Bamdad Barari**, Emad Omrani, Afsaneh D. Moghadam, Pradeep L. Menezes, Pradeep K. Rohatgi, Krishna M. Pillai, "*Mechanical, Microstructural and Tribological Characterization of Cellulose Nano Fibers/Bio-epoxy Composites: An Attempt to Fabricate and Scale 'Green' Composite*" **Carbohydrate Polymers**, **2015**, (Accepted for publication).
- ❖ **Bamdad Barari**, Saman Beyhaghi and Krishna M. Pillai, "*Fast 2D Micrograph-based Method of Permeability Estimation through Micro-Macro Coupling in Porous Media*", **Journal of Porous Media**, **2015**, (Accepted for publication).
- ❖ **Bamdad Barari**, Thomas K. Ellingham, Issam I. Qamhia, Krishna M. Pillai, Rani El-Hajjar, Lih-Sheng Turng, Ron Sabo, "*Mechanical characterization of Scalable Cellulose Nano-Fiber based Composites made using Liquid Composite Molding Process*", **Composites part B: Engineering**, **2015**.

<http://www.sciencedirect.com/science/article/pii/S1359836815004709>

- ❖ **Bamdad Barari** and Krishna M. Pillai, “Search for a ‘Green’ Composite Material: An Attempt to Fabricate Cellulose Nano-Fiber Composites using Liquid Composite Molding”, **Journal of the Indian Institute of Science**, **2015**, (accepted for publication).  
<http://journal.iisc.ernet.in/index.php/iisc/article/view/4575>
- ❖ Emad Omrani, **Bamdad Barari**, Afsaneh D. Moghadam, Pradeep Rohatgi, Krishna M. Pillai, “Mechanical and Tribological Properties of Bio-based Epoxy Composites reinforced by 2D Woven Carbon Fiber Made Using Resin Transfer Molding Process”, **Tribology International**, Volume 92, Pages 222–232, **2015**.  
<http://www.sciencedirect.com/science/article/pii/S0301679X15002455>
- ❖ **Bamdad Barari** and Krishna M. Pillai, “Calibration of one-dimensional flow setup used for estimating fabric permeability using three different reference media”, **Polymer Composites**, DOI: 10.1002/pc.23251, **2014**.  
<http://onlinelibrary.wiley.com/doi/10.1002/pc.23251/full>
- ❖ N Vernet, E Ruiz, S Advani, JB Alms, M Aubert, M Barbarski, **B Barari**, ..., “Experimental determination of the permeability of engineering textiles: Benchmark II”, **Composites part A: Applied Science and Manufacturing**, Volume 61, Pages 172–184, **2014**.  
<http://www.sciencedirect.com/science/article/pii/S1359835X14000505>
- ❖ **Bamdad Barari**, Abbasian Ashkan Shirazi, Mohsen Keshavarzi, Iman Rostamsowlat, “Numerical analysis and field study of time dependent exergy-energy of a gas-steam combined cycle”, **Journal of the Serbian Chemical Society**, Volume 77, Issue 7, Pages: 945-957, **2012**.  
<http://www.doiserbia.nb.rs/Article.aspx?id=0352-51391200014B#.Vc5dLldWSq>
- ❖ Alireza Rahbari, Ahmad Afsari, **Bamdad Barari**, Iman Rostamsowlat, “Theoretical Investigation over the Effects of EGR, Fuel Reforming and Compression Ratio on the HCCI Engine Operation Fuelled with Ethanol”, **Global Journal of Researches in Engineering**, Volume 12, Issue 2, **2012**.  
<http://www.engineeringresearch.org/index.php/GJRE/article/view/433>

## CONFERENCE PAPERS

---

- ❖ **Bamdad Barari** and Krishna M. Pillai, “Estimation of Permeability Using Closure Formulation in Particulate and fibrous Porous Media with Experimental Verification”, 6th International Conference on Porous Media & Annual Meeting of the International Society for Porous Media May 27 - 30, 2014, Milwaukee, Wisconsin USA.



- ❖ **Bamdad Barari** and Krishna M. Pillai, “*Mechanical Testing Of Scaled Cellulose Nano-Fiber Based Composites Made Using Micro-Rtm Process*”, 19th International Conference on Composite Materials, July 28 – August 2, 2013, Montreal, Canada.
- ❖ **Bamdad Barari**, Trevor Burg and Krishna M. Pillai, “*Creating Environment-Friendly Green Composites using Cellulose Nano-Fibers*”, Advancements in Fiber-Polymer Composites: Wood fiber, Natural Fiber and Nano-cellulose, May 6-7, 2013, Milwaukee, Wisconsin USA.
- ❖ Reza kamali, **Bamdad Barari** and Ashkan Abbasian Shirazi, “*Numerical Analysis of Entropy Generation in Array of Pin-Fin Heat Sinks for Some Different Geometries*”, **ASME 2010** 3rd Joint US-European Fluids Engineering Summer Meeting collocated with 8th International Conference on Nanochannels, Microchannels, and Minichannels, August 1–5, 2010, Montreal, Canada.  
<http://proceedings.asmedigitalcollection.asme.org/proceeding.aspx?articleid=1621228>
- ❖ Alireza Rahbari, **Bamdad Barari** and Ashkan Abbasian Shirazi, “*Computational Investigation of HCCI Engine Performance With Fuel Reforming Effect on Lean Ethanol*”, **ASME 2009** Internal Combustion Engine Division Spring Technical Conference, May 3–6, 2009, Milwaukee, Wisconsin USA.  
<http://proceedings.asmedigitalcollection.asme.org/proceeding.aspx?articleid=1622268>
- ❖ Hassan Rahimzadeh, **Bamdad Barari**, Mohammad Hesam Asoodeh, “*Numerical Analysis of Two-Phase Turbulent Flow in Horizontal Channel with Experimental Verification*”, Proceedings of the World Congress on Engineering, WCE 2008, July 2 - 4, 2008, London, U.K.  
[http://www.researchgate.net/publication/44262191\\_Numerical\\_Analysis\\_of\\_Two\\_Phase\\_Turbulent\\_Flow\\_in\\_Horizontal\\_Channel\\_with\\_Experimental\\_Verification](http://www.researchgate.net/publication/44262191_Numerical_Analysis_of_Two_Phase_Turbulent_Flow_in_Horizontal_Channel_with_Experimental_Verification)

## COMPUTER SKILLS

---

- ❖ **ENGINEERING RELATED SOFTWARE**
  - Proficient in COMSOL, ANSYS FLUENT, Pro-E
- ❖ **PROGRAMING SKILLS**
  - Basic knowledge in MATLAB, FORTRAN

## MEMBERSHIP

---

- ❖ International Society for Porous Media (InterPore)
- ❖ American Society of Mechanical Engineering (ASME)
- ❖ Society of Plastic Engineers (SPE)